Spatial Confinement of Atomic Excitation in a Doped Solid

Räumliche Begrenzung von atomarer Anregung in einem dotierten Festkörper
Dissertation von Markus Stabel, Januar 2024

TECHNISCHE
UNIVERSITÄT
DARMSTADT

Fachbereich Physik
Institut für Angewandte Physik
Nichtlineare Optik / Quantenoptik

Spatial Confinement of Atomic Excitation in a Doped Solid

Vom Fachbereich Physik
der Technischen Universität Darmstadt

zur Erlangung des Grades
eines Doktors der Naturwissenschaften
(Dr. rer. nat.)

genehmigte Dissertation von
M.Sc. Markus Stabel
aus Bensheim

Referent: Prof. Dr. Thomas Halfmann
Korreferent: Prof. Dr. Markus Gräfe

Tag der Einreichung: 10. Januar 2024
Tag der Prüfung: 12. Februar 2024

Darmstadt 2024

Markus Stabel: Spatial Confinement of Atomic Excitation in a Doped Solid
Darmstadt, Technische Universität Darmstadt
Jahr der Veröffentlichung der Dissertation auf TUprints: 2024
URN: urn:nbn:de:tuda-tuprints-266816

Tag der mündlichen Prüfung: 12. Februar 2024

Contents

Introduction

Quantum memories are an integral part of any large-scale quantum communication structure, e.g., as part of repeaters or processors. In simple terms, such a quantum memory temporarily stores the information encoded in the quantum state of a qubit. Hence, the most important characteristics of this memory are its fidelity, storage efficiency, storage time, and multimode capacity [1]. Optical implementations of quantum memories use photons as information carriers and often ensemble-based media, e.g., cold atomic gases, warm vapors, or emitters in solid-state systems such as rare-earth ion-doped crystals [2]. The latter solid-state systems hold significant potential for realistic applications in quantum technologies because they combine free-atom-like, spectrally narrow transitions [3] with the advantages of solids, i.e., absence of atomic motion, robust handling, scalability, and integratability [2].

There are already some impressive results on implementations of quantum memories in rare-earth ion-doped crystals, reaching, e.g., storage efficiencies up to 76 % [4], storage times up to 53 minutes [5] and fidelities of 99.9 % [6]. To increase the capacity of the memory, i.e., its ability to store more than one qubit simultaneously, most approaches so far rely on temporal [7, 8] or spectral [9] multiplexing. While storage of up to 1060 modes was demonstrated [8], these techniques are inherently limited by the bandwidth of the memory protocol and medium. An alternative approach utilizes spatial multiplexing. Our team already implemented such multiplexing by exploiting the phase matching condition of the memory protocol to store information in overlapping interference patterns in the crystal [9]. However, the available angular resolution strongly limits this approach, and it may suffer from cross-talk between information channels. A much simpler approach to spatial multiplexing relies on selective addressing of individual storage volumes in an extended medium [10]. The larger the medium and the smaller the optically addressable volume, the larger the spatial storage capacity of the memory. In this case, the diffraction limit for focused laser beams is expected to limit the storage capacity. Hence, we require methods to optically address small sections of a memory, potentially with extensions of the excitation area below the diameter of the driving laser beam, even if focused down to the diffraction limit. In the following, we will deal with novel techniques to overcome the diffraction limit in optical excitation.

We note that there are a multitude of other applications beyond the storage capacity of an optical quantum memory that benefit from spatial confinement of optical excitations below the diffraction limit. Examples from quantum technology are selective addressing of single emitters from a large ensemble as isolated qubits [11–13], the generation of narrow waveguide-like excitation structures in crystals to enhance light-matter interaction for quantum information processing [14], patterning of Bose-Einstein condensates [15, 16], or single-site addressing below the diffraction limit in a Paul ion trap or optical lattice [17–22] to enable tighter qubit spacing and, hence, stronger qubit interaction for quantum computations. Examples from applied optics are the broad fields of high-resolution microscopy

[23–28] and nano-lithography [15, 29–32]. Finally, also investigations of fundamental quantum physics, e.g., the measurement of the wave function of individual or ensembles of atoms, at resolutions below the diffraction limit, become possible [33–36].

This large potential for applications prompted the initial proposals to apply coherent or adiabatic light-matter interactions for what is now usually called subwavelength (i.e., subdiffraction-limited) localization. While the first schemes made use of spatially varying potentials [25, 37, 38], most of the following proposals and experimental demonstrations were based on spatially selective interaction with two or more laser fields of appropriate intensity profiles (see [39] and references therein). In the first part of this thesis, we focus on techniques with background in the latter category and in particular on adiabatic passage processes [40, 41] to drive a dark state in a Λ-type system of three-level atoms. Adiabatic passage processes permit efficient manipulation of population distributions in a quantum system. They offer pronounced robustness regarding variations of experimental parameters, which typically leads to threshold-like and, hence, highly nonlinear behavior with regard to laser intensities.

In the second part of this thesis, we focus on the related proposal [20–22] to utilize composite pulse (CP) sequences [42–44] for subwavelength localization and in particular for high-resolution addressing. CP sequences use a series of pulses with well-defined properties to shape the excitation probability in a two-level system driven by a single laser beam. In particular, it is possible to devise sequences that show a strong dependence on experimental parameters like the laser intensity.

In both cases—adiabatic processes and CP sequences—the steep nonlinear dependence of the coherent excitation probability upon the laser intensities allows for spatially highly localized excitation. Thus, one can create a very tight spatial confinement of population transfer, below the diameter of the driving radiation fields and even below their diffraction limit. Hence, adiabatic passage and CP sequences permit optical detection and manipulation of quantum systems at subwavelength scales.

We note that conventional applied optics already offers powerful schemes for high-resolution excitations, e.g., stimulated emission depletion (STED) [24] in nonlinear microscopy. However, STED relies on purely incoherent interactions. This is an obstacle for applications that require conservation of coherence, as, e.g., in quantum information technology. Moreover, incoherent population dynamics on single-photon transitions (e.g., depletion of an excited state by STED) vary only linearly with the driving laser intensity. Hence, the spatial confinement grows rather slowly in STED. Finally, STED requires a fast-decaying target state and therefore does not permit population transfer to a metastable state.

In this thesis, we implement and investigate two different adiabatic passage processes as well as *narrowband composite pulse* (NCP) sequences to localize atomic excitations in a rare-earth ion-doped crystal. In particular, we present our results on localization by adiabatic processes in Chapter 1. We drive the localization either by *electromagnetically induced transparency* (EIT) [26, 45] or by *stimulated Raman adiabatic passage* (STIRAP) [15]. To the best of our knowledge,

these are the first experimental implementation of EIT-driven localization in a solid and the first implementation of STIRAP for localization at all, no matter in which medium. In Chapter 2, we present and discuss NCP-based localization [20–22]. Again, this is the first experimental implementation of the technique for localization in a solid.

All of these proof-of-principle experiments operate at dimensions above the diffraction limit. Nevertheless, there is no fundamental limit to these techniques. The experimental data fully confirm the theoretical predictions and pave the way for further investigations toward subwavelength resolution.

Finally, in Chapter 3, we address a related application of CP sequences in a rare-earth ion-doped crystal: The extension of a quantum memory's storage time by application of a large number of pulses that decouple the system from environmental noise. This technique—called *dynamical decoupling* (DD) [46, 47]—suffers strongly from pulse errors that are inevitably present in any experimental setup [48, 49]. To reduce the effect of these errors, one typically uses broadband, i.e., compensating, CP sequences [42, 43, 48, 50]. We present here a simple showcase experiment in which we intentionally introduce inhomogeneity, i.e., amplitude errors, in the driving pulses and experimentally determine the performance of CP sequences to compensate for such errors.

Chapter 1

Confining Atomic Population in Space via Stimulated Raman Adiabatic Passage

1.1 Introduction

In this first chapter, we present our results on localization, driven either by EIT or STIRAP as examples for adiabatic passage processes. We published this data in the special issue "Coherent Control: Photons, Atoms and Molecules" of the Journal of Physics B [51].

The first of these techniques, EIT [52], was initially proposed for localizing population by Agarwal and Kapale [45] and later in a modified version by Yavuz and Proite [26]. Since then, it has been experimentally implemented for high-resolution localization of population in cold atomic gases, reaching spatial confinements down to 11 nm ($\lambda/50$) [27, 34, 53, 54]. However, localized excitations or population distributions in gases are short-lived due to diffusion. Moreover, care has to be taken to prevent recoil from limiting the achievable resolution [45]. In solid media, the emitters are fixed in space. Neither recoil nor diffusion effects are problems here. Nevertheless, there are no implementations of EIT for localizing population in solids yet. We also note that all implementations so far applied a standing wave geometry, which leads to an extended one-dimensional chain of population centers. In our experiment, we use a STED-like geometry, which yields a single localization spot in two dimensions [16, 19].

More recently, Mompart and coworkers proposed to apply STIRAP [41, 55] for subwavelength localization [15]. As an important finding from the theoretical treatment, the nonlinearity in STIRAP is much steeper compared to EIT. Thus, the spatial resolution increases much faster with increasing laser intensities for STIRAP than for EIT. In other words, at a given laser intensity, the population localized by STIRAP is much tighter spatially confined compared to EIT-based approaches [15, 16, 19]. So far, there are no experimental implementations of STIRAP-driven localization at all, no matter in which medium.

In this chapter, we present a convincing experimental demonstration and thorough systematic study of localizing population by STIRAP in a rare-earth ion-doped crystal and compare the results to EIT as well as numerical simulations of both approaches. The proof-of-principle experiment operates at dimensions above the diffraction limit. Nevertheless, the experimental data fully confirm the theoretical predictions and permit extrapolation toward obtaining spatially confined population in the subdiffraction regime.

1.2 Basic Theory

We review now the basic theory of localizing population, driven by EIT [26, 45] or STIRAP [15, 19]. The adiabatic passage processes rely on coherent interaction in a Λ-type three-level system with two metastable ground states coupled to a single excited state by two laser pulses (see Figure 1.1). The pump pulse drives transition $|1\rangle \leftrightarrow |2\rangle$ with Rabi frequency Ω_P, the Stokes pulse drives transition $|3\rangle \leftrightarrow |2\rangle$ with Rabi frequency Ω_S.[1] The dressed eigenstates of this coupled light-matter system include a so-called dark state given by [52]

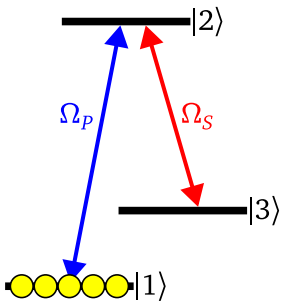

Figure 1.1: Coupling scheme for EIT and STIRAP, driven by pump (blue) and Stokes (red) beams. Yellow circles show the initial population.

$$|D(\mathbf{r})\rangle = \frac{\Omega_S(\mathbf{r})\,|1\rangle - \Omega_P(\mathbf{r})\,|3\rangle}{\sqrt{\Omega_P^2(\mathbf{r}) + \Omega_S^2(\mathbf{r})}}. \tag{1.1}$$

Since the dark state does not contain any contribution of the excited state $|2\rangle$, an atom in this state is essentially trapped therein, i.e., it can no longer be optically excited. This phenomenon is usually referred to as coherent population trapping.

Localization by EIT Let us now first consider localization by EIT. We assume that the system is in the dark state (and will later discuss how to transfer it into this state). In this case, the population distribution of the bare states $|1\rangle$ and $|3\rangle$ depends solely upon the ratio $\Omega_P(\mathbf{r})/\Omega_S(\mathbf{r})$ and, hence, it varies across the laser intensity profiles. As an instructive example, let us assume a beam geometry similar to STED, i.e., a Laguerre-Gaussian "donut" mode for the pump beam profile

$$\Omega_P(\mathbf{r}) = \Omega_{P0}\frac{r}{w_P}e^{-r^2/w_P^2} \tag{1.2}$$

and a Gaussian mode for the Stokes beam profile

$$\Omega_S(\mathbf{r}) = \Omega_{S0}e^{-r^2/w_S^2}. \tag{1.3}$$

Here, r is the radial coordinate, Ω_{i0} are the peak coupling strengths, and w_i, with $i = P,S$, are the beam waists. Close to the node of the pump beam, we have $\Omega_P \ll \Omega_S$. Thus, we get $|D\rangle = |1\rangle$ at the node, whereas further out (provided that $\Omega_{P0} > \Omega_{S0}$)[2] we have $|D\rangle \approx |3\rangle$. Hence, due to the spatial variation in $\Omega_P(\mathbf{r})/\Omega_S(\mathbf{r})$, the system remains in state $|1\rangle$ only in a spatially tightly confined region around the intensity node of the pump beam. Thus, the population P_1 defined as the density matrix element ρ_{11} has a sharp peak at the pump intensity node (see Figure 1.2). The population in state $|3\rangle$ shows the opposite behavior, i.e., a sharp

[1] We note that for consistency, throughout this chapter we use the typical STIRAP nomenclature "pump" and "Stokes" also for EIT, where the pulses are otherwise usually termed "probe" and "control".

[2] We note that EIT typically requires $\Omega_{P0} \ll \Omega_{S0}$ instead [52].

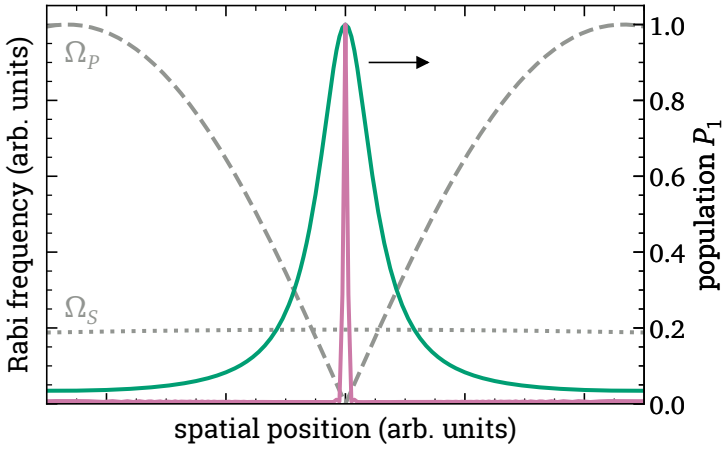

Figure 1.2: Localization via the dark state: Remaining population P_1 in state $|1\rangle$ vs. spatial position for EIT (green line) and STIRAP (purple line). We assume a Gaussian Stokes beam profile, i.e., almost constant Rabi frequency Ω_S (see gray, dotted line), and a donut-shaped pump beam profile, i.e., a node in Ω_P (see gray, dashed line).

dip at the center of the donut pump profile (not depicted in Figure 1.2).

We note that this behavior is a disadvantage for applications that aim at controlling a single quantum emitter, e.g., in high-resolution addressing for quantum computers, since the emitter in the center of the pump profile remains in its initial state while all other emitters are modified. Hence, in this case, one has to apply inversion after the localization, which can induce an additional unwanted phase. However, many other applications, like, e.g., the preparation of a spatially multiplexed quantum memory, the generation of waveguide-like structures, lithography, or microscopy, require only a localized population distribution. Here, it would easily be possible to exchange the occurrence of a peak or a dip in the spatial population patterns of the two states $|1\rangle$ and $|3\rangle$, by preparing the system initially in the other ground state (for reasons discussed below) and exchanging the beam profiles of the pump and Stokes pulses.

In any case, the localization gets tighter when Ω_{P0} increases, as the condition $\Omega_P > \Omega_S$ is fulfilled closer to the center of the node (see Figure 1.3(c)). To calculate the width (full width at half maximum (FWHM)) of the localized population, we define it straightforwardly as twice the radius r_0 at which $P_1(r_0) = 0.5$. From Equation (1.1) and using the beam profiles (1.2) and (1.3), it is easy to see that this requires

$$\Omega_P(r_0) = \Omega_{P0}\frac{r_0}{w_P}e^{-r_0^2/w_P^2} \stackrel{!}{=} \Omega_{S0}e^{-r_0^2/w_S^2} = \Omega_S(r_0). \tag{1.4}$$

We can now expand this equation to first order to obtain

$$\Omega_{P0}\frac{r_0}{w_P} = \Omega_{S0} \tag{1.5}$$

and finally solve for r_0 to find the width

$$\Delta r \equiv 2r_0 = \frac{2w_P}{\sqrt{R}} \tag{1.6}$$

where we define $R = \Omega_{P0}^2/\Omega_{S0}^2$. This clearly shows, as expected, that the localization improves with increasing R, i.e., increasing pump Rabi frequency—which is proportional to the electric field of the driving radiation.

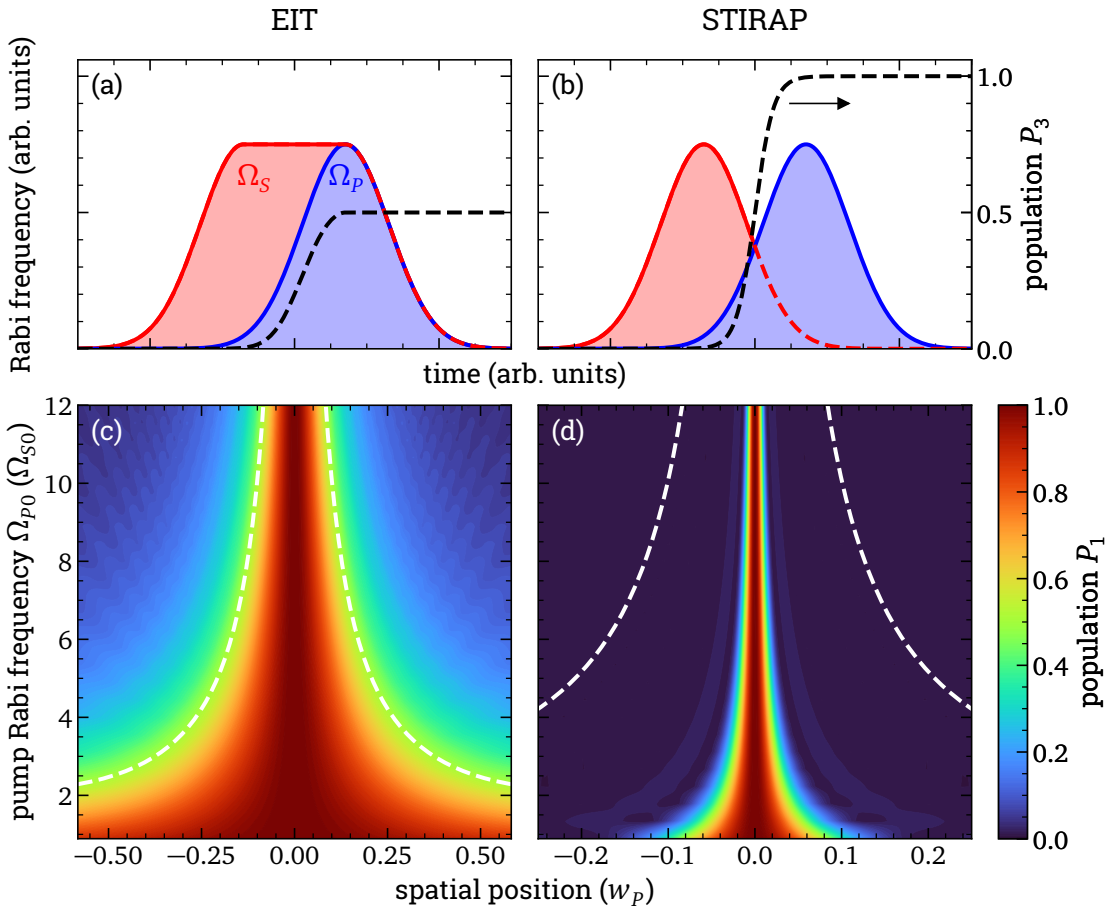

Figure 1.3: Localization via the dark state using EIT (left) or STIRAP (right). The top row shows the temporal profile of the Stokes (blue) and pump (red) Rabi frequency with $\Omega_{P0} = \Omega_{S0}$, as well as the population P_3 in state $|3\rangle$ (black, dashed line). The bottom row shows the population P_1 remaining in state $|1\rangle$ vs. spatial position and (peak) pump Rabi frequency. We assume a Gaussian-shaped Stokes profile and a donut-shaped pump profile. The white, dashed lines show where $\Omega_P(\mathbf{r}) = \Omega_S(\mathbf{r})$. Note the different scales of the horizontal axes.

There are several ways to transfer the system to the dark state. Let us assume that initially the population is in state $|1\rangle$. The initial proposal suggested coincident pump and Stokes pulses with equal temporal intensity profiles to optically pump the system to the dark state [45]. This requires, however, that the pulses are much longer than the lifetime T_1^e of the excited state $|2\rangle$. Otherwise, the localized population pattern in space broadens [56] and diabatic coupling causes complicated, oscillatory behavior in the wings [54]. Furthermore, the transfer involving decay is incoherent and not applicable for, e.g., quantum technology. Therefore, following work on EIT-based localization [26, 34, 53, 54] used a counter-intuitive sequence of shaped pulses that already resembles fractional STIRAP [55] as illustrated in Figure 1.3(a). We still assume that the system is initially in state $|1\rangle$, i.e., $P_3 = 0$, but here, the Stokes pulse precedes the pump pulse such that initially $\Omega_P < \Omega_S$. Hence, at first, the system is in the dark state $|D\rangle = |1\rangle$. If the pump beam then turns on sufficiently slow and temporally overlapping with the Stokes pulse, the system adiabatically follows the dark state into the spatially varying

superposition of $|1\rangle$ and $|3\rangle$. Finally, the pulses end simultaneously to maintain a constant ratio $\Omega_P(\mathbf{r})/\Omega_S(\mathbf{r})$, which ensures that the system remains in the dark state. Compared to the initial proposal [45], this approach maintains coherence. However, the achieved spatial confinement of the population remains the same. Moreover, the protocol is very sensitive to variations of the shape of the falling edges of the pulses.

Localization by STIRAP In more recent theory work, Mompart and coworkers proposed to apply the full, standard STIRAP process for subwavelength localization [15]. This approach requires appropriately delayed pump and Stokes pulses only, without the need for specific pulse shapes, e.g., in the falling edges. For STIRAP, the Stokes pulse precedes the pump pulse, as illustrated in Figure 1.3(b). We assume that the system is initially in state $|1\rangle$, i.e., the population in state $|3\rangle$ is $P_3 = 0$. Hence, at early times, when $\Omega_P < \Omega_S$, the system is in the dark state $|D\rangle = |1\rangle$. At late times, when $\Omega_P > \Omega_S$, the dark state and thus the system have evolved into the target state $|D\rangle = |3\rangle$, i.e., $P_3 = 1$. This is the essence of complete, adiabatic population transfer from state $|1\rangle$ to state $|3\rangle$ by STIRAP. The process is robust, i.e., the population dynamics do not change when the experimental parameters fluctuate—provided some limits are kept in view. If we apply the geometry of a donut pump and a Gaussian Stokes beam for STIRAP, no population is transferred in a tight region around the node of the pump field, whereas the robustness of STIRAP ensures almost perfect transfer everywhere else. The larger the peak intensity in the beam, the tighter the region where population remains in state $|1\rangle$ (see Figure 1.3(d)).

Efficient STIRAP requires fulfillment of the local adiabaticity condition [40]

$$\sqrt{\Omega_S^2(t) + \Omega_P^2(t)} \gg \frac{|\Omega_S(t)\dot{\Omega}_P(t) - \Omega_P(t)\dot{\Omega}_S(t)|}{\Omega_P^2(t) + \Omega_S^2(t)} \tag{1.7}$$

at all times t. Here, the left side describes the energy splitting of the dressed states in the coupled system, and the right side is the rate of change of the dark state composition. In other words, the dark state has to evolve slowly compared to the energy splitting to prevent coupling between the dressed states. As long as this condition is fulfilled, the system follows the dark state, i.e., STIRAP transfers the population efficiently.

For smooth pulse shapes, we can also derive a simpler global adiabaticity condition by integrating Equation (1.7). We obtain [40]

$$\left(\Omega_S^2(\mathbf{r}) + \Omega_P^2(\mathbf{r})\right) T^2 \geq A_0^2 \tag{1.8}$$

where T is the delay between the pulses, i.e., approximately the interaction time, and $A_0 \gg \pi/2$ is a minimal pulse area (i.e., the product of Rabi frequency and pulse duration) necessary for efficient transfer. In the terminology of incoherent excitation, the large pulse area simply corresponds to the saturation of a transition.

One has to choose the value of A_0 such that fulfillment of the global adiabaticity condition (1.8) implies fulfillment of the stricter local condition (1.7). Thus, typically, STIRAP demands $A_0 \approx 10$ [40]. However, this value assumes equal

peak Rabi frequencies, i.e., equal pulse areas, of pump and Stokes, as is often the case in STIRAP experiments. Yet in our experiment, in particular close to the center of the pump node, the pulse areas are not identical. Let us illustrate this difference with a simple example where we consider a large Stokes pulse area $\Omega_S T > A_0 = 10$. Then, even for $\Omega_P \approx 0$, Inequality (1.8) would be fulfilled, even though there would obviously be no population transfer. This is because the local adiabaticity condition would not be fulfilled at all times, as one can confirm easily by inserting Gaussian profiles with $\Omega_{P0} T \gtrsim 0$ and $\Omega_{S0} T \gg \pi/2$ into Inequality (1.7). Indeed, from numerical simulation studies, we find that efficient STIRAP with $\Omega_S T \gg \pi/2$ still requires a minimum pump pulse area $\Omega_P T > 0$ to guarantee adiabaticity. However, we find that $\Omega_P T \ll \Omega_S T$ is sufficient and, hence, in this case, $A_0 \gtrsim \Omega_S T$ is a good choice for the global adiabaticity condition.

From this, we already see that STIRAP reaches much stronger spatial confinement of population patterns compared to EIT (see Figure 1.2). Let us review the requirements for efficient population transfer from state $|1\rangle$ to state $|3\rangle$: When using EIT, we need $\Omega_P \gg \Omega_S$ to ensure $|D\rangle \approx |3\rangle$, whereas in STIRAP, fulfillment of the adiabaticity condition suffices. As we just discussed, the latter is already guaranteed for $\Omega_P \ll \Omega_S$, i.e., much closer to the node of the pump profile. Hence, STIRAP gives us a much stronger confinement of the population in state $|1\rangle$.

To find the diameter (FWHM) of the region around the pump node, where the atoms are left in state $|1\rangle$ when using STIRAP, we follow the approach by Viscor and coworkers [19]: We insert the beam profiles (1.2) and (1.3) into the adiabaticity condition (1.8) to obtain

$$\left(\Omega_{P0}^2 \frac{r^2}{w_P^2} e^{-2r^2/w_P^2} + \Omega_{S0}^2 e^{-2r^2/w_S^2}\right) T^2 \geq A_0^2. \tag{1.9}$$

We expand this inequality to second order and use the equality to define a spatial threshold r_{th} for successful STIRAP:

$$\left(\Omega_{P0}^2 \frac{r_{th}^2}{w_P^2} + \Omega_{S0}^2 \left(1 - 2\frac{r_{th}^2}{w_S^2}\right)\right) T^2 \stackrel{!}{=} A_0^2. \tag{1.10}$$

Finally, we solve for r_{th} and assume that the diameter of the localized population is equal to this threshold to obtain

$$\Delta r \equiv r_{th} = w_P \sqrt{\frac{\left(\frac{A_0}{T\Omega_{S0}}\right)^2 - 1}{R - 2\frac{w_P^2}{w_S^2}}}. \tag{1.11}$$

Since $A_0 \gtrsim \Omega_{S0} T$, comparing Equations (1.6) and (1.11) reveals that STIRAP reaches much stronger spatial confinement of population patterns and converges much faster with increasing laser intensity toward tight localization compared to EIT (see Figures 1.2, 1.3(c), and 1.3(d)) [15, 16, 19]. Moreover, the pulse sequence of STIRAP is easy to implement and robust with regard also to fluctuations in the pulse shape or other experimental parameters. The process maintains coherence and produces no recoil.

1.3 Experimental Setup

1.3.1 Orbital Angular Momentum Modes

Let us consider the required pump profile with a central intensity node again. So far, we simply assumed a "donut"-shaped pump beam with a cusp in the intensity node. We note that this cusp is not required for subwavelength localization; a smooth Rabi frequency distribution with a dark center would be sufficient. The latter could be generated by simply imaging a mask or with diffractive optical elements. However, a cusp improves the confinement, since here the Rabi frequency increases faster with the radial coordinate.

Hence, let us consider Laguerre-Gaussian modes—the generalization of the "donut" profile—in more detail. At the focus $z = 0$ they are given by [57]

$$LG_p^l(\mathbf{r}) \propto \left(\frac{r}{w}\right)^{|l|} L_p^l\left(\frac{2r^2}{w^2}\right) e^{-r^2/w^2} e^{il\Phi} \tag{1.12}$$

where Φ is the azimuth angle and the associate Laguerre polynomial L_p^l is defined by the two integer quantum numbers l and p. Note that for $l = 1$, $p = 0$ and by taking the absolute value, i.e., neglecting the phase, Equation (1.12) reduces to the previously considered pump profile (1.2).

In general, the wavefronts of Laguerre-Gaussian beams with $l \neq 0$ are l intertwined helical surfaces around the propagation axis z with a step length of $|l|\lambda$ (see Figure 1.4(a)). For fixed z, on the other hand, the phase of the beam increases by $2\pi \times l$ when going around the origin (see Figure 1.4(b)). This behavior results in a phase singularity at $r = 0$, i.e., a point where the phase of the beam is multiply defined and hence the amplitude necessarily drops to zero, causing the desired intensity node—an optical vortex (see Figure 1.4(c)). The quantum number l is also called the topological charge of the vortex and is further connected to the

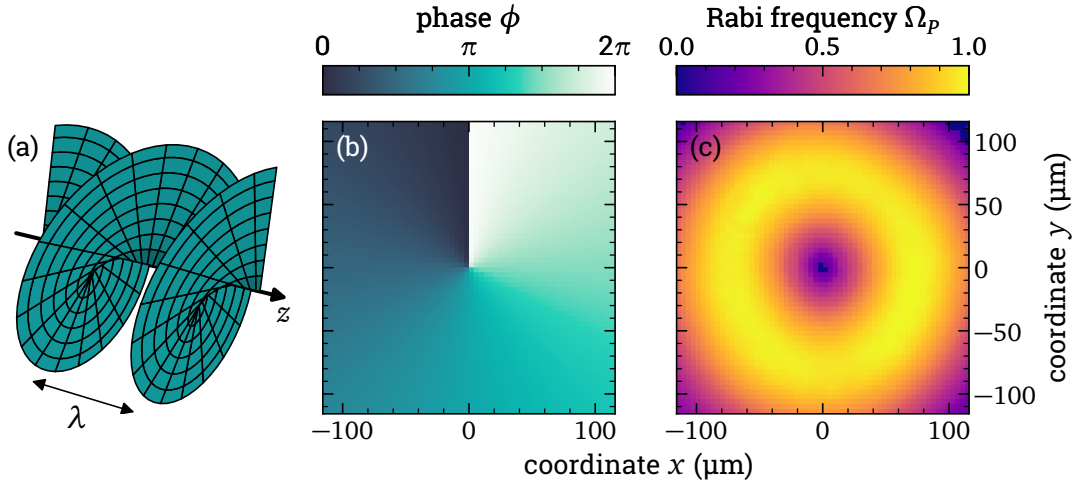

Figure 1.4: Schematic depiction of a Laguerre-Gaussian mode (1.12) with $l = 1$, $p = 0$. (a) A wavefront of the beam along the propagation axis z. (b) Phase ϕ vs. coordinates x and y at $z = 0$. (c) Measured Rabi frequency vs. coordinates x and y.

orbital angular momentum of the beam [57–59] (not to be confused with its polarization) which has a value of $l\hbar$ per photon. The second quantum number p gives the number of π phase steps in the radial direction. This causes an intensity profile consisting of $p+1$ rings whose radius scales with $\sqrt{l}$ [60]. Since we are interested in a single ring with a small radius (such that the confinement is as strong as possible), we only consider the case of $l = 1$, $p = 0$ in the following. We further note, that other singularities, e.g., in polarization, cause intensity nodes as well [59]. However, the transition moment in Pr^{3+}:Y_2SiO_5 is polarization dependent [61] which makes this approach incompatible with our medium.

Laguerre-Gaussian modes can be generated by various methods including fork-gratings, mode conversion, q-plates and spiral phase plates [57, 59]. The latter are useful in particular due to their simplicity. Hence, we also apply them in our experiments. As illustrated in Figure 1.5, spiral phase plates are optical elements with spirally (and radially for $p > 0$) increasing (effective) thickness. They imprint the Laguerre-Gaussian phase distribution onto a Gaussian beam due to the spatially varying retardation associated with the changing optical path length. Note that due to manufacturing limitations, the thickness typically does not increase continuously around the central axis but in steps. It was shown, however, that about 10 steps are sufficient to generate Laguerre-Gaussian modes with high purity [62].

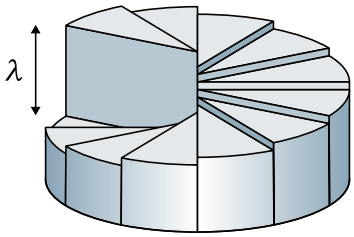

Figure 1.5: Schematic depiction of a spiral phase plate with charge $l = 1$ and 12 steps.

1.3.2 The Rare-Earth Ion-Doped Medium Pr:YSO

We implement our experiments on localizing population by adiabatic passage in a Pr^{3+}:Y_2SiO_5 (from now on simply termed Pr:YSO) crystal, which we describe here only briefly to introduce its relevant parameters. For more details, see [63]. We employ the hyperfine states of the optical transition $^3H_4(0) \leftrightarrow {}^1D_2(0)$,[3] at a center wavelength of 605.98 nm. We specifically choose the hyperfine states $|1\rangle = {}^3H_4(0)\,|m_I = \pm 3/2\rangle$, $|3\rangle = {}^3H_4(0)\,|m_I = \pm 1/2\rangle$, and $|2\rangle = {}^1D_2(0)\,|m_I = \pm 1/2\rangle$ for our experiments (see Figure 1.6) due to their corresponding favorable transition moments [64] but note that in principle we could utilize any of the hyperfine states for localization. The excited state population lifetime in Pr:YSO is $T_1^e = 164\,\mu s$, whereas the ground state lifetime is $T_1^g = 100\,s$. The latter is an attractive feature, as the population patterns in space driven by STIRAP or EIT live very long. The decoherence time $T_2^g = 500\,\mu s$ among the

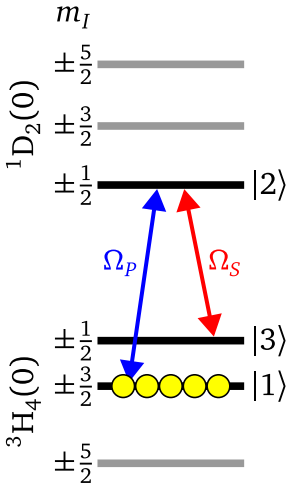

Figure 1.6: Coupling scheme for the experiments on adiabatic localization in Pr:YSO with the pump (blue) and Stokes (red) lasers. Yellow circles show the initial population.

[3] Russel-Saunders notation $^{2S+1}L_J$. (0) indicates the lowest crystal field state.

ground states sets an upper limit for the interaction time with the driving light fields, i.e., the maximal pulse duration and pulse delay.

The optical transition in Pr:YSO is inhomogeneously broadened to several GHz, while the hyperfine state separation is only on the order of 10 MHz. Hence, a single frequency laser couples all possible transitions in ions from different frequency ensembles within the inhomogeneous linewidth. Thus, we use an optical pumping sequence to prepare the required level scheme and population distribution. This preparation sequence starts by burning a spectral pit that contains both the pump and Stokes transition, followed by a repump pulse to create an antihole on the pump transition with a residual inhomogeneous broadening below 100 kHz. Finally, a cleaning pulse removes unwanted population from state $|3\rangle$ to create the desired Λ-system with the population initially in state $|1\rangle$ (see Figure 1.6). For more details on the preparation sequence, see [64, 65].

1.3.3 Optical Setup

Figure 1.7 depicts our experimental setup around the Pr:YSO crystal (length 1 mm, dopant concentration 0.05 %) which we cool to temperatures below 4 K in a continuous flow cryostat[4]. We derive all laser beams in the experiment from a fiber laser[5] pumped optical parametric oscillator[6] with internal sum frequency generation. The system yields up to 400 mW of optical power at the experiment and its stabilized[7] laser linewidth is well below 100 kHz (FWHM). For details on the laser system, see [66, 67]. We can control each beamline in the experiment in intensity and frequency using acousto-optic modulators[8] driven by direct digital synthesis drivers[9], to generate preparation, pump, Stokes, and probe pulses with appropriate temporal pulse shapes, durations, and timings. An I/O card[10] and home-made LabVIEW software control the entire experimental sequence.

The pump beam first passes a spatial filter consisting of a pinhole in the focus of a telescope (not shown in Figure 1.7) to ensure a high-quality Gaussian intensity distribution in space. Afterward, a spiral phase plate[11] with charge $l = 1$ converts the pump beam mode to a Laguerre-Gaussian "donut"-like intensity profile, as discussed above. We mildly focus the pump beam into the crystal with lens L1 (focal length 200 mm), yielding a beam waist of $w_P = 100\,\mu\text{m}$.

The Stokes beam (which we also use for the optical preparation of the medium) counterpropagates to the pump beam with a small angle of about 2° in between. We collimate this beam into the crystal with lenses L2 (focal length 150 mm) and L3 (focal length 60 mm), yielding a beam waist of $w_S = 250\,\mu\text{m}$ at the position of the crystal. This large size compared to the pump beam ensures a smaller

[4] ST-100, Janis Research Co.
[5] YAR-15K-1064-LP-SF, IPG Photonics pumping Koheras AdjustiK Y10 PM FM, NKT Photonics
[6] based on Argos Model 2400 SF-15, Lockheed Martin Aculight [66, 67]
[7] using DigiLock 110, Toptica Photonics and a home-made high finesse cavity [67]
[8] pump: AOMO 380-125, Gooch & Housego; Stokes & probe: BRI-TEF-80-50-.606, Brimrose
[9] pump & probe: AODS 20160-1, Crystal Technology; Stokes: DDSPA-B8b23b-0, AA Opto-Electronic
[10] PCIe-6363, National Instruments
[11] V-593-20-1, Vortex Photonics

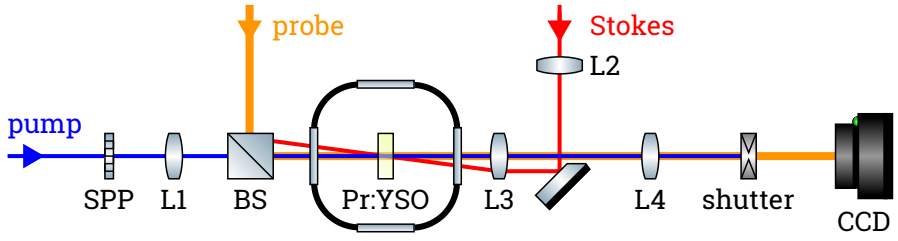

Figure 1.7: Experimental setup with pump (blue), Stokes (red), and probe (orange) beamlines, Pr:YSO crystal (green), spiral phase plate (SPP), beam splitter (BS), lenses (L), and CCD camera.

modulation of the Stokes Rabi frequency and a homogeneous optical preparation of the medium across the interaction region.

Imaging System To determine the spatially varying population distribution after adiabatic passage, we measure the transmission across a probe laser beam profile when we tune the probe laser frequency in the range of the pump and Stokes transitions. The probe beam copropagates with the pump beam, but is temporally well separated from the STIRAP pulses by roughly 7 ms. The delay is much longer than the lifetime of the excited state $T_1^e = 164\,\mu s$. Hence, there is no residual population in state $|2\rangle$ when the probe pulse interacts with the medium, i.e., all population is in the ground states $|1\rangle$ and $|3\rangle$. The probe beam has a beam waist of 290 µm in the crystal, i.e., much larger than the pump profile, to cover the full interaction region. We image the probe beam profile onto a CCD camera[12] using a simple imaging system consisting of lenses L3 and L4 (focal length 300 mm). A mechanical shutter[13] prevents saturation of the camera caused by the pump beam or back reflections of the Stokes beam.

From the probe beam intensity profile at the CCD camera, we determine the probe transmissions $\mathcal{T}_1$ at the pump transition $|1\rangle \leftrightarrow |2\rangle$ and $\mathcal{T}_3$ at the Stokes transition $|3\rangle \leftrightarrow |2\rangle$ for each pixel. We compare these values to the maximal transmission $\mathcal{T}_0$ through the optical setup, measured during the preparation sequence when the crystal should be fully transparent. After subtracting a background measurement, this allows us to determine the spatial distribution of the optical depths $OD_i = -\ln(\mathcal{T}_i/\mathcal{T}_0)$ at the pump and Stokes transitions. From there, we calculate the populations

$$P_1 = 1 - P_3 = 1 - \frac{1}{1+X} \text{ with } X = \frac{OD_1}{OD_3}\frac{\mu_{32}}{\mu_{12}} \tag{1.13}$$

where μ_{ij} is the transition moment of the transition $|i\rangle \leftrightarrow |j\rangle$. We note that, in principle, a single transition would also be sufficient to determine the population distribution in the initial and target states. However, measuring at both the pump and Stokes transition yields a larger signal-to-noise ratio [69].

We determine the magnification and resolution of the imaging system with a

[12] Prosilica GC1290, Allied Vision
[13] home-made, based on [68]

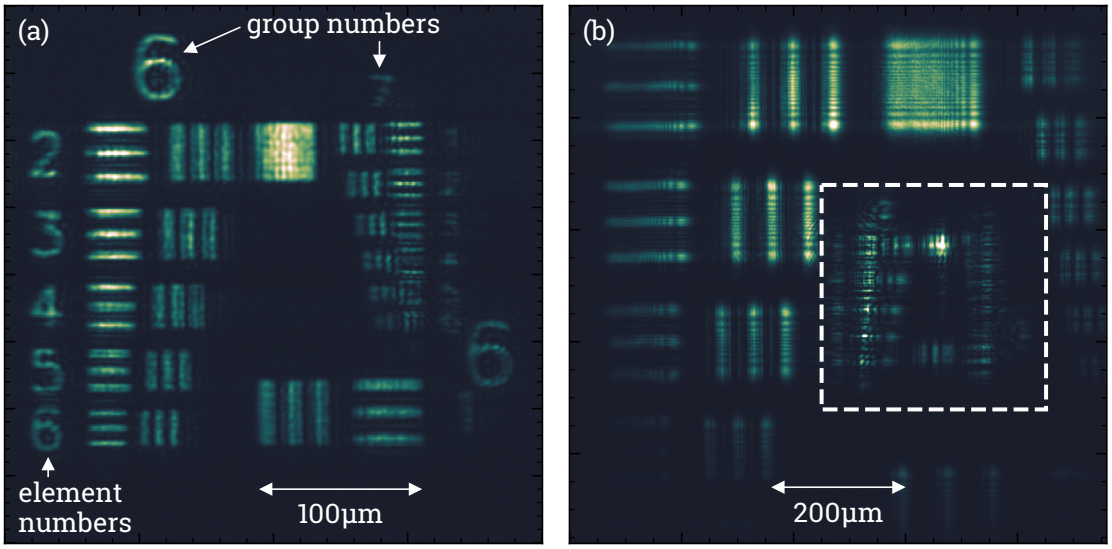

Figure 1.8: Images of a USAF-1951 target mask using the imaging setup described in the main text. (a) Groups 6 and 7 with the mask in the focus of the imaging system. (b) Groups 4 to 7 with the mask 0.5 mm closer to the CCD camera than in (a). The white, dashed square indicates the section shown in (a).

USAF-1951 target mask placed in the beamlines instead of the crystal. This mask consists of seven groups of six elements each. Every such element contains three horizontal and three vertical lines. The higher the group and element number, the thinner are these lines. In Figure 1.8(a) we show the transmission through the mask imaged onto the CCD camera. We can clearly see the structure of the mask, and in particular groups 6 (lower left) and 7 (upper right). The smallest resolvable element is 7-3 with a line thickness of 3.1 µm which gives us a resolution only slightly larger than the diffraction limit of 2.7 µm given by the numerical aperture NA ≈ 0.23 of the system. From the same data, we also calculate the magnification of 4.68 which fits with the ratio of the focal lengths of lenses L2 and L3.

However, the mask has a negligible thickness, while our crystal is 1 mm thick. This reduces the resolution in the experiment. We can see this in Figure 1.8(b), where we move the mask by 0.5 mm, i.e., half the crystal thickness, toward the CCD camera. Due to its limited depth of field, the imaging system can no longer resolve groups 6 and 7 (indicated by the white dashed square). At most, we can still surmise the structure of element 6-1. The smallest, clearly visible element is 5-4 (on the right), which has a nominal line thickness of 11.05 µm. Hence, for the entire crystal thickness, we estimate a resolution of about 10 µm.

Time Sequence Figure 1.9 shows the time sequence of our experiment: (i) Preparation pulse sequence using optical pumping to provide full transparency for both Stokes and pump transition. (ii) Transmission measurement of a probe pulse as reference. (iii) Preparation pulse sequence to provide a Λ-system. (iv) STIRAP or EIT pulse sequence to drive localization. (v) Transmission measurement of a probe pulse to determine population patterns generated by STIRAP or EIT. We repeat the sequence (i–v) and average the resulting images to reduce noise.

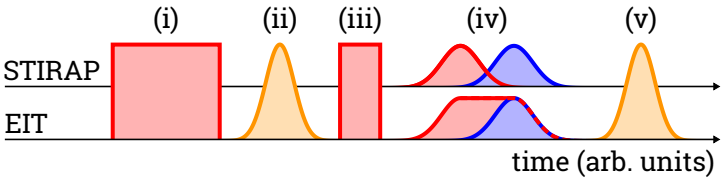

Figure 1.9: Time sequences of optical pulses (see main text). Colors correspond to beamlines from Figure 1.7.

Determination of Rabi Frequencies To compare the results of our measurements to a numerical simulation, we require exact values of pump and Stokes Rabi frequencies, as they vary across the laser beam profiles at the position of the crystal. It would not be very accurate to calculate the Rabi frequencies from the laser intensity beam profiles, as uncertainties in the intensity and transition moments would add up. Hence, we decided to measure the Rabi frequencies directly through spatially resolved observation of Rabi oscillations across the laser beam profiles. For this purpose, we employ the same time sequence as discussed above (see Figure 1.9) but replace the STIRAP/EIT pulses (iv) with a single pump or Stokes pulse of rectangular pulse shape in time. In the case of the Stokes pulse, we also change the optical pumping sequence such that the population is initially prepared in state $|3\rangle$. For each pixel of the CCD camera, we determine by a transmission measurement the amount of population left in the ground state of the transition when we vary the pump/Stokes pulse duration. Since this population oscillates with the Rabi frequency, we get spatially resolved information on the latter across the laser profiles. As an example for the application of this method, Figure 1.4(c) shows the spatial variation of the pump Rabi frequency across the donut-shaped pump beam.

1.4 Experimental Results

1.4.1 Localizing Population by STIRAP

We now discuss our experiments on localization driven by STIRAP. We apply the time sequence discussed above and presented in Figure 1.9. In particular, we choose pulses with a Gaussian intensity profile in time with a duration (FWHM) of $\tau \equiv \tau_P = \tau_S = 25\,\mu s$, i.e., well below the ground state decoherence time $T_2^g = 500\,\mu s$. The pump pulse follows the Stokes pulse with a time delay of $T = 25\,\mu s$. We found that the exact value of the time delay is not relevant (as expected for STIRAP) as long as it matches the pulse duration to about 50 %, i.e., $0.5\tau < T < 1.5\tau$, and hence choose $T = \tau$. For systematic measurements, we keep the peak Stokes Rabi frequency at $\Omega_{S0} = 2\pi \times 225\,\text{kHz}$ and vary the peak pump Rabi frequency Ω_{P0} from 0 to $2\pi \times 2710\,\text{kHz}$ (limited by the available laser power). For each value of Ω_{P0} (i.e., ratio R of the peak Rabi frequencies), we measure the population P_1 with a probe pulse of Gaussian intensity profile in time with a duration (FWHM) of 10 µs and a peak Rabi frequency of roughly $2\pi \times 8\,\text{kHz}$, which leads to only negligible change of the population distribution. We expose the CCD camera to radiation for 40 µs, which ensures detection of the entire probe pulse.

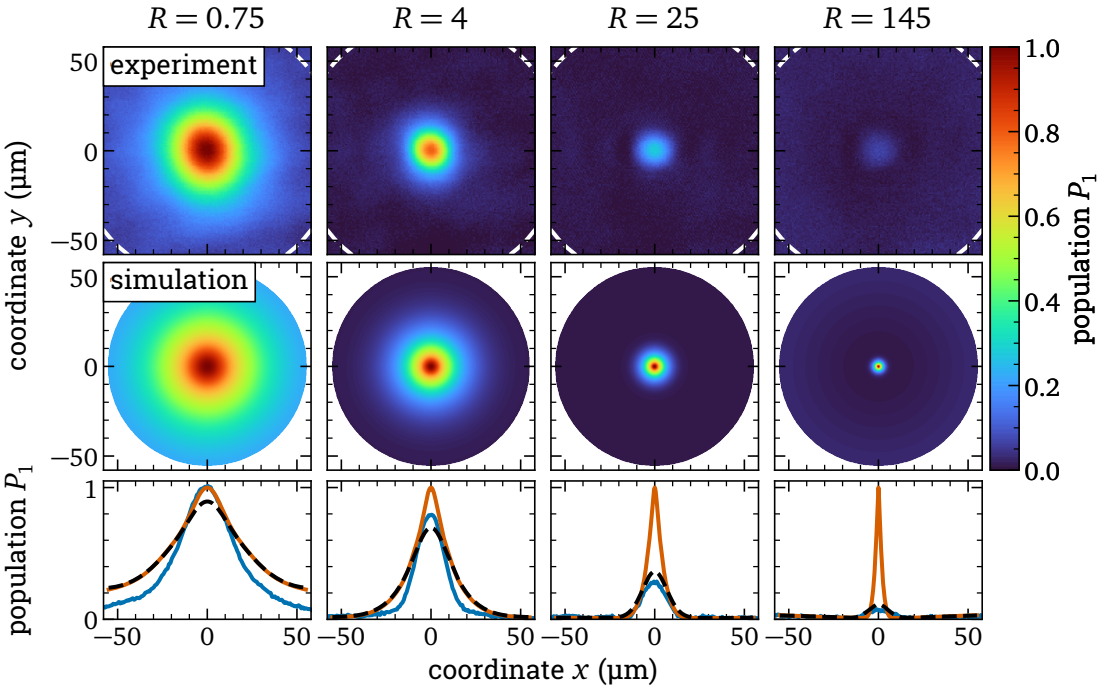

Figure 1.10: STIRAP-driven localization in Pr:YSO. Variation of the population $P_1(x, y)$ vs. coordinates x and y across the laser beam profiles. (upper row) Experimental data for different values of R. The white, dashed line indicates the diameter of the pump beam defined by the position of the ring at maximal pump intensity. (middle row) Numerical simulations with the experimentally determined parameters. (lower row) Cuts through the experimental data (blue line), simulation (orange line), and spatially filtered simulation (black, dashed line).

The top row of Figure 1.10 shows the experimentally measured population distributions after the STIRAP process for selected values of R. The bottom row shows cuts (indicated by blue lines) through the central peaks. Obviously, the remaining population in state $|1\rangle$, described by P_1, is localized in the center of the donut pump beam. Already at $R = 0.75$, the population is well confined below the pump beam diameter. This is already clear evidence for adiabatically driven localization. The extension of the population region shrinks with increasing pump laser intensity (i.e., larger values of R), as expected. We also see that for ratios $R \geq 4$, the background population essentially reduces to zero, confirming the almost perfect transfer by STIRAP as soon as the pump Rabi frequency is sufficiently large to fulfill the adiabaticity condition (1.8).

However, it is also apparent that for $R \geq 25$, the extension of the population confinement seems to remain approximately constant at $\Delta r \approx 15\,\mu\text{m}$, while only its amplitude decreases further. This is due to the extension of the crystal in the propagation direction and the limited depth of field in our imaging system. As discussed before, our imaging system has a diffraction-limited resolution of about 3 µm at its focus, but the resolution for an object 0.5 mm (i.e., half the crystal thickness) outside the focus is only about 10 µm. Thus, even larger structures outside the focus are not well imaged and smear out. When we image the population distribution in the crystal, our imaging system averages this distribution in the propagation direction and thus washes out the population distribution due to the

lower resolution at the edges of the crystal.

We also note that the peak population in the center of the pump profile most likely slightly deviates from the maximal value of one, as there is some residual intensity > 0 in the pump node. We confirmed experimentally that this intensity is at most 0.1 % of the peak intensity, and as such, it does not cause more than 40 % loss of population even for the highest Ω_{P0}. Furthermore, since the resolution of our imaging system also limited this measurement, we can safely assume that the real intensity in the profile center and thus the population loss are actually much lower than that.

We compare the results of our measurement with a straightforward numerical simulation based on a density matrix calculation of the Λ-system in Pr:YSO, interacting with pump and Stokes pulses [52]. The calculation also takes the decay of the excited state $|2\rangle$, the limited decoherence time among the ground states $|1\rangle$ and $|3\rangle$, and inhomogeneous broadenings of the optical and hyperfine transitions into account. In the calculation, we use fits to the spatial variations of pump and Stokes Rabi frequencies, as experimentally determined from measurements of Rabi oscillations (see above), and set all other pulse parameters to be the same as in the experiment. To reduce the required calculation time, we assume rotational symmetry in the beam profiles. The middle row of Figure 1.10 shows the results of the simulation. The orange lines in the bottom row indicate cuts through the central peaks in the two-dimensional plots of the simulations. For low values of R we see good agreement between the simulations and the experimental data, with some small offset in the wings. We suspect that this is caused by a small mismatch between the simulation parameters and the experiment. The sensitivity of STIRAP at low pump Rabi frequencies, e.g., as is here the case in the wings of the beam profile, then causes the small visible deviation. At larger values of R the simulation deviates from the experiment—as expected, when our imaging system washes the narrow population distributions out. We mimic the latter imaging effect in our simulation by applying a simple two-dimensional Gaussian filter with a width (FWHM) of 12 µm and show the resulting profiles as black, dashed lines in the bottom row of Figure 1.10. Now we see a good agreement with the experimental data (blue lines), especially for large values of R.

We analyze the experimental data now in more detail to obtain some more information on the localization process also for large values of R, even if the imaging system washes out the effect of stronger spatial confinements. In Figure 1.11 we plot the width Δr (FWHM) of the region with population confined by STIRAP vs. R (blue circles). The plot also shows results from our simulation (orange triangles) and the analytic treatment (1.11), for which we use the experimentally determined parameters and $A_0 = 38$ (black line).[14] As discussed before, we see that the width of the localized population is limited to 15 µm and does not match the expectation. This is due to the limitations of the imaging system.

Let us draw our attention again to the two-dimensional plots in the top row of Figure 1.10: We see that for large values of R the region with localized population does not shrink any further (as we already discussed), but it becomes fainter, i.e., the maximal signal decreases. We also see this in the cuts in the bottom row of

[14] For comparison, $\Omega_{S0} T \approx 35$.

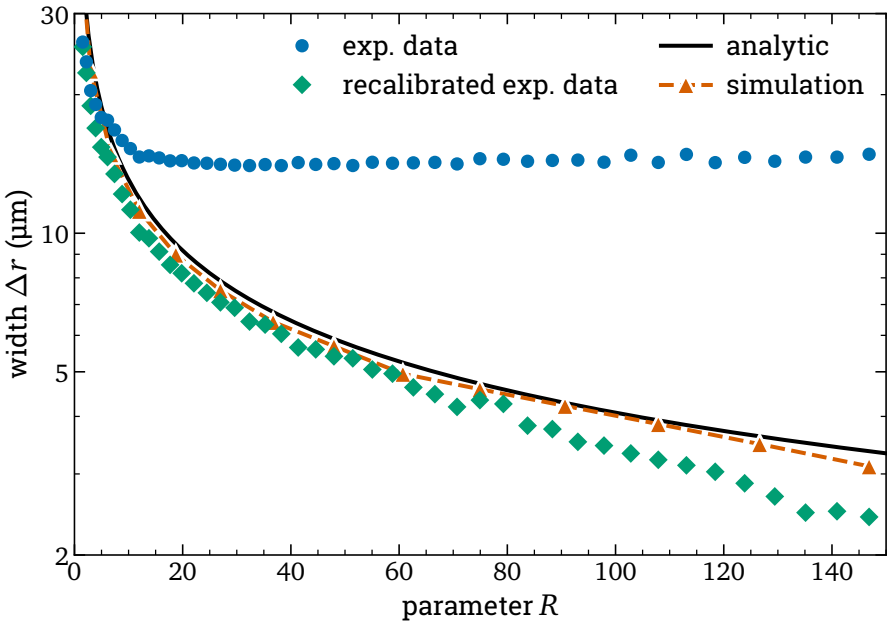

Figure 1.11: Width Δr (FWHM) of the population distribution $P_1(x, y)$ after localization by STIRAP vs. R. Comparison of the width calculated from Equation (1.11) (black line), numerical simulation (orange triangles), experimental data (blue circles), and recalibrated experimental data taking limited imaging resolution into account (green squares). Note the logarithmically spaced ticks of the vertical axis.

Figure 1.10, where the amplitude decreases for larger values of R. This can be explained by the fact that the stronger STIRAP spatially confines the population, the fewer quantum emitters are selected by the process and contribute to the signal. In other words, the integral of the signal is proportional to the number of quantum emitters spatially selected by STIRAP. This holds true irrespective of the spatial resolution of the imaging system, i.e., if the imaging system limits the measured width, the amplitude has to decrease.

This gives us a handle to infer the true width of the localized population from resolution-limited experimental data. To do so, we rescale the fits to the experimental data (e.g., the blue lines in the bottom row of Figure 1.10), such that they reach a peak height of 1, while reducing their width such that the integral remains the same. We show the resulting, recalibrated widths of the localized population as green squares in Figure 1.11. They are in much better agreement now with the numerical simulation and analytic treatment. We assume that the remaining discrepancy is due to the reduced peak population caused by residual intensity in the center of the pump profile. We do not account for this behavior in our simple recalibration procedure, which leads to an overcorrection of the data.

Nevertheless, our experiment confirms the theoretical proposal of STIRAP-based localization and its analytic treatment (1.11). Under our experimental conditions with still very large beam diameters and small Rabi frequencies, STIRAP reaches a localization of at least $\Delta r \approx 3\,\mu\text{m}$, i.e., very much below the pump beam diameter. Extrapolating from these results, already for still moderate focusing to a donut size of $w_P = 15\,\mu\text{m}$, yielding (at the same pump pulse energy as in our present experiment) a pump Rabi frequency of $\Omega_{P0} = 2\pi \times 18\,\text{MHz}$, we would confine the

population to $\Delta r \leq 100\,\mathrm{nm}$, i.e., well below the diffraction limit. Alternatively, we could reach the same confinement by keeping the Rabi frequency the same as in the present experiments (i.e., $\Omega_{P0} \approx 2\pi \times 3\,\mathrm{MHz}$) and focusing the pump beam to a still readily achievable waist of $w_P = 3\,\mu\mathrm{m}$.

1.4.2 Comparison with Localizing Population by EIT

We proceed now to localization by EIT in order to compare the results with STIRAP-driven localization. We keep all experimental parameters as in the STIRAP measurements, except for the temporal shape of the Stokes pulse. The latter now consists of a Gaussian rising and falling edge with a rise/fall time of 25 µs (FWHM), and a plateau of constant intensity with a duration of 30 µs in between. We choose the pulse delay such that the falling edges of Stokes and pump coincide, as required for EIT-driven localization [26].

The top row of Figure 1.12 shows the experimentally measured population distributions after the EIT process for selected values of R. The bottom row shows cuts (indicated by blue lines) through the central peaks. Clearly, population is localized in the center of the pump beam, with an extension well below the beam diameter. However, comparison to STIRAP (see Figure 1.10) very obviously shows the superior performance of STIRAP. For all values of R, STIRAP yields

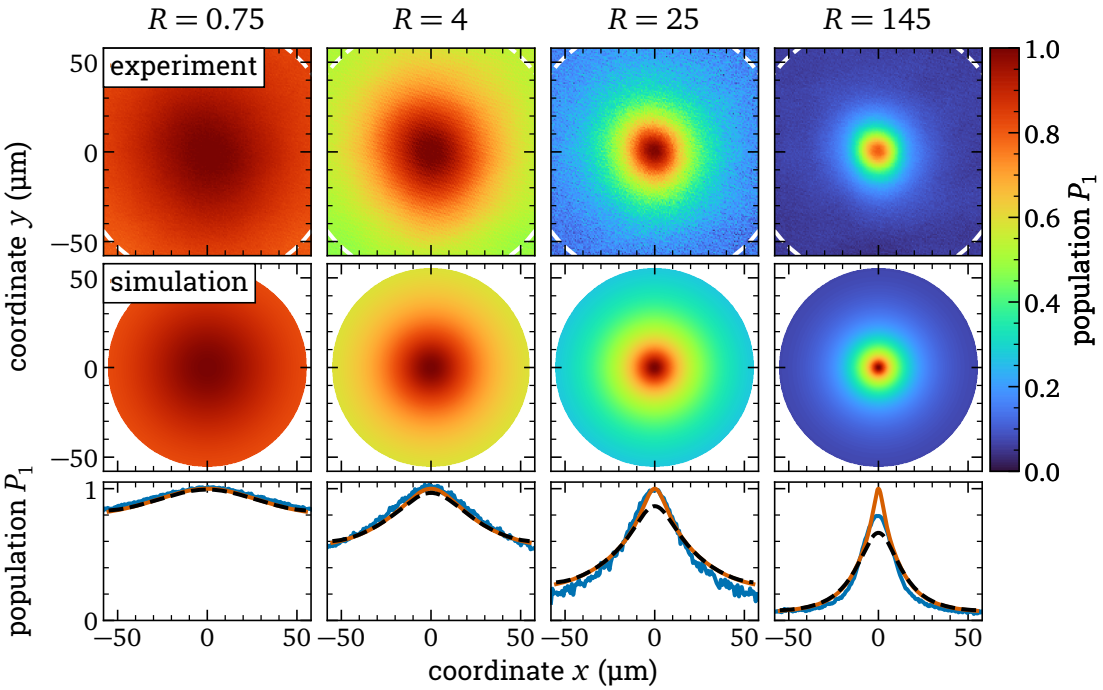

Figure 1.12: EIT-driven localization in Pr:YSO. Variation of the population $P_1(x, y)$ vs. coordinates x and y across the laser beam profiles. (upper row) Experimental data for different values of R. The white, dashed line indicates the diameter of the pump beam defined by the position of the ring at maximal pump intensity. (middle row) Numerical simulations with the experimentally determined parameters. (lower row) Cuts through the experimental data (blue line), simulation (orange line), and spatially filtered simulation (black, dashed line).

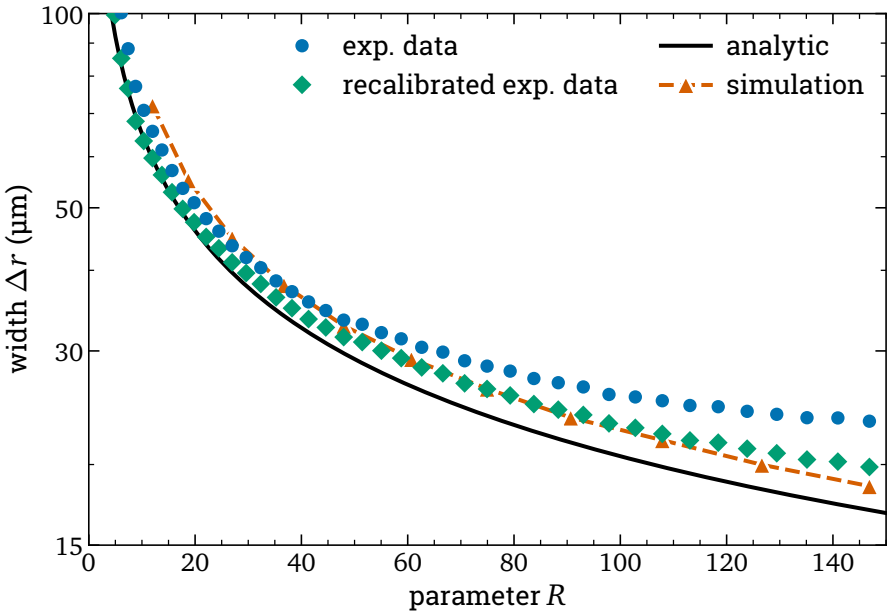

Figure 1.13: Width Δr (FWHM) of the population distribution $P_1(x, y)$ after localization by EIT vs. R. Comparison of the width calculated from Equation (1.6) (black line), numerical simulation (orange triangles), experimental data (blue circles), and recalibrated experimental data taking limited imaging resolution into account (green squares). Note the different scale of the vertical axis compared to Figure 1.11.

a much tighter localization than EIT. Furthermore, we see that STIRAP reaches full transfer efficiency in the outer parts of the pump profile already at $R = 4$, while for EIT even at the largest value $R = 145$, roughly 10 % of the population remains in state $|1\rangle$. This strongly reduces the fidelity of EIT-driven localization. Hence, STIRAP clearly outperforms EIT, as predicted by theory [15, 16, 19]. The numerical simulation (see middle row of Figure 1.12 and the corresponding cuts in the graphs of the bottom row) fully confirms our findings and conclusion.

Let us finally consider the convergence of EIT to stronger confinement of population with increasing values of R. In Figure 1.13 we plot the width Δr (FWHM) of the region with localized population, determined from fits to the experimental data (blue circles), numerical simulation (orange triangles), and analytic treatment (1.6) (black line) vs. the ratio R. We also apply the recalibration method, as presented for STIRAP, to the experimental EIT data to get information on the true width of the spatially confined population (see green squares). Note that due to the larger population regions in EIT-based localization, the limited resolution of the imaging setup and thus the recalibration have a much smaller effect compared to the STIRAP data. We find excellent agreement, in particular for the recalibrated data points compared to the simulation. The slight, systematic deviation compared to the analytic treatment is due to inhomogeneous broadening, which we neglected in the analytic solution. For EIT we find the strongest localization at $\Delta r \approx 20\,\mu\text{m}$, i.e., a factor of 6.5 larger compared to STIRAP, at equal experimental parameters. From theory, we calculate that EIT would require more than 25 times larger pulse energy to match with STIRAP. Again, this reveals the superior performance of STIRAP-driven localization compared to EIT.

1.5 Conclusion and Outlook

We experimentally demonstrated localization of atomic population by STIRAP and EIT in Pr:YSO. To the best of our knowledge, this represents the first implementation of EIT-driven localization in a solid medium and the first implementation of the STIRAP-based approach at all. We applied a STED-like geometry with a Gaussian-shaped Stokes and a donut-shaped pump beam to confine population by STIRAP or EIT in the zero-intensity center of the pump beam profile. We determined the obtained population distribution across the laser beam profiles by spatially resolved absorption spectroscopy with a probe laser. In particular, our experiments confirmed that adiabatic passage confines atomic population to spatial extensions well below the diameter of the driving laser beams. If we apply a pump beam with a beam waist of $w_P = 100\,\mu\text{m}$ and peak Rabi frequencies of $\Omega_{P0} = 2\pi \times 2710\,\text{kHz}$, we get a spatial confinement of population to $\Delta r \approx 3\,\mu\text{m}$ for STIRAP and $\Delta r \approx 20\,\mu\text{m}$ for EIT. We confirmed that the localization improves with increasing laser intensity. Moreover, our data demonstrated that STIRAP converges to smaller population regions much faster compared to EIT when increasing the laser intensity. The latter would require more than an order of magnitude larger laser pulse energy to match the performance of STIRAP. Hence, STIRAP-driven localization clearly outperforms EIT, as predicted by theory [15, 16, 19]. The experimental data agree with numerical simulations and the analytic treatment [19]. Residual deviations are due to slight parameter mismatches but mostly due to the limited resolution of our imaging setup.

We note that under our experimental conditions and due to the resolution limit of our imaging system, we still operated well above the diffraction limit. Nevertheless, the experiment permits extrapolation toward obtaining localized population in the subdiffraction regime. With still moderate beam diameters and Rabi frequencies, spatial confinement of population toward extensions $\leq 100\,\text{nm}$ in Pr:YSO is easily within reach. The results serve as a first step toward new applications of STIRAP, to prepare population patterns or confine population in a medium at large spatial resolution. This will be relevant to quantum information technology and well beyond.

The results of this chapter on STIRAP-based localization are the subject of a publication in the Journal of Physics B [51].

Prospects for Future Work The obvious next step is to decrease the beam diameters and implement adiabatic confinement below the diffraction limit. In this case, any standard imaging system will, of course, no longer be able to resolve and detect the subwavelength localization. While one could in principle still use the recalibration method introduced in this work, we suspect that the washed-out signal would become too faint for it to work properly.

Instead, we suggest utilizing an autocorrelation measurement similar to the one employed by Miles and coworkers for EIT-based localization in cold gases [54]. The general idea is to repeat the localization pulses but slightly shift the pump beam profile in between such that population only remains in state $|1\rangle$ as long as the pump displacement is smaller than the width of the localization region. We

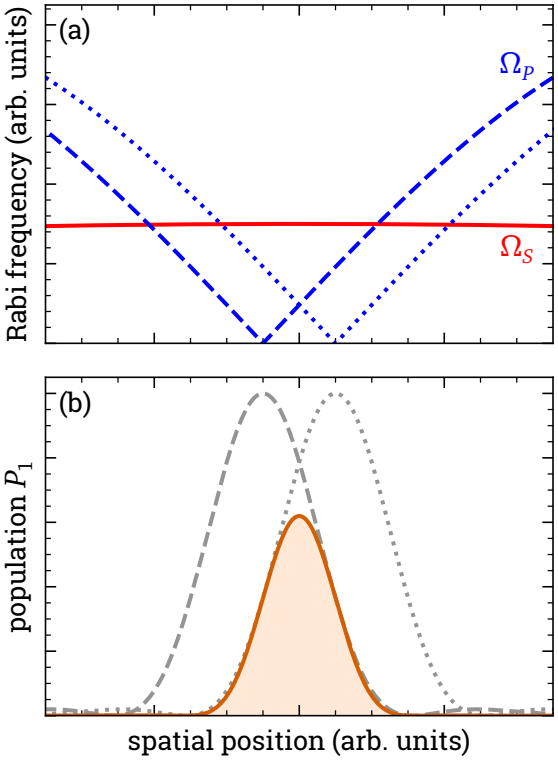

Figure 1.14: Principle of the STIRAP autocorrelation measurement: (a) Rabi frequency of Stokes (red) and pump (blue) pulses vs. spatial position. We shift the pump profile between the two sets of STIRAP pulses (compare blue, dashed and blue, dotted line). (b) Population P_1 remaining in state $|1\rangle$ after localization. The gray, dashed line depicts population localized by the first STIRAP process. The gray, dotted line shows where the second STIRAP process is spatially focused. Overall, population remains only in the overlap of both regions (orange line).

illustrate this concept in Figure 1.14. The first STIRAP process confines population to the gray, dashed region in Figure 1.14(b). Shifting the pump beam profile (compare the blue lines in Figure 1.14(a)) shifts the spatial focus of the second STIRAP process as well. Overall, population remains only in the overlap region of both processes, as indicated by the orange line in Figure 1.14(b). Thus, the total remaining population as a function of the pump displacement is essentially the convolution of the localization profile with itself and hence contains all the necessary information to calculate the latter's width. One can measure this population independent of the imaging system resolution, either by absorption spectroscopy as before or with a fluorescence-based measurement if necessary.

As an alternative approach to measuring the width of the localized population at subwavelength scale, we suggest applying a magnetic (or electric) field gradient that induces position-dependent level shifts. This translates the information about the spatial population distribution into a spectrum that is easy to measure. However, estimations show that the required gradient is on the order of 0.2 T/mm, i.e., very large and challenging to implement experimentally.

Finally, in the long run, one should actually combine the subwavelength localization with a quantum memory protocol to increase the latter's storage capacity. This requires the preparation of a pattern of localized population peaks in space, which is laborious to implement with the donut-shaped pump profile we used in the present experiments. Instead, a standing wave geometry, as is often used in subwavelength localization [34, 53, 54] would be better suited to create the required population pattern.

Chapter 2

Confining Atomic Excitations in Space via Narrowband Composite Pulse Sequences

2.1 Introduction

In this chapter, we present our results on localization by NCP sequences. We are currently preparing a manuscript to publish these results.

CP sequences [42–44] in general have been a versatile tool for decades, but are best known in nuclear magnetic resonance (NMR) spectroscopy [42, 43]. More recently, they have, e.g., also been applied to quantum information processing (see also Chapter 3) [44, 48, 70].

NCP sequences in particular have long been proposed and implemented to, e.g., increase the resolution of NMR spectroscopy [71–73]. For the specific application of high-resolution qubit addressing, i.e., subwavelength localization, they were first suggested more recently by Ivanov and Vitanov [20]. Later, Merrill and coworkers implemented them to reduce the ion spacing of a surface trap by about 40 % [22]. However, since then, newer classes of NCP sequences that promise better confinement have been developed [74]. These have yet to be implemented experimentally. Furthermore, there are no implementations for localizing excitation by NCP sequences in a solid yet. In particular, there are no implementations in inhomogeneously broadened media. These impose additional requirements on the NCP sequences and render many of the previously known sequences inapplicable.

In comparison to the STIRAP-driven localization presented in the previous chapter, NCP sequences provide several advantages, especially regarding applications in quantum computing: Unlike STIRAP, they do not necessarily require the qubit to be in a specific initial state [42, 75, 76], and they need only a two-level system and a single laser beam. The latter makes them easier to implement experimentally than STIRAP, but also inapplicable for metastable target states. However, they can be extended to multi-level systems as well [77–79]. Moreover, they can be used not only to localize excitation but to implement arbitrary narrowband qubit rotations, i.e., localized single- [22, 76, 80] and multi-qubit gates [81].

In this chapter, we present a thorough, systematic study of localizing excitation by NCP sequences in a rare-earth ion-doped crystal. We implement a new class of sequences developed by our cooperation partner Nikolay V. Vitanov (University of Sofia) specifically for inhomogeneously broadened media and compare it to other previously published sequences [20, 21, 74] as well as a numerical simulation. This proof-of-principle experiment operates above the diffraction limit but still fully confirms the theoretical predictions, thus paving the way for further investigations toward high-resolution addressing.

2.2 Basic Theory

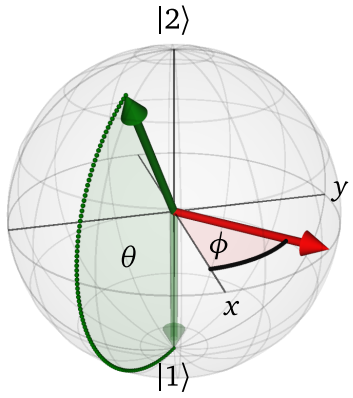

Figure 2.1: Bloch sphere representation of a two-level system. A laser pulse with phase ϕ (red arrow) rotates the Bloch vector (green arrows) by θ.

We now briefly review the basic theory of localized excitations driven by NCP sequences in a two-level system coupled to a single laser beam. We consider this system in the Bloch sphere picture (see Figure 2.1) where we represent interaction with a laser pulse as a rotation of the Bloch vector (green arrows) around a torque vector (red arrow). In the resonant case, the latter lies in the x-y plane, and its angle ϕ to the x-axis is simply the phase of the laser pulse. The rotation angle θ is equal to the pulse area A defined by

$$A = \int \Omega(t)\,\mathrm{d}t \tag{2.1}$$

with the Rabi frequency $\Omega(t)$. For pulsed excitation with the peak Rabi frequency Ω_0 and the duration τ, we have $A \propto \Omega_0 \cdot \tau$. Assuming population initially in the ground state $|1\rangle$, i.e., the Bloch vector pointing to the south pole, we get the excitation probability to state $|2\rangle$

$$P_2 = \sin^2(A/2). \tag{2.2}$$

Let us now assume a typical Gaussian laser profile with a peak pulse area of π, i.e., perfect population inversion in the center of the beam. Using Equation (2.2) we can calculate the spatial population distribution after the excitation as

$$P_2(\mathbf{r}) = \sin^2\left(\pi/2 \cdot e^{-r^2/w^2}\right) \tag{2.3}$$

with the radial coordinate r and the beam waist w. We find that the widths (FWHM) of the laser beam and population distribution are equal (see also Figure 2.3).

We can change this behavior, i.e., the dependence of the excitation probability on experimental parameters, by replacing the single pulse with a series of pulses with different phases. The latter act as control parameters that allow us to shape the excitation profile.[1] This is the general concept of CP sequences [42–44]. Depending on the application, we can derive CP sequences with any target rotation on the Bloch sphere. We can further make these sequences either more robust or more susceptible to changes in pulse parameters compared to a single pulse, resulting in broadband or narrowband sequences, respectively.

In this chapter, we focus our attention on sequences that show narrowband behavior regarding the pulse area when it changes from its target value π. We utilize only the phases ϕ_k of the pulses as control parameters and keep their peak

[1] We note that, in general, one can also use other pulse parameters like the detuning or pulse area as control parameters.

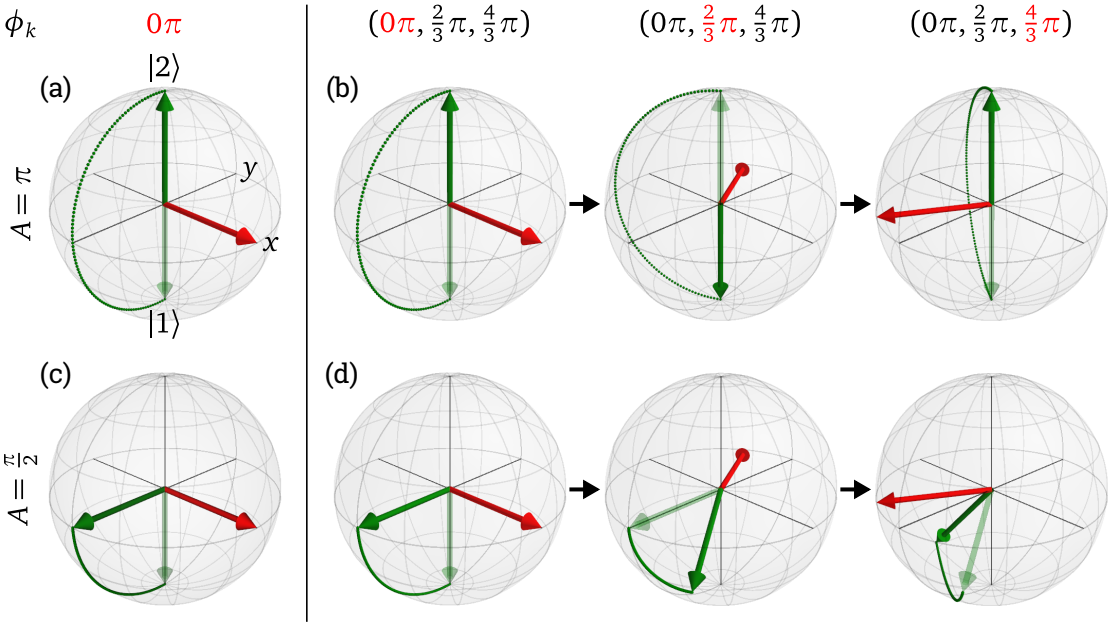

Figure 2.2: Bloch sphere representation of a two-level system excited by a single pulse (left) or the 3-pulse NCP sequence $(0\pi, \frac{2}{3}\pi, \frac{4}{3}\pi)$ [21] (right). Each Bloch sphere shows the evolution (green circles) of the Bloch vector from its initial state (transparent green arrow) to its final state (solid green arrow) during the interaction with a single pulse. The red arrows show the pulses' torque vectors; their phases are given in red at the top. The pulse area A of each individual pulse is π in (a) and (b) and $\pi/2$ in (c) and (d).

pulse area $A = \pi$ and detuning $\Delta = 0$ equal. We denote such a NCP sequence consisting of N pulses as $(\phi_1, \phi_2, \ldots, \phi_N)$.

In Figure 2.2, we illustrate the effect of a NCP sequence with a simple example. Its intended behavior is to create full population inversion, i.e., $P_2 = 1$, for $A = \pi$ (in the center of the beam) while suppressing excitation for any other pulse area. For comparison, we depict in Figures 2.2(a) and 2.2(c) the interaction of a two-level system with a single pulse with the arbitrarily chosen phase $\phi_1 = 0$. Figure 2.2(a) shows excitation with the pulse area $A = \pi$ as in the center of a beam profile. We see full population inversion, i.e., $P_2 = 1$ in the final state where the Bloch vector points to the north pole. In Figure 2.2(c) we consider the pulse area $A = \pi/2$ and see that the Bloch vector is rotated into the equatorial plane, i.e., $P_2 = 0.5$. This is the behavior of a single pulse, which we discussed before.

Let us now consider the effect of the $N = 3$ pulse NCP sequence $(0\pi, \frac{2}{3}\pi, \frac{4}{3}\pi)$ [21] as depicted in Figures 2.2(b) and 2.2(d). The first pulse has a phase of $\phi_1 = 0$, and its effect is exactly the same as the single pulse that we discussed previously. In the case of $A = \pi$ (see Figure 2.2(b)), the second pulse simply rotates the Bloch vector back to the south pole, just around a different axis of rotation, and the third pulse rotates the Bloch vector back to the north pole, again with a different axis of rotation. The result is—as intended—the same as in the case of a single pulse: $P_2 = 1$. The interaction looks vastly different, however, for $A = \pi/2$ (see Figure 2.2(d)). Here, due to their phases, the second and third pulses rotate the Bloch vector to a final state below the equatorial plane, i.e., $P_2 < 0.5$. This is precisely the desired effect, i.e., the excitation for a pulse area $A \neq \pi$ is suppressed.

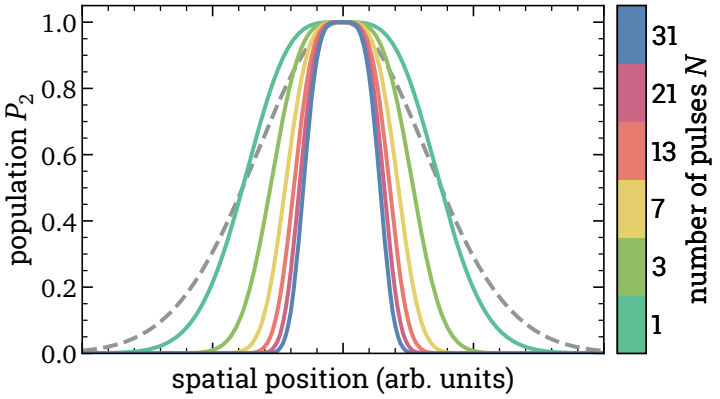

Figure 2.3: Simulated excitation by NCP sequences from [21] across a Gaussian laser profile. Variation of the population P_2 vs. spatial position for different numbers of pulses N (color code). The gray, dashed line shows the Gaussian Rabi frequency profile of the driving laser pulses. The pulse area in the center of the beam is $A = \pi$.

We can also see this in Figure 2.3, where we plot the simulated population transfer of NCP sequences with different numbers of pulses N across a Gaussian laser profile. For a single pulse, the excitation profile has the same width as the exciting beam, just as we have seen in Equation (2.3) (compare turquoise and gray, dashed lines). However, when we increase the number of pulses to $N = 3$, excitation in the wings of the beam profile (where $A < \pi$) is significantly suppressed while the transfer probability in the center remains at unity, as we have seen in the example above. Further increasing the number of pulses in the NCP sequence (and choosing appropriate phases) further improves the localization. This is due to the increasing number of control parameters (the phases of N pulses) that are available to optimize the sequence.

2.3 Experimental Setup

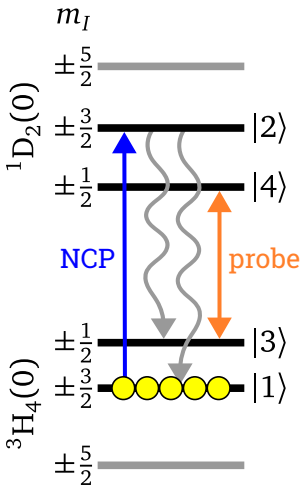

Figure 2.4: Coupling scheme for the NCP experiments in Pr:YSO. Straight lines depict transitions coupled by a laser; wavy lines show spontaneous decay. Yellow circles show the initial population.

As in the previous chapter (see Section 1.3.2), we also implement our experiments on localized excitations by NCP sequences in a Pr:YSO crystal among the hyperfine states of the $^3H_4(0) \leftrightarrow {}^1D_2(0)$ transition. Here, we choose the hyperfine states $|1\rangle = {}^3H_4(0)\,|m_I = \pm 3/2\rangle$ and $|2\rangle = {}^1D_2(0)\,|m_I = \pm 3/2\rangle$ to drive NCP sequences (see Figure 2.4) since the large transition moment enables high Rabi frequencies, i.e., short pulses. This is important because the coherence time of the optical transition $T_2^e = 111\,\mu s$ sets an upper limit for the duration of the NCP sequences.

After the NCP sequence, the localized population in state $|2\rangle$ decays with the lifetime $T_1^e = 164\,\mu s$ mostly into states $|1\rangle$ and $|3\rangle = {}^3H_4(0)\,|m_I = \pm 1/2\rangle$. Assuming that decay during the NCP sequence is negligible, the population distribution in state $|3\rangle$ after the decay is proportional to the population initially localized in $|2\rangle$. Hence, we can use absorption spectroscopy with a probe pulse on the

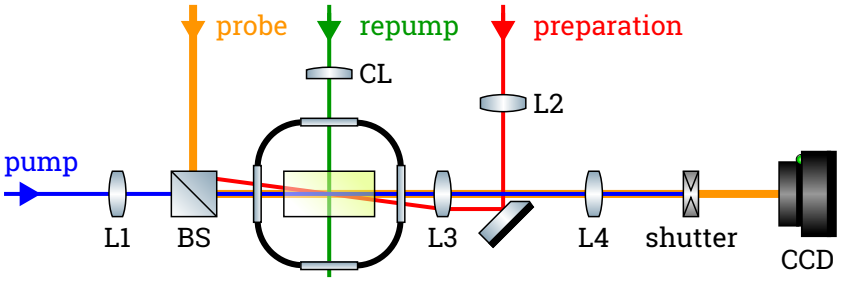

Figure 2.5: Experimental setup with pump (blue), preparation (red), repump (green), and probe (orange) beamlines, Pr:YSO crystal (green), beam splitter (BS), lenses (L), cylindrical lens (CL), and CCD camera.

$|3\rangle \leftrightarrow |4\rangle = {}^1\mathrm{D}_2(0)\,|m_I = \pm 1/2\rangle$ transition to measure this distribution (see Section 1.3.3 for details).

We note that even though the localized excitation lives only for a comparatively short time, we could still exploit the very long ground state lifetime $T_1^g = 100\,\mathrm{s}$ in Pr:YSO to create long-lived population patterns also with NCP sequences. To do so, one would simply have to coherently map the excited state population to state $|3\rangle$ with a single resonant π pulse (or a broadband CP sequence). However, for this first demonstration of localization by NCP sequences, we skip this additional step.

Figure 2.5 shows our experimental setup, which is in large parts identical to the STIRAP experiment depicted in Figure 1.7. We discuss here mainly the differences, and refer to Section 1.3.3 for further details. In this experiment, we derive all laser beams from an amplified and frequency doubled diode laser.[2] This system yields 800 mW of optical power at the experiment and is stabilized in frequency[3] to well below 100 kHz (FWHM). We can control each beamline in the experiment in intensity, frequency, and phase using acousto-optic modulators.[4] We employ direct digital synthesis drivers[5] to generate preparation, repump, and probe pulses and an arbitrary waveform generator[6] (AWG) to generate the NCP sequences. This setup gives us a phase accuracy better than $\pi/200$, while NCP sequences with a few 10 pulses require only about $\pi/100$ (as determined by numerical simulations).

As before, the pump beam (which drives the NCP sequences) passes a spatial filter to ensure a clean Gaussian beam profile before we mildly focus it into the crystal with lens L1 (focal length 200 mm), yielding a beam diameter (FWHM) of 210 µm. To determine the spatially varying population distribution after the NCP sequence, we measure the transmission across a probe laser beam profile, as described above. The probe beam copropagates with the pump beam, but is temporally well separated from the NCP sequences by roughly 7 ms. This delay is much longer than the lifetime of the excited state $T_1^e = 164\,\mu\mathrm{s}$, such that the

[2] DLC PR STORAGE, Toptica Photonics
[3] using FALC PRO, Toptica Photonics and a home-made high finesse cavity [67]
[4] pump: AOMO 380-125, Gooch & Housego; probe, preparation, and repump: BRI-TEF-80-50-.606, Brimrose
[5] probe: AODS 20160-1, Crystal Technology; Stokes: DDSPA-B8b23b-0, AA Opto-Electronic; repump: Model 409b, Novatech Instruments
[6] AWG5014, Tektronix

population localized in state $|2\rangle$ has fully decayed when we probe. The probe beam has a diameter (FWHM) of 550 µm in the crystal, i.e., much larger than the pump profile, to cover the full interaction region. We image the probe beam profile onto the CCD camera using the same simple imaging system consisting of lenses L3 and L4 as before.

In this setup, we use a 10 mm long Pr:YSO crystal (0.05 % dopant concentration) and two perpendicular beamlines (preparation and repump) for the preparation by optical pumping instead of a single beamline as before (see Figure 2.5). The preparation beam counterpropagates to the probe (and pump) beam with a small angle of about 2° in between. We collimate this beam with lenses L2 (focal length 75 mm) and L3 to a diameter (FWHM) of 600 µm, ensuring good overlap along the entire crystal. The repump beam, on the other hand, propagates perpendicular to the other beams, and we mildly focus it with a cylindrical lens (focal length 150 mm) to a size of 440 µm × 2700 µm (FWHM, width × height) in the crystal.

In the optical pumping sequence, we apply the preparation beam to create the spectral pit that contains the NCP and probe transitions but use the repump beam to prepare the antihole on the NCP transition. Hence, along the propagation axis of the probe and pump beams, the crystal becomes entirely transparent on the relevant transitions, except in the region where the preparation and repump beams overlap. Only in this region, population is prepared in state $|1\rangle$ and thus we effectively get a shorter crystal. Due to saturation during the optical pumping, the thickness of this region and hence the effective crystal length are about 1 mm. We could vary this value by changing the width of the repump beam, i.e., choosing a cylindrical lens with a different focal length.

Figure 2.6 summarizes the time sequence of our experiments: (i) Preparation pulse sequence using optical pumping with the preparation beam to provide full transparency at the NCP and probe transitions. (ii) Transmission measurement of a probe pulse as reference. (iii) Preparation of the antihole on the NCP transition only in the overlap region between preparation and repump beam by optical pumping with the latter. (iv) Removal of population from state $|3\rangle$. (v) NCP sequence to drive localized excitations. (vi) Transmission measurement of a probe pulse to determine population patterns generated by the NCP sequence. We repeat the sequence (i–vi) and average the resulting images to reduce noise.

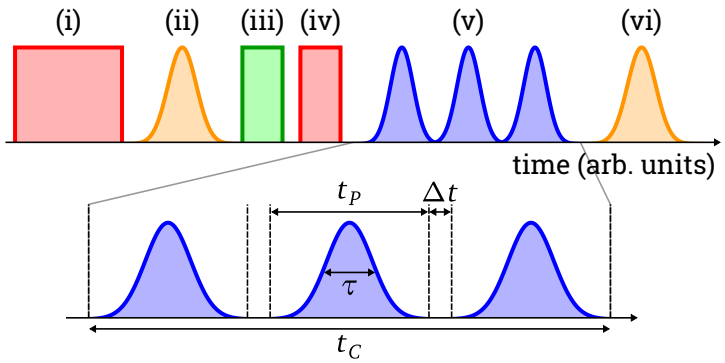

Figure 2.6: Time sequences (see main text) of optical pulses of the entire experimental sequence (top) and of an exemplary NCP sequence with $N = 3$ (bottom). Colors correspond to beamlines from Figure 2.5.

2.4 Experimental Results

We discuss now our experiments on localization driven by NCP sequences. We apply the time sequence discussed above and presented in Figure 2.6. In particular, we choose pump pulses with a peak Rabi frequency in space and time of $\Omega_0 = 2\pi \times 1\,\mathrm{MHz}$. With a Gaussian intensity profile in time with a duration (FWHM) of $\tau = 332\,\mathrm{ns}$, this corresponds to a pulse area of $A = \pi$ in the center of the beam profile. We truncate the pulses to a total pulse duration of $t_P = 1.2\,\mu\mathrm{s}$ such that the Rabi frequency in the temporal wings of the pulses reaches 0 and we get no adverse effects from a sharp cut-off. The pulses have a separation of $\Delta t = 40\,\mathrm{ns}$. We found that shorter separations Δt cause phase errors, presumably due to the limited rise time in the AWG or, more likely, the acousto-optic modulators.

The total duration of a sequence of N pulses is

$$t_C = N \cdot t_P + (N-1) \cdot \Delta t \approx N \cdot t_P = N \cdot 1.2\,\mu\mathrm{s}, \tag{2.4}$$

which is sufficiently shorter than the coherence time $T_2^e = 111\,\mu\mathrm{s}$ of the optical transition even for $N = 31$, i.e., the longest sequences we investigate. At the same time, the Rabi frequency is much smaller than the hyperfine splitting of the excited states ($\approx 4.5\,\mathrm{MHz}$) so we can neglect coupling to additional states, which would result in unwanted population transfer.

For systematic measurements, we keep the previously described parameters fixed and change only the number of pulses and their phases. For each NCP sequence, we measure the population P_3 with a probe pulse of Gaussian intensity profile in time with a duration (FWHM) of $10\,\mu\mathrm{s}$ and a peak Rabi frequency of roughly $2\pi \times 15\,\mathrm{kHz}$, which leads to only negligible change of the population distribution. We expose the CCD camera to radiation for $40\,\mu\mathrm{s}$, which ensures detection of the entire probe pulse.

2.4.1 Localizing Excitation by Optimized NCP Sequences

Over the course of this work, we found that most of the previously published NCP sequences are not well suited to an inhomogeneously broadened medium such as Pr:YSO, as we will discuss in detail in Section 2.4.3. Hence, we collaborated with the team of Nikolay V. Vitanov to develop new NCP sequences that are optimized for our medium (albeit at some less efficient localization, as we will see in Section 2.4.2). In the following, we call this class of sequences "optimized", and we list its parameters in Table A.5 of Appendix A.

We now present our results on localization with these sequences. The top row of Figure 2.7 shows the experimentally measured population distribution after localization by optimized NCP sequences with different numbers of pulses $N \leq 11$. The bottom row shows cuts (indicated by blue lines) through the central peaks. Note that we plot here the population P_3 in state $|3\rangle$. However, since the NCP sequences are much shorter than the lifetime of the excited state ($t_C \ll T_1^e$), decay during the NCP sequence is negligible. Hence, as discussed before, the population P_3 at the time of measurement is proportional to the population P_2 localized in state $|2\rangle$.

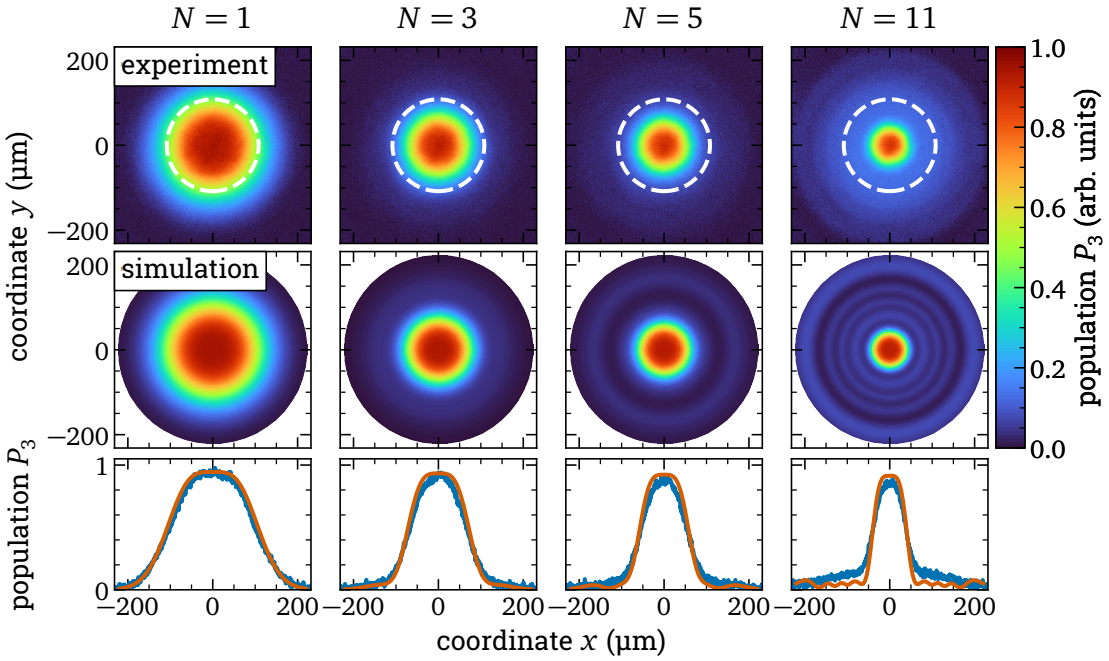

Figure 2.7: NCP-driven localization in Pr:YSO using optimized sequences. Variation of the population $P_3(x, y)$ vs. coordinates x and y across the pump beam profile. (upper row) Experimental data for different numbers of pulses of N. The white, dashed line indicates the diameter (FWHM) of the pump beam. (middle row) Numerical simulations with the experimentally determined parameters. (lower row) Cuts through the experimental data (blue line) and simulation (orange line).

We clearly see that already when switching from a single pulse to $N = 3$, the extension of the localized population shrinks significantly. Any population transfer that would be expected in the wings of what is essentially a 3π pulse is fully suppressed. The central population peak narrows even further when we increase the number of pulses beyond $N = 3$. For $N = 11$ pulses, the population is confined to a width of about 40 % of the single pulse excitation profile. This is already clear evidence for localization driven by NCP sequences. However, in particular for $N = 11$ pulses, the population transfer in the wings is no longer fully suppressed. Nevertheless, this background population remains well below 20 %.

We compare the results of our measurement to a straightforward numerical simulation based on a density matrix calculation of the three-level system $|1\rangle$, $|2\rangle$, and $|3\rangle$ in Pr:YSO, interacting with NCP pulses. The calculation takes decay of the excited state $|2\rangle$ as well as the decoherence and the inhomogeneous broadening of the optical transition $|1\rangle \leftrightarrow |2\rangle$ into account. In the calculation, we employ a Gaussian Rabi frequency distribution in space with its width matched to the experimental data, and set all other pulse parameters to be the same as in the experiment. The middle row of Figure 2.7 shows the results of the simulation. The orange lines in the bottom row indicate cuts through the central peak in the two-dimensional plots of the simulations. We see excellent agreement between experiment and simulation, with only some small differences in the peak shape and the wings of the profile. Compared to the simulation, the experimental data shows a sharper peak that decreases slightly in height with the number of pulses N.

This indicates that the central pulse area in the experiment is slightly smaller than π. We found that it is nearly impossible to set the pulse parameters more precisely than in the presented experiments, and will discuss some possible solutions at the end of this chapter. However, from further simulations, we can estimate that this pulse area error is at most 1 %.

Furthermore, we see some faint rings in the wings of the simulated data, especially for $N = 11$, that are also barely visible in the two-dimensional plots of the experimental data. These rings are caused by the inhomogeneous broadening of the optical transition, as we will discuss in Section 2.4.3. However, in the experimental data, the rings are mostly hidden below a broad background that the simulation does not reproduce. We suspect that this background is caused by additional, incoherent population transfer from state $|1\rangle$ to state $|3\rangle$. This could be either due to off-resonant excitation to state $|4\rangle$ or due to Raman scattering. We present additional studies of this background in Appendix B but have so far been unable to conclusively determine the underlying mechanism. We note, however, that neither this background nor the rings caused by inhomogeneous broadening are intrinsic to the NCP sequences but rather limitations of our specific medium.

We analyze the data now in more detail. To do so, we extract the width (FWHM) of the localized peak. For the simulated data, we can calculate the width directly, while we use a fit of the form

$$P_3(r) = \mathcal{A} \cdot \sin^2\left(\frac{\pi}{2} \cdot \exp\left(-4 \ln 2 \frac{r^2}{\Delta r^2}\right)\right) + \mathcal{B}, \tag{2.5}$$

i.e., the expected shape of the transition probability with a Gaussian laser profile (compare to Equation (2.3)), to find the width Δr (FWHM) of the experimental data. Figure 2.8 shows the (normalized) width of the experimental data (blue circles) and the simulation (orange triangles) vs. the number of pulses N for up to $N = 31$. Clearly, the peak width decreases with the number of pulses, as expected. We find excellent agreement up to about $N = 11$ pulses. For larger numbers of pulses, the experimentally determined profiles are slightly wider than the simulated profiles. This is most likely caused by a small deviation of the experimental beam profile from the ideal Gaussian assumed in the simulation. The narrowest measured population peak with $N = 29$ pulses has a width of only about 28 % of the population distribution after a single π pulse. This fully confirms the proposal of localization by NCP sequences with a confinement that is far below what was reported in previous experiments [22] due to the newer and optimized sequences.[7]

We further quantify the data by fitting it to the power function

$$\Delta r(N) = N^{-\alpha} \tag{2.6}$$

and obtain the exponents $\alpha = 0.38$ for the experimental data and $\alpha = 0.42$ for the

[7] Note that Merrill and coworkers characterize the localization from the ion separation at which the infidelity of a neighboring qubit reaches $\leq 10^{-4}$, while we use the spatial width (FWHM) of the excitation profile. When we apply the latter, we find a width of ≈ 72 % for their data [22].

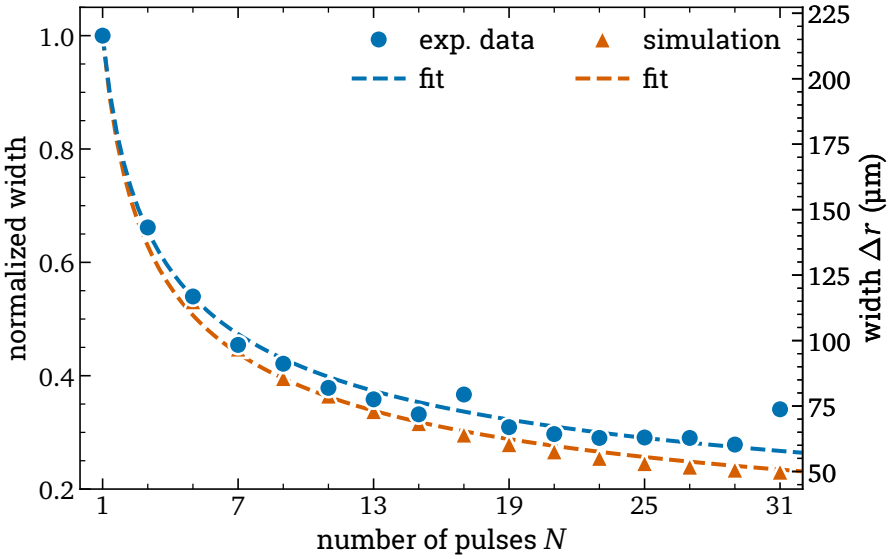

Figure 2.8: Width Δr (FWHM) of the population distribution $P_3(x, y)$ after localization by optimized NCP sequences vs. the number of pulses N. Comparison of the experimental data (blue circles) and numerical simulation (orange triangles). The dashed lines show fits to the power function (2.6).

numerical simulation. The fits (see dashed lines in Figure 2.8) match the data very well. As expected, we get slightly a larger exponent α for the simulation, i.e., a stronger confinement at the same number of pulses.

2.4.2 Comparison with Other NCP Sequences

We now continue to compare the previous results with four other classes of NCP sequences. All of these sequences were developed by the group of Nikolay V. Vitanov [20, 21, 74] and we list their parameters in Appendix A. Except for the phases of the pulses, all experimental parameters are the same as in the previous section.

We compare four of these classes in Figure 2.9 (the fifth class is almost identical to the "antisymmetric" class, and we skip it here for clarity).[8] The top row shows the experimentally determined population distribution for different sequences with $N = 13$ pulses each. The bottom row shows cuts (indicated by blue lines) through the central peak. Clearly, the excitation is localized in a central peak for all sequences, but the profiles look very different. Even though all NCP sequences consist of the same number of pulses, the width of the population peak differs strongly from sequence to sequence. We find the narrowest peak for the "antisymmetric" sequence, but the peak of the "optimized" sequence presented in the previous section is only slightly wider.

Furthermore, all but the "symmetric" and "optimized" sequences show pronounced rings around the localized center. The numerical simulation shown in the middle row and as cuts through the central peak in the bottom row (orange lines) of Figure 2.9 reproduces these very well. As we will discuss in more detail

[8] We discuss our naming scheme below.

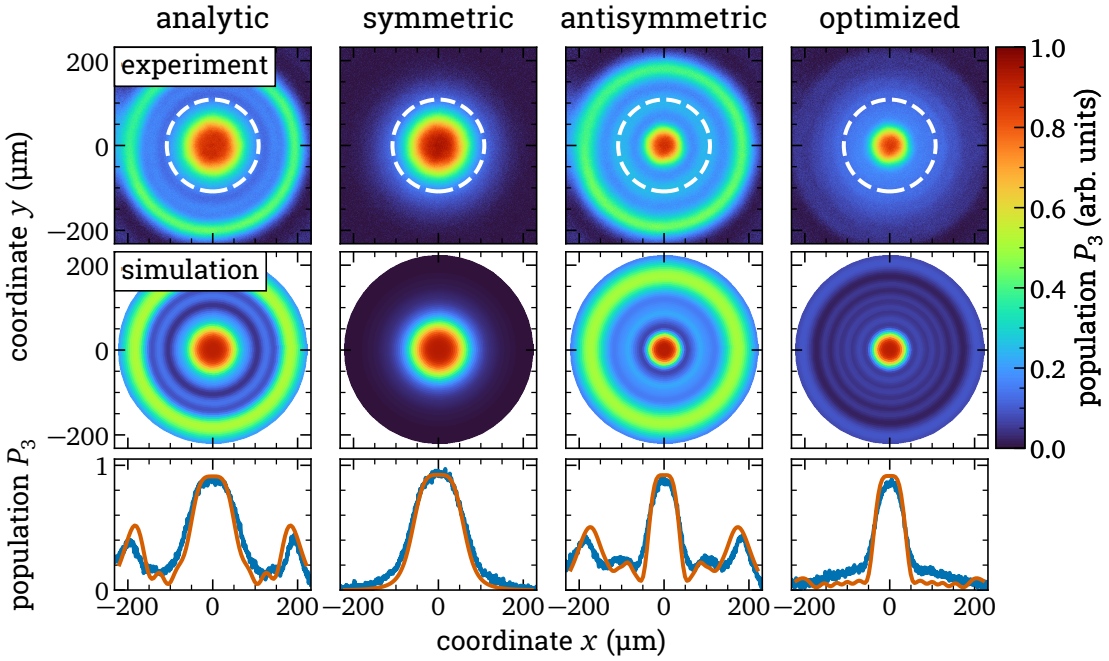

Figure 2.9: NCP-driven localization in Pr:YSO using different sequences with $N = 13$ pulses. Variation of the population $P_3(x, y)$ vs. coordinates x and y across the pump beam profile. (upper row) Experimental data. The white, dashed line indicates the diameter (FWHM) of the pump beam. (middle row) Numerical simulations with the experimentally determined parameters. (lower row) Cuts through the experimental data (blue line) and simulation (orange line).

in Section 2.4.3, these rings are caused by the inhomogeneous broadening of the optical transition. The mismatch in the ring amplitude between experimental data and simulation is most likely caused by an overestimated inhomogeneous broadening in the simulation. The slight difference in the ring diameter suggests that the tails of the beam profile are slightly longer than we assumed in the simulation, most likely due to an imperfect Gaussian profile in the experiment.

We perform systematic measurements and numerical simulations of all five classes of sequences that are summarized in Figure 2.10 where we plot the width of the localized excitation vs. the number of pulses N. Symbols represent experimental data, while lines of the same colors show the matching numerical simulations. The blue data is the same as shown in Figure 2.8, but we now show the simulation as a blue line instead of as orange triangles. In general, we see localization behavior for all classes of sequences, i.e., the width decreases with the number of pulses. For all classes, the experimental data and simulation agree very well for up to $N = 11$ pulses but deviate slightly for large pulse numbers. We attribute this difference to a deviation of the experimental beam profile from an exact Gaussian, as discussed before.

We quantify the localization performance by fitting the experimental data and the numerical simulations to the power function (2.6) and summarize the results in Table 2.1. For all sequences, the simulation shows slightly better performance, i.e., larger exponent α than the experimental data, as expected from the raw data (see Figure 2.10).

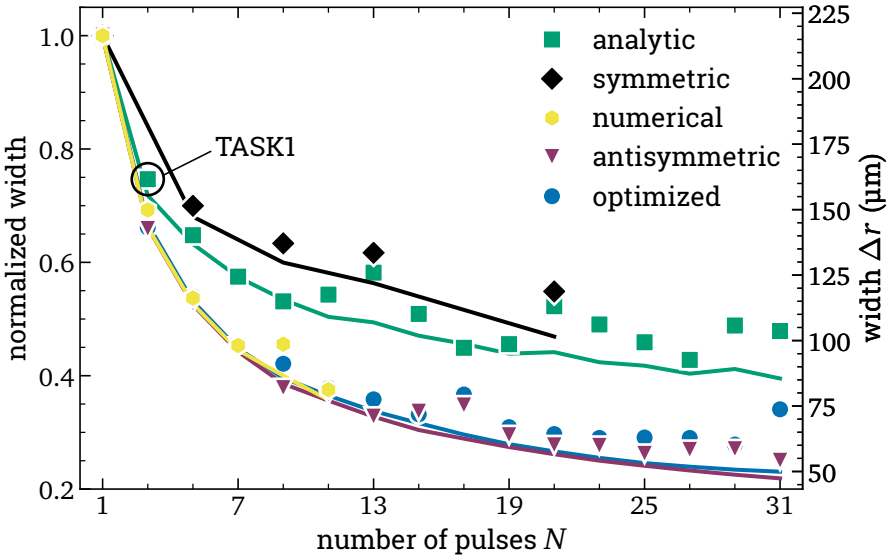

Figure 2.10: Width Δr (FWHM) of the population distribution $P_3(x, y)$ after localization by NCP sequences vs. the number of pulses N for various classes of sequences. Comparison of both experimental data (symbols) and corresponding numerical simulations (lines of the same colors). The analytic sequence with $N = 3$ is the same as the TASK1 sequence from [22]. The blue circles and line show the same data as Figure 2.8.

At the same time, there are also obvious differences between the different classes of sequences. Let us discuss these in more detail by going through the classes from top to bottom.

Analytic Sequences The first class of NCP sequences, named "analytic", was derived by calculating analytic expressions for the phases that optimize the propagator of the N pulse sequence [21]. We find that these sequences perform rather poorly compared to most other sequences. Not only do they show pronounced rings for more than $N = 5$ pulses (see Figure 2.9), but the width of the central peak also decreases slowly with the number of pulses compared to other sequences, as confirmed by the small exponent $\alpha = 0.25$. This is to be expected since the analytic sequences suppress excitation in the wings of the profile to less than 10^{-N} while the sequences with better confinement tolerate more excitation, i.e., they trade fidelity for a stronger confinement, as we will discuss below. Furthermore, we also see pronounced oscillations in the width of the experimental data vs. the number of pulses that the simulation does not reproduce. These are caused by fit errors due to the rings in the profiles. The advantage of these sequences is, however, that the analytic formula (see Equation (A.1) in Appendix A) allows the simple calculation of sequences with any arbitrary (odd) number of pulses.

We further note that the analytic sequence with $N = 3$ is (up to an irrelevant global phase of $\pi/3$) equivalent to the TASK1 sequence derived by Merrill and coworkers [22]. We find, with the same sequence, a slightly wider peak compared to their experiments (75 % of the beam profile diameter instead of 72 %) and attribute this small difference to the inhomogeneous broadening of our medium.

Table 2.1: Comparison of the power law exponent α from Equation (2.6) fitted to experimental data and numerical simulations of all investigated classes of NCP sequences.

sequence	excitation threshold ϵ	exponent α exp.	sim.
symmetric		0.20	0.24
analytic		0.25	0.28
numerical	0.01%	0.31	0.34
	0.1 %	0.33	0.37
	1 %	0.38	0.41
optimized		0.38	0.42
antisymmetric	1 %	0.41	0.43
	3 %	0.42	0.45
	10 %	0.44	0.48

Symmetric Sequences The derivation of the second class uses the same ansatz but numerical methods to find the phases, with the additional constraint that the sequences are symmetric with respect to reversal of the pulses [20]. Hence, we name this class "symmetric". With the smallest measured exponent $\alpha = 0.2$, these sequences perform similar but slightly worse than the analytic sequences. We assume that this is due to the numerical derivation, which performs worse than an exact analytic solution. However, they show no rings (see Figure 2.9) and are thus applicable in inhomogeneously broadened media.

Numerical and Antisymmetric Sequences The derivation of the third class, which we call "numerical", uses numerical optimization to reduce the transfer probability in the wings of the beam profile below a certain excitation threshold ϵ (here $\epsilon = 1\,\%$) [74]. While these sequences show rings (not shown in Figure 2.9), their localization performance with $\alpha = 0.38$ is clearly much better than the previous classes. As discussed above, this is due to the higher excitation tolerance of in the wings of the profile. However, the authors of [74] only provided sequences with up to $N = 11$ pulses.

Hence, we collaborated with Nikolay V. Vitanov to calculate additional sequences with more pulses. We term this class "antisymmetric" due to their additional constraint of being antisymmetric, i.e., invariant under simultaneous reversal of the pulses and change of the sign of their phases. As we can see in Figure 2.10, they match the performance of the numerical sequences and continue this trend up to $N = 31$ pulses. The exponent $\alpha = 0.41$ even shows that they perform slightly better. At $N = 31$ and with a confinement to 25 % of the width of the beam profile, they show the smallest localization we measured with any of the investigated sequences. However, they are affected by the inhomogeneous broadening and show pronounced rings (see Figure 2.9).

Furthermore, one can vary the performance of these two classes by changing the excitation threshold ϵ during the derivation. A higher threshold should improve the localization even further at the cost of more excitation in the wings.

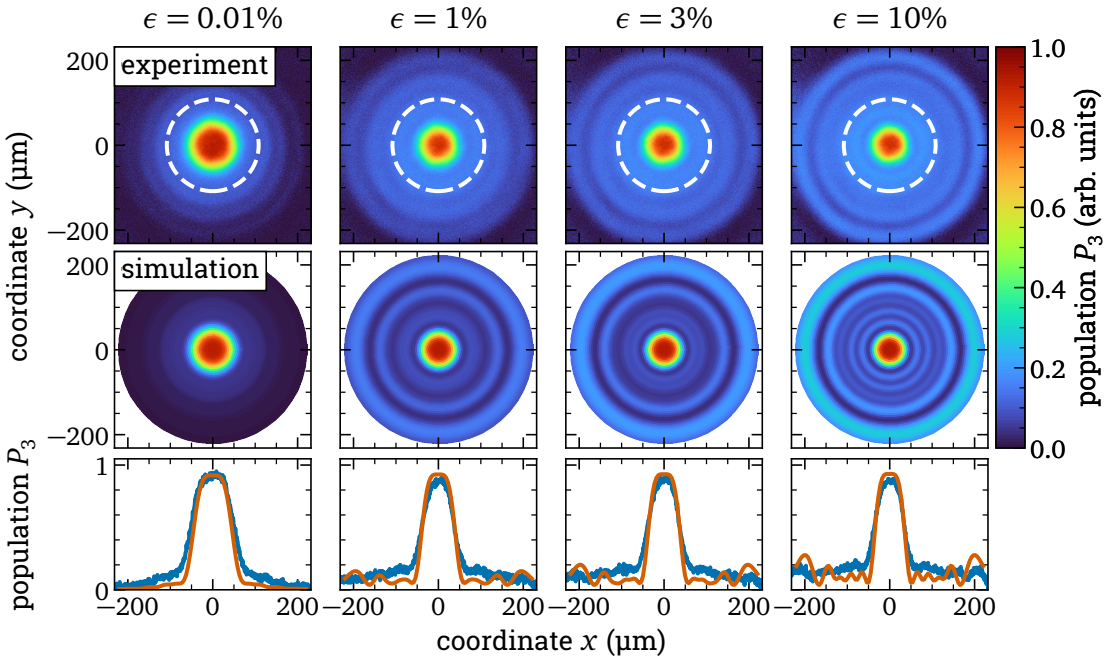

Figure 2.11: NCP-driven localization in Pr:YSO using sequences with different excitation thresholds ϵ but $N = 11$ pulses each. Variation of the population $P_3(x, y)$ vs. coordinates x and y across the pump beam profile. The left column shows a numerical sequence; the other columns show antisymmetric sequences. (upper row) Experimental data. The white, dashed line indicates the diameter (FWHM) of the pump beam. (middle row) Numerical simulations with the experimentally determined parameters. (lower row) Cuts through the experimental data (blue line) and simulation (orange line).

We investigate this behavior in Figure 2.11 where we compare the localization by four different NCP sequences with the same number of pulses ($N = 11$), but different excitation thresholds ϵ. We clearly see (in particular in the bottom row of Figure 2.11) that the excitation in the wings increases with ϵ, as expected. We note that the excitation should increase at most to the fraction ϵ of the peak excitation, but increases to about twice that value in the experimental data. This is partially due to the inhomogeneously broadened line, which causes rings in the excitation profile, and partially due to additional, incoherent population transfer (see Appendix B). Nevertheless, we also see that the width of the central peak in the profile narrows with the excitation threshold. The experimental data and the numerical simulation are in good agreement.

We perform systematic measurements and numerical simulations with both classes of sequences and three different thresholds ϵ each. We show the results in Figure 2.12 where we plot the width Δr (FWHM) of the confined population over the number of pulses N. As before, we find good agreement between experimental data and simulation up to about $N = 11$ pulses and a small deviation thereafter. Moreover, we clearly see that for higher excitation thresholds, the localization improves as expected. We also find larger exponents α for larger excitation thresholds (see Table 2.1). This fully confirms the expectation.

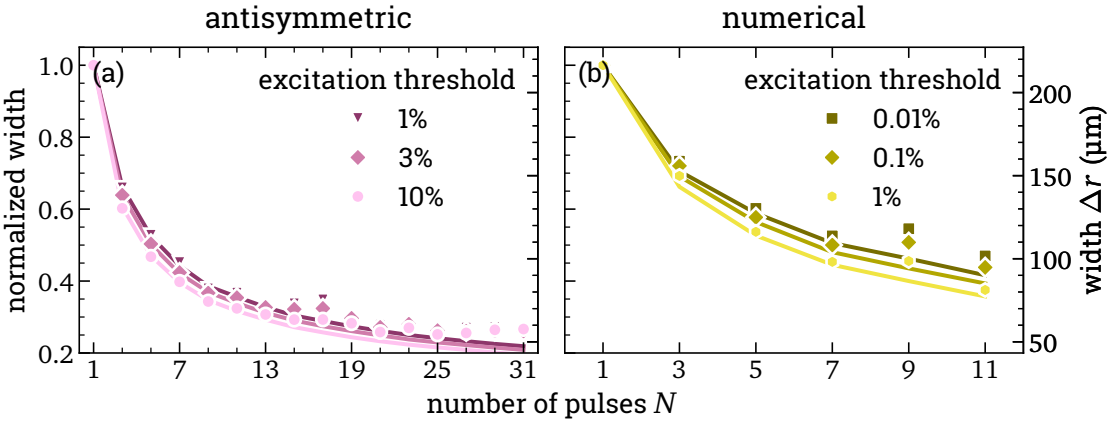

Figure 2.12: Width Δr (FWHM) of the population distribution $P_3(x, y)$ after localization by NCP sequences vs. the number of pulses N for antisymmetric (a) and numerical (b) sequences with different excitation thresholds ϵ. Comparison of both experimental data (symbols) and corresponding numerical simulations (lines of the same colors). Note the different ranges on the horizontal axes. The data with $\epsilon = 1\,\%$ is the same as the data shown in Figure 2.10.

Optimized Sequences For the final class of sequences, our theory partners derived sequences that show strong localization like the antisymmetric sequences but are at the same time not affected by inhomogeneous broadening, i.e., show no rings in the excitation profiles. To do so, they extended the methods employed for the derivation of the antisymmetric sequences such that the excitation probability also remains below the threshold $\epsilon = 1\,\%$ for detunings within the inhomogeneous line. We presented detailed results on these sequences in the previous section. They show almost no rings, even for $N = 31$ pulses. When comparing them to the antisymmetric sequences, we see that they perform slightly worse regarding the localization (compare blue circles and purple triangles in Figure 2.10). This is to be expected due to the additional constraints in their derivation. Nevertheless, unlike the antisymmetric sequences, they work in inhomogeneously broadened media and still reach a confinement to 28 % of the width of the beam profile.

2.4.3 NCP Sequences in an Inhomogeneously Broadened Medium

Let us now discuss the rings caused by inhomogeneous broadening and observed in the localization patterns of Figure 2.9 in more detail.

To understand the origin of these rings, we numerically simulate the population transfer of an $N = 11$ pulse analytic NCP sequence depending on the pulse area $A \propto \Omega \cdot \tau$ and the product of detuning and pulse duration $\Delta \cdot \tau$ for a peak Rabi frequency of $\Omega_0 = 2\pi \times 1\,\mathrm{MHz}$. All other parameters are as in the previous sections, but we neglect decay, decoherence, and inhomogeneous broadening. We plot this variation of the excitation probability with detuning and pulse area in Figure 2.13(a). If we consider the case of resonance $\Delta \cdot \tau = 0$, indicated by the white, vertical line, we see the expected result of a NCP sequence: For $A = \pi$, the transfer is complete, i.e., $P_2 = 1$, but for any pulse area smaller than about 0.65π population

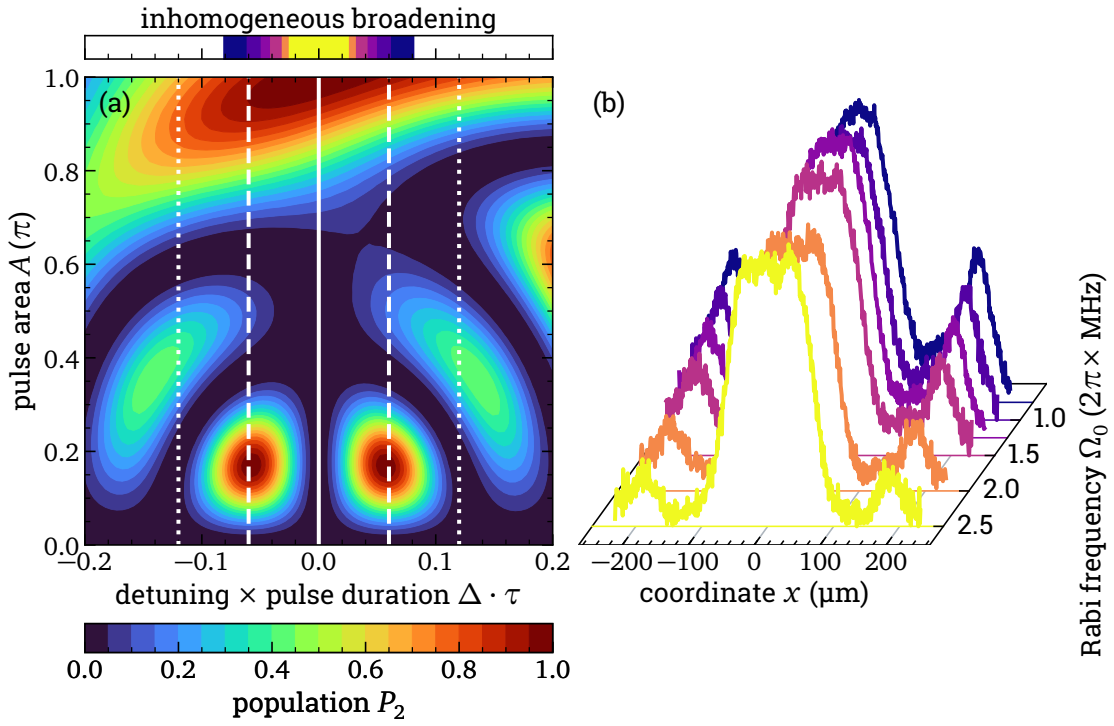

Figure 2.13: Investigation of the ring-like excitation patterns generated by NCP sequences in Pr:YSO. (a) Numerical simulation of the excitation probability vs. the product of detuning and pulse duration $\Delta \cdot \tau$ and the pulse area $A \propto \Omega \cdot \tau$ for the analytic sequence with $N = 11$ pulses. The peak Rabi frequency is $\Omega_0 = 2\pi \times 1\,\mathrm{MHz}$ and we neglect decay, decoherence, and inhomogeneous broadening. The white, dashed lines show the 100 kHz spectral linewidth (FWHM) of the inhomogeneous broadening in our system; the dotted lines show twice that width. The color scale at the top shows the width (FWHM) of the inhomogeneous broadening for different peak Rabi frequencies Ω_0, i.e., pulse durations τ. The color scale matches the data from (b). (b) Variation of the experimentally determined population $P_3(x)$ after localization with the $N = 11$ pulse analytic sequence vs. coordinate x for different peak Rabi frequencies Ω_0 (color scale).

transfer is fully suppressed. However, for $\Delta \cdot \tau \neq 0$ the shape of the population transfer is much more complex, with several regions of high population transfer even at small pulse areas. This is due to an additional phase accumulated by the detuned ions that disturbs the phase relation within the NCP sequence.

When we now consider inhomogeneous broadening, we have ions with detunings spread around resonance and thus average horizontally over this complex distribution. The dashed lines in Figure 2.13(a) indicate the inhomogeneous linewidth of 100 kHz (FWHM) in our experiment, while the dotted lines show twice the linewidth. This is approximately the area we average over, and it clearly contains regions of large population transfer. Hence, averaging leads to a pronounced ring far in the wings of the beam profile where the pulse area is roughly 0.15π and another faint ring at about 0.5π. This is what we see in Figure 2.9 (left column).

We can also see this in Figure 2.13(b) where we plot cuts through the experimentally determined population distribution after an $N = 11$ pulse analytic NCP sequence for different peak Rabi frequencies Ω_0 from $2\pi \times 0.75\,\mathrm{MHz}$ to

$2\pi \times 2.5\,\mathrm{MHz}$. Furthermore, the ring decreases in amplitude when the Rabi frequency increases. Again, we can explain this behavior using the distribution of the excitation probability in Figure 2.13(a). When we increase the Rabi frequency Ω of the pulses, we need to decrease their duration τ to keep the pulse area $A \propto \Omega \cdot \tau$ constant. Hence, the horizontal axis of the excitation plot essentially stretches outward, moving the regions of large population transfer further from resonance. Or, in a different picture, the width of the inhomogeneous broadening shrinks, as indicated by the color scale at the top of Figure 2.13(a) which displays the inhomogeneous linewidth (FWHM) for different peak Rabi frequencies. The larger the Rabi frequency, the narrower the inhomogeneous broadening, and thus a smaller fraction of the regions with large population transfer is included in the averaging. Consequently, the rings decrease in amplitude.

Hence, in inhomogeneously broadened media, it is beneficial to increase the Rabi frequency as much as possible. However, there is a trade-off since a higher Rabi frequency can increase incoherent population transfer, as discussed in Appendix B. Furthermore, since we have access to the optimized sequences that do not show regions of large population transfer within the inhomogeneous linewidth, we chose a rather small peak Rabi frequency of $\Omega_0 = 2\pi \times 1\,\mathrm{MHz}$ for the previous experiments.

We also note that it is actually the total duration of the sequence that matters and not the duration of an individual pulse, since the detuned ensembles accumulate the additional phase over that entire duration. Hence, increasing the Rabi frequency is only beneficial as long as the pulse separation remains constant such that the entire sequence duration decreases. This is usually the case.

2.4.4 Ring-Shaped Localized Excitation Patterns

In the previous sections, we presented convincing experimental data that show the capability of NCP sequences to spatially confine excitation. However, we also saw that even for the best class of sequences, this confinement improves rather slowly with the number of pulses, i.e., the best confinement we reached was 25 % of the beam diameter with $N = 31$ pulses. From the power function (2.6) we can extract that reaching a confinement to 2 % of the beam diameter as we have with STIRAP-based localization would require about 10 000 pulses. This is not only very difficult to implement in real experimental conditions with inevitable pulse errors and limited coherence time, but also a huge and maybe impossible effort in the numerical derivation of the NCP sequences. However, as we will see in the following, the localization is partially limited by the flat shape in the center of the Gaussian beam profile, where the pulse area varies slowly with the radial coordinate. Hence, an improved suppression at pulse areas close to π has only a small benefit regarding the localization.

In this section, we investigate how to omit the issue by localizing the population on a ring in the wings of the beam profile, where the Rabi frequency decreases (approximately) linear with the radial coordinate and not quadratically as in the center. We apply pulses with a pulse area of 2π in the center of the beam. Since the NCP sequences suppress excitation for any pulse area besides π, we expect a ring-shaped excitation pattern in space. The width of this ring should shrink

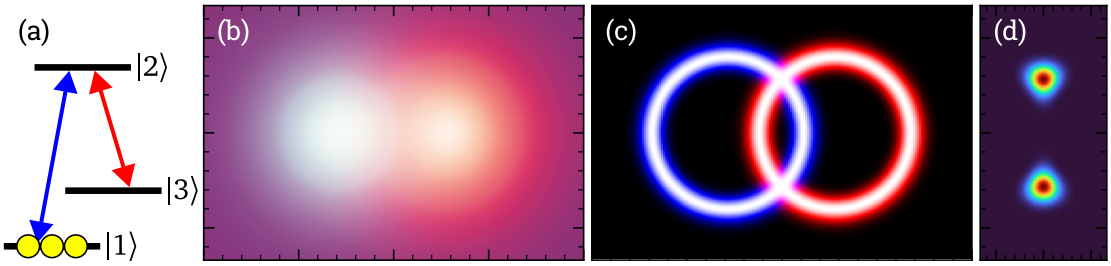

Figure 2.14: Spatial confinement using two time-separated NCP sequences on different transitions in a three-level system. (a) Λ-type coupling scheme. Yellow circles indicate the initial population. (b) Spatial distribution of the two shifted Gaussian Rabi frequency profiles with a central pulse area of $A = 2\pi$. (c) Spatial variation of the excitation probability of the two individual NCP sequences. We assume analytic NCP sequences with $N = 31$. (d) Spatial distribution of the population P_3 in state $|3\rangle$ after both NCP sequences.

quadratically faster with the number of pulses compared to the peak width, i.e., the exponent α in Equation (2.6) should be doubled.

We note that confining excitation to a ring is obviously of limited use for real applications. However, one can still generate a spot of tightly confined excitation using this method. Here, one would apply NCP sequences (with a central pulse area of 2π) on both transitions of a Λ-type system but with spatially shifted laser profiles as illustrated in Figures 2.14(a) and 2.14(b). The first NCP sequence excites population only on a ring, and hence the second NCP sequence transfers population to the final metastable ground state only where the two rings overlap (see Figures 2.14(c) and 2.14(d)). While not perfectly symmetric, the size of this region would not be limited by the flat shape of the Gaussian beam profiles.

To confirm this general behavior, we apply the ring-type localization in a two-level system. We use the class of optimized NCP sequences with a peak Rabi frequency of $\Omega_0 = 2\pi \times 2.5\,\mathrm{MHz}$. With a temporal pulse width (FWHM) of $\tau = 266\,\mathrm{ns}$ and a total pulse duration $t_P = 1\,\mu\mathrm{s}$ this corresponds to a pulse area of 2π in the center of the beam profile.

We show the results of these measurements for different numbers of pulses $N \leq 11$ in the top row of Figure 2.15. The bottom row shows cuts through the experimental data (blue lines). We clearly see the expected ring shape in the population distribution. The width of the ring decreases with increasing pulse number. However, as before, we also see a substantial background, especially for $N = 11$ pulses, that is most likely caused by incoherent transfer directly from state $|1\rangle$ to state $|3\rangle$ (see Appendix B). Furthermore, the amplitude of the ring decreases to about 60 % at $N = 11$ pulses. As with the data on localization driven by STIRAP, this is caused by the limited resolution of our imaging system when the ring width approaches 10 µm.

As before, we compare the experimental data with a numerical simulation shown in the middle row of Figure 2.15. The bottom row shows cuts through the simulation (orange lines). We find good qualitative agreement between experiment and simulation. However, the simulated ring is wider in particular for small numbers of pulses. This indicates a mismatch in the beam profile of experiment and simulation, i.e., that the Rabi frequency slope in the experiment

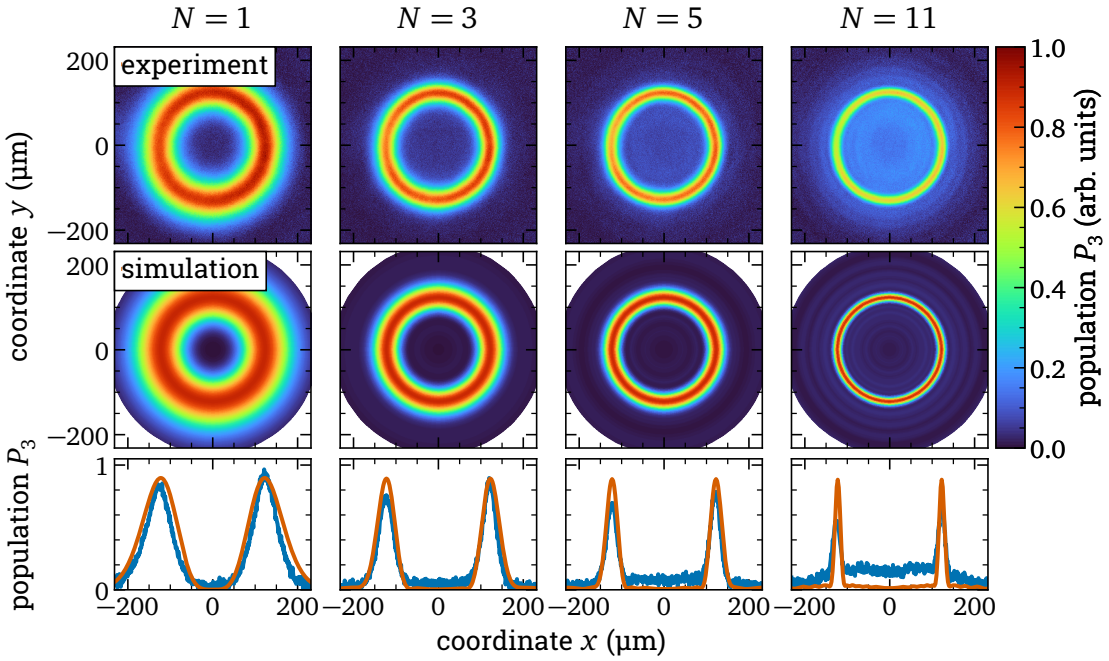

Figure 2.15: NCP-driven ring localization in Pr:YSO using the optimized sequences. Variation of the population $P_3(x, y)$ vs. coordinates x and y across the pump beam profile. (upper row) Experimental data for different numbers of pulses of N. (middle row) Numerical simulations with the experimentally determined parameters. (lower row) Cuts through the experimental data (blue line) and simulation (orange line).

is steeper than expected. This matches the deviation between experiment and simulation observed in the previous sections.

We further analyze the data by determining the width of the ring for both experimental data and numerical simulation (employing a fit to Equation (B.1) for the former) and plotting it vs. the number of pulses for up to $N = 31$ in Figure 2.16. The blue circles represent the experimental data, the orange triangles show the numerical simulation. As expected, we see a big discrepancy: At about $N = 9$ pulses, the measured width of the ring approaches 10 µm and remains at that level up to $N = 31$ pulses. In this region, the resolution of the imaging setup, which we determined to be 10 µm in an independent measurement (see Section 1.3.3), limits the experimentally determined width. The real population distribution is more narrow, it simply washes out due to the resolution limit and as such, the measured height of the ring also decreases as discussed above. However, we can still gain insight into the real width of the population distribution by applying the recalibration method introduced in Section 1.4.1. We show the recalibrated data as green squares in Figure 2.16. They match the numerical simulation very well. We assume that the remaining discrepancy is due to background population that we neglected in the recalibration. Hence, depending on the relative background levels, we may have over- or under-corrected some data.

From fits to the power law in Equation (2.6) we extract the exponents $\alpha = 0.72$ for the recalibrated experimental data and $\alpha = 0.75$ for the simulation. These are in good agreement.

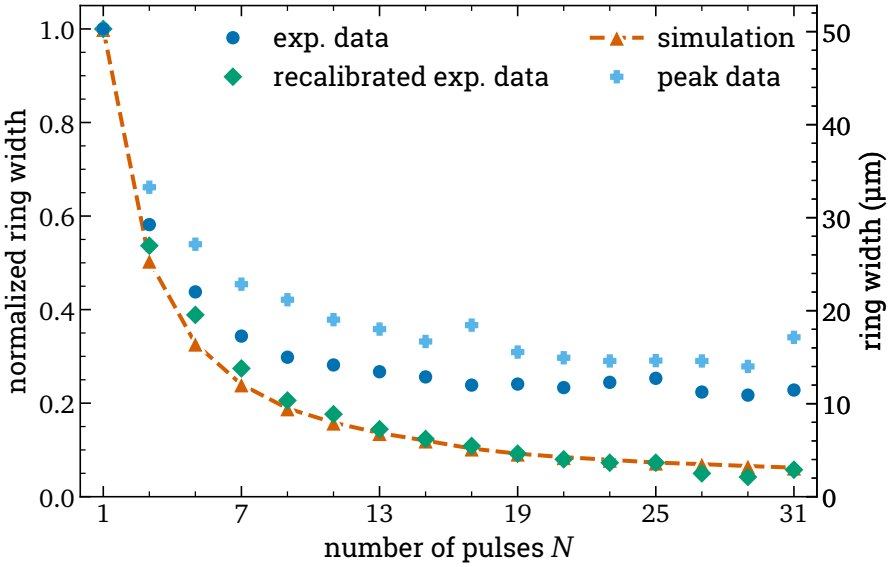

Figure 2.16: Width (FWHM) of the population ring $P_3(x, y)$ after localization by the optimized NCP sequences vs. the number of pulses N. Comparison of the numerical simulation (orange triangles), experimental data (blue circles), and recalibrated experimental data taking limited imaging resolution into account (green squares). The blue crosses show the normalized width (FWHM) of the population after peak-type localization by the same sequences. This is the same data as in Figure 2.8. The right vertical axis is only valid for the ring data.

Finally, we compare the data to the peak-type localization we discussed in Section 2.4.1. We expect a significantly better performance for the ring localization due to the steep Rabi frequency slope compared to the flat peak in the center of the beam profile. We plot the experimentally determined (normalized) width of the localization peak created with the optimized sequences in Figure 2.16 as blue crosses. As expected, the width of the ring decreases faster with the number of pulses than the peak width (compare green squares and blue crosses in Figure 2.16). The exponent $\alpha = 0.72$ of the ring data, which—as predicted above—is about twice the value of the exponent $\alpha = 0.38$ of the peak localization data, validates this conclusion. This confirms our assumption that the shape of the beam profile significantly limited the peak-type localization in the previous sections.

2.5 Conclusion and Outlook

We experimentally demonstrated localization of excitation by NCP sequences. To the best of our knowledge, this represents the first implementation of NCP sequences for localization in a solid. We applied sequences consisting of up to 31 pulses and confined the excitation to spatial extensions well below the diameter of the driving Gaussian laser profile. In particular, with a sequence consisting of 31 pulses, we got an excitation width of 25 % compared to the diameter of the driving laser beam, which is almost a factor of 3 smaller than in previous experiments [22]. We confirmed that the localization improves with the number of pulses. Moreover, our data demonstrated that some classes of sequences converge to

smaller localization much faster than others, as expected from theory [74]. The experimental data agree very well with numerical simulations. Residual deviations are due to a slight mismatch in the laser profile.

We found that the flat Gaussian shape in the center of the laser beam is one of the main limitations for localization by NCP sequences. Tighter localization is possible by localizing in, e.g., a ring on the slope of the laser profile instead.

Furthermore, we analyzed numerically and experimentally the influence of an inhomogeneously broadened transition on the localization by NCP sequences. We found that for most sequences, it leads to additional, unwanted population transfer in the wings of the laser profile. Hence, we collaborated with the team of Nikolay V. Vitanov to develop NCP sequences that are robust against inhomogeneous broadening and confirmed their behavior experimentally.

We note that under our experimental conditions, we still operated well above the diffraction limit. Nevertheless, the experimental data showed that NCP sequences can significantly relax the beam size requirements in high-resolution applications. The results serve as a step toward a new application of CP sequences to prepare excitation patterns or perform quantum gates with large spatial resolution. This will be relevant to quantum information technology and well beyond.

We are currently preparing a manuscript to publish the results of this chapter.

Prospects for Future Work We found in our experiments that the strong dependence of the transfer probability on the pulse parameters, which enables localization, is also an experimental challenge. Any pulse area deviation from the target value $A = \pi$ in the center of the beam profile results in a large loss of transfer fidelity due to the narrowband nature of the driving pulse sequences. Hence, a next step should be to also investigate passband sequences, as was suggested in the past [20, 74, 80]. These sequences are robust over a small range of parameters, but still suppress excitation for large deviations. Hence, they localize population (albeit not as strongly as NCP sequences), but at the same time they are robust to (small) pulse errors that are inevitably present in any experiment.

Furthermore, one could consider localization by NCP sequences in a Λ-type three-level system coupled by two laser beams, similar to the STIRAP setup. One could implement this by applying either independent and time separated NCP sequences on the two transitions, or directly with a NCP sequence on the Raman transition [77–79]. In either case, the localized population would benefit from the long ground state lifetime in Pr:YSO. One could further extend the first option by shifting the laser profiles with respect to each other and localizing in a ring each (see Figure 2.14). Then, the population in the final state would be localized only in the intersection of the two rings, which by the arguments in the previous section would be more narrow than the peak-type localization considered for most of this chapter. Localization on the Raman transition, on the other hand, would allow a direct application of localized interaction to Raman qubits.

Finally, we considered only localized population inversion in this work, but it is easily possible to derive similar NCP sequences for any arbitrary rotation on the Bloch sphere [22, 76, 80]. These would enable localized single-qubit gates, which are, of course, of great interest in quantum information technology.

Chapter 3

Dynamical Decoupling with Inhomogeneous Radio Frequency Fields

3.1 Introduction

In this final chapter, we consider a more typical application of CP sequences: To compensate for errors in the driving pulses. We present a showcase experiment where we intentionally introduce these errors in the form of inhomogeneous pulses and characterize the robustness of various state-of-the-art CP sequences.

In particular, we consider the context of quantum memories, where CP sequences are routinely applied—by our group [82, 83] and others [5, 84–86]—to increase the memory's storage time. Since the decoherence that limits the latter is often induced by environmental noise [47], decoupling the system from the environment is an effective approach to increase the coherence time. This technique, called DD [46–48], involves applying a sequence of control pulses for the decoupling and has been applied to many systems (see [48] and references therein). However, in standard DD sequences, inevitable pulse errors cause additional decoherence that often surpasses the environmental perturbation [48, 49]. Apart from reducing these pulse errors as much as possible in the first place, broadband CP sequences that compensate for the errors are a typical solution to this issue [42, 43, 48, 50]. There exists a wide variety of these robust sequences [48, 49, 83, 87, 88] that have been studied and compared extensively, both in theory and in experiments [48, 49, 83, 89–92].

However, regarding pulse errors, these studies are typically rather artificial in that they assume perfect pulses and then vary one or more pulse parameters. Yet, in a real experiment, it is usually inhomogeneity that introduces the pulse errors and not a fixed deviation that could be compensated by proper experimental calibration. For example, in rare-earth-based quantum memories, one typically drives DD with radio frequency (RF) fields [5, 82–85], where the presence of metal in close proximity to the RF coils causes eddy currents and thus often introduces field inhomogeneities, i.e., amplitude errors [93].

Hence, in this chapter, we present a simple showcase experiment where we intentionally introduce inhomogeneity in the RF fields. We generate a coherence in a rare-earth ion-doped solid using the light storage protocol based on EIT [52] and employ DD to increase the coherence time. The latter is our benchmark to compare typical state-of-the-art (robust) DD sequences [48, 49, 83, 87, 88] when we increase the field inhomogeneity, i.e., the pulse errors. Our experimental data confirm the prediction and show the relevance of robust CP sequences for quantum memories.

3.2 Characterization of the Magnetic Field Distribution in Three Dimensions

Before we can systematically measure the influence of the driving RF fields' inhomogeneity on DD, we need to accurately characterize the latter. However, in our experiments, copper mounts surround the RF coils. Hence, eddy currents distort the RF fields, and a calculation of the field distribution is essentially not possible with sufficient accuracy. Thus, we developed an experimental setup that allows us to directly measure the three-dimensional Rabi frequency distribution in space.

3.2.1 Experimental Setup

We will later implement light storage to create the coherence on the spin transition between the hyperfine states $|1\rangle = {}^3\mathrm{H}_4(0)\,|m_I = \pm 3/2\rangle$ and $|3\rangle = {}^3\mathrm{H}_4(0)\,|m_I = \pm 1/2\rangle$ of Pr:YSO (see Figure 3.1). Hence, for the measurement of the magnetic field, we drive Rabi oscillations on the same spin transition with the population initially in state $|1\rangle$ and probe the remaining population using the optical transition $|1\rangle \leftrightarrow |2\rangle$ at 605.98 nm. Note that we apply a different type of preparation compared to the previous chapters. In this preparation, we optically pump the crystal such that the probe pulse resonantly couples the populated state $|1\rangle$ to one excited state each in three different frequency ensembles within the inhomogeneous line. We use this so-called three ensemble preparation to increase the optical depth of the medium and thus the light storage efficiency. See [94, 95] for more details.

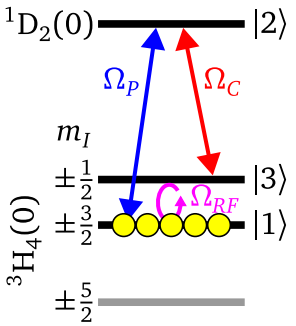

Figure 3.1: Coupling scheme for the light storage and DD experiments in Pr:YSO driven by probe (blue) and control (red) beams as well as RF fields (purple). Yellow circles show the initial population.

Figure 3.2 shows our setup inside the cryostat. We use a 10 mm long Pr:YSO crystal (0.05 % dopant concentration) and create the RF fields to drive the spin transition using two coils wired in series. These coils have a radius of about 5.3 mm such that they can partially enclose the crystal, and a mean separation of 6.3 mm limited by spatial constraints, i.e., they are slightly further apart than in a Helmholtz configuration. Each coil is 2.5 mm long, which provides enough space for up to 14 windings each. To change the inhomogeneity of the magnetic field, we simply change the number of windings N_1 and N_2 of the two coils. We generate the RF pulses resonant to the spin transition at 10.2 MHz with an AWG,[1] amplify[2] them, and use a simple impedance matching circuit [67, 96] to couple them into the coils.

[1] AWG5014, Tektronix
[2] LZY-22+, Mini-Circuits

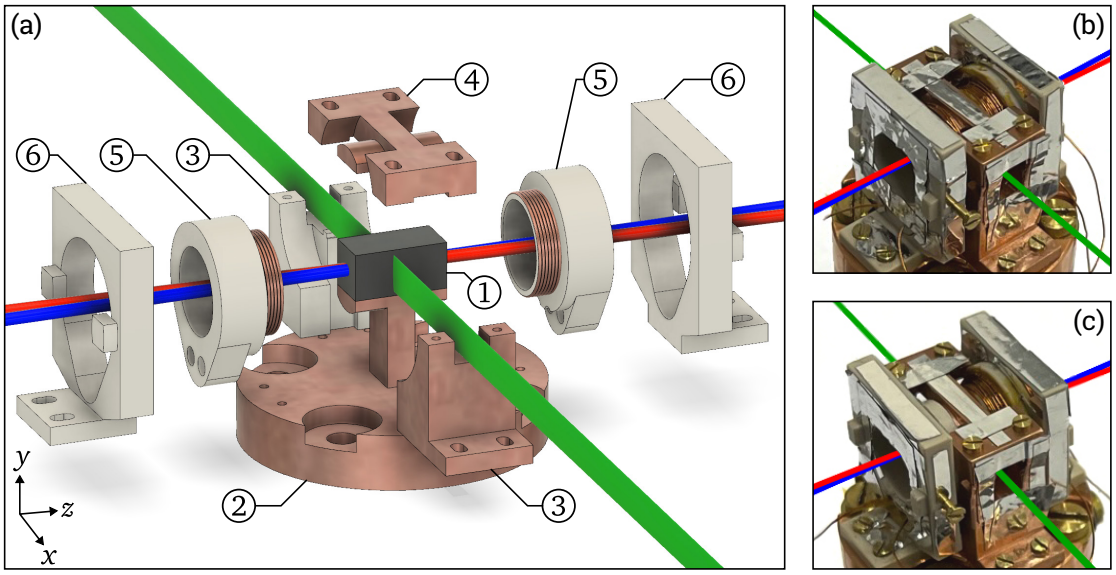

Figure 3.2: (a) Exploded view of the crystal and coil setup. The Pr:YSO crystal ① is pressed on to the copper baseplate ② by the crystal mount sides ③ and top ④. The baseplate connects to the cold finger of the cryostat (not shown). The RF coils ⑤ fit partially around the crystal and are held in place by the coil mounts ⑥. The white parts are manufactured from PEEK; everything else is oxygen-free copper. (b) and (c) Photos of the RF coils, coil mounts, and crystal mount for setups with $N_1 = 10$; $N_2 = 10$ and $N_1 = 14$; $N_2 = 0$ windings, respectively. We clad the exterior surfaces with aluminum tape to reduce the absorption of thermal radiation. Lines represent beamlines with colors matching Figure 3.3.

Figure 3.3 shows the entire experimental setup, with the crystal and coils inside the cryostat in the bottom left. This setup is in large parts identical to the one we used for the NCP experiments (see Figure 2.5 and Section 2.3).

To measure the Rabi oscillations (driven by the RF coils), we employ the same technique as in Chapter 1. We image a probe beam with a diameter of 570 µm (FWHM) in the crystal onto the CCD camera using the same imaging system (lenses L3 and L4) as before. For each pixel of the CCD camera, we determine by a transmission measurement the population left in state $|1\rangle$ when we vary the duration τ of a preceding rectangular RF pulse. Since this population oscillates with the Rabi frequency, we get spatially resolved information on the latter.

However, this gives us only the two-dimensional distribution of the Rabi frequency along the x and y directions but averaged along z (the beam direction). To resolve the Rabi oscillations also in the third dimension, we apply a specific optical preparation which is similar to the one we used for the NCP experiments as described in Section 2.3. We utilize two perpendicular beamlines (preparation and repump) for the optical pumping (see Figure 3.3).

We collimate the preparation beam using lenses L2 and L3 to a diameter of 600 µm (FWHM) such that it counterpropagates to the probe beam with a small angle of about 2° in between. We apply this beam to create spectral pits at the probe and control ($|1\rangle \leftrightarrow |3\rangle$) transitions, as well as at frequencies 10.2 MHz larger than the probe frequency and 10.2 MHz smaller than the control frequency. The latter two pits ensure that in additional ensembles, in which the probe (control)

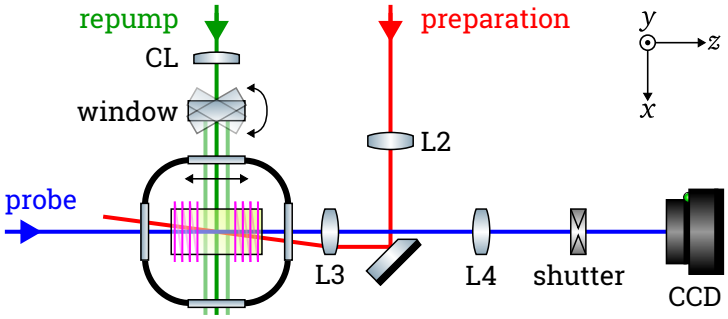

Figure 3.3: Experimental setup with probe (blue), preparation (red), and repump (green) beamlines, Pr:YSO crystal (green), RF coils (purple), lenses (L), cylindrical lens (CL), and CCD camera.

pulses resonantly couple the ${}^3\mathrm{H}_4(0)\,|m_I = \pm 1/2\rangle$ (${}^3\mathrm{H}_4(0)\,|m_I = \pm 3/2\rangle$) state, the population is also in the lowest ground state ${}^3\mathrm{H}_4(0)\,|m_I = \pm 5/2\rangle$. Otherwise, the RF pulses would drive Rabi oscillations in these ensembles and thus disturb the measurements. See [94] for more details on this preparation.

The repump beam, on the other hand, enters the crystal perpendicular to the other beams through a window in the crystal mounts (see Figure 3.2), and we focus it with a cylindrical lens (focal length 150 mm) to a size of 55 µm × 750 µm (FWHM, width × height). We use this beamline to create the antihole on the probe transition. Hence, the crystal remains entirely transparent to the probe pulse except in a thin slice where the preparation and repump beams overlap. We estimate this slice to be about 100 µm thick due to saturation during the optical pumping, but could change the thickness by changing the width of the repump beam. Next, we employ the preparation beam again to pump unwanted population from state $|3\rangle$ to state $|1\rangle$ to create the Λ-system, as depicted in Figure 3.1.

Using this preparation method, we thus get the Rabi frequency distribution in x and y averaged over a thin slice centered around a fixed position in z. Finally, we use a rotatable window[3] (N-BK7, 5 mm thick) in the repump beam path to translate the repump beam along the z direction. The translation range of about 3.5 mm matches the window in the crystal mounts. Thus, we can simply repeat the Rabi frequency measurement with the repump beam in different z positions and get the Rabi frequency distribution spatially resolved in all three dimensions.

Figure 3.4 summarizes the time sequence of these experiments: (i) Preparation of the spectral pits by optical pumping. (ii) Transmission measurement of a probe pulse as reference. (iii) Creation of the antihole on the probe transition only where preparation and repump beam overlap. (iv) Removal of unwanted population from state $|3\rangle$. (v) Driving of Rabi oscillations by an RF pulse with duration τ. (vi) Transmission measurement of a probe pulse to determine the population left in state $|1\rangle$. We repeat the sequence (i–vi) for each repump beam position z and pulse duration τ and average the resulting images at each to reduce noise.

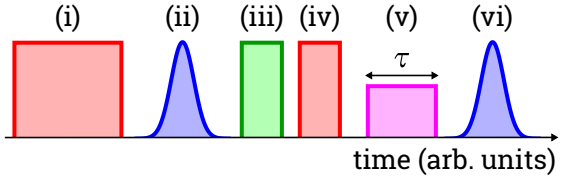

Figure 3.4: Time sequence of optical and RF pulses (see main text). Purple represents RF pulses, the other colors correspond to beamlines from Figure 3.3.

[3] WG11050-A, Thorlabs

3.2.2 Experimental Results

We discuss now the experimental results of our Rabi frequency measurements. In total, we investigate six different coil pairs starting with the same number of windings on both coils ($N_1 = N_2 = 10$) to create an almost homogeneous field and going up to $N_1 = 14$ and $N_2 = -3$ for the largest inhomogeneity.[4] For each coil pair, we determine the Rabi frequency distribution as described above. We measure the population using a probe pulse with a Gaussian intensity profile in time with a duration (FWHM) of 10 µs and a peak Rabi frequency of roughly $2\pi \times 7$ kHz, which leads to only negligible change of the population distribution. We expose the camera to radiation for 40 µs, which ensures detection of the entire probe pulse.

Figure 3.5 shows the Rabi frequency distribution generated by the coil pair with $N_1 = 14$ and $N_2 = 0$, i.e., just a single coil (we show a photo of this setup in Figure 3.2(c)). As we can see, there is a strong gradient along the z direction (beam direction), whereas the Rabi frequency is almost constant in the x-y plane. This is expected for two reasons: When we neglect eddy currents and the slight mismatch between coil radius and separation, we can describe our coil pairs as the sum of a Helmholtz and an Anti-Helmholtz coil. The latter generates a linear gradient in the magnetic quadrupole field, and this gradient is stronger along the coil axis (z direction) than perpendicular to it. More important, however, is that the volume in which we investigate the Rabi frequency is much narrower along the x and y directions compared to the z direction (≈ 250 µm vs. ≈ 2.5 mm).

We perform this same measurement for all six coil pairs and compare the results in Figure 3.6. Since the field inhomogeneity is almost exclusively along the z axis, we average the Rabi frequency along x and y and plot it only vs. z. For further comparability, we normalize each measurement to its mean value.

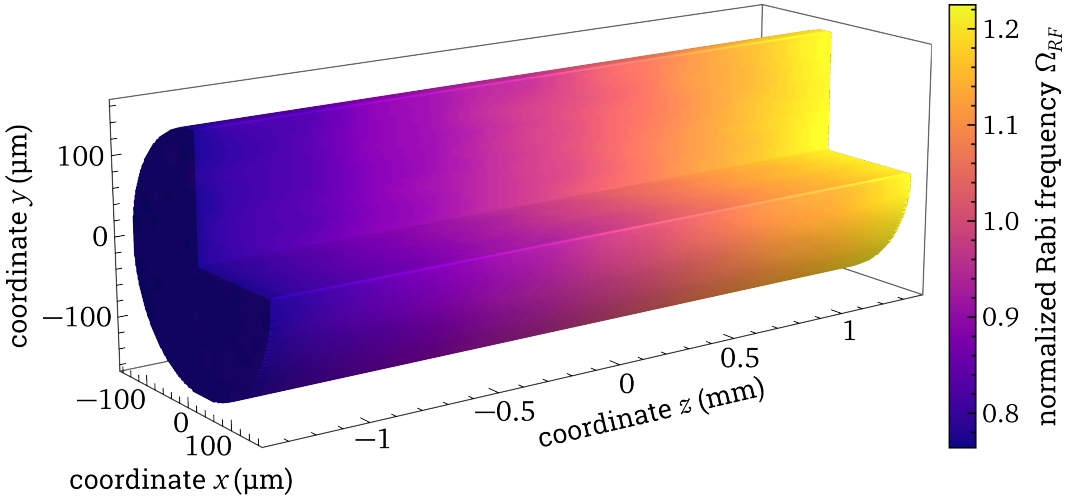

Figure 3.5: Experimentally determined Rabi frequency distribution $\Omega_{RF}(x, y, z)$ normalized to its mean value in three dimensions for the coil setup with $N_1 = 14$; $N_2 = 0$. Note the different scale of the z axis.

[4] Here, the negative number of windings means an inverted winding direction.

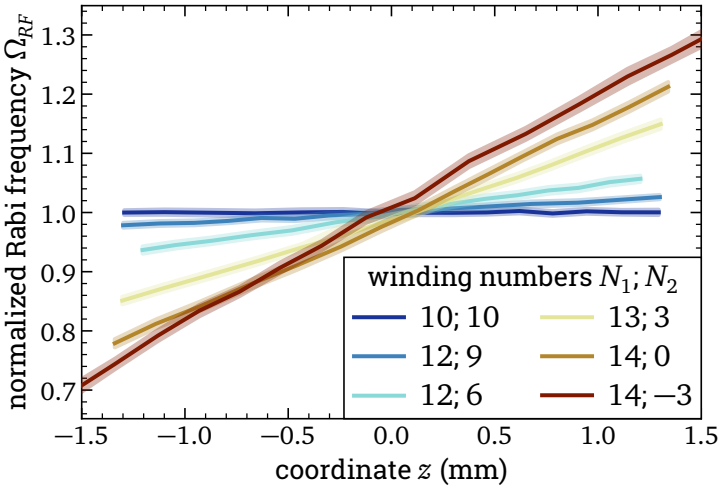

Figure 3.6: Experimentally determined Rabi frequency distribution $\Omega_{RF}(z)$ normalized to its mean value vs. coordinate z for six different coil setups. The data is averaged along the x and y directions. Transparent bands show fit uncertainties and standard deviation due to the averaging. The coils are located at $z = \pm 3.15\,\mathrm{mm}$.

As we can see, for the coil pair with $N_1 = N_2 = 10$, i.e., close to a Helmholtz pair, there is almost no variation of the Rabi frequency. When we increase the difference in windings, the expected linear gradient starts to form and gets steeper the larger the difference in windings becomes. In the most inhomogeneous case ($N_1 = 14$; $N_2 = -3$), the Rabi frequency varies by $\pm 30\,\%$ along the z axis.

In the following, we quantify the inhomogeneity IH by the standard deviation of the data normalized to its mean value. This allows a comparison independent of the shape of the Rabi frequency distribution. We find the smallest value $IH = 0.3\,\%$ and the largest $IH = 18.9\,\%$.

3.3 Basic Theory of DD and EIT Light Storage

Let us now briefly review the basic principle of rephasing and DD [46, 47] (see Figure 3.7). We consider an inhomogeneously broadened ensemble of two-level systems in which we generate a collective coherence at time $t = 0$. Even in an ideal, noiseless environment, the distribution of transition frequencies in the inhomogeneous line leads to a different time evolution of the individual coherences such that they dephase as illustrated in the middle row of Figure 3.7(a). Already shortly after the creation of the coherence, this causes destructive interference and a loss of the net coherence. We can counteract this behavior and recover the net coherence by applying a π pulse at $t = t_S/4$ which inverts the phases and leads to a rephasing at $t = t_S/2$. However, the π pulse inverts not only the phase but also the population, so we need a second π pulse at $t = 3/4t_S$ such that the entire system returns to its initial state at $t = t_S$ and we can read out the coherence [97, 98].

In a real experiment, however, noise causes random changes in the transition frequency of the individual systems, which leads to imperfect rephasing, i.e., a reduction of the coherence amplitude at $t = t_S$ (see bottom row of Figure 3.7(a)). In Pr:YSO this noise is mainly caused by spin flips of yttrium ions [99] which lead to changes in the local magnetic field around the individual praseodymium ions.

DD is a typical way to reduce the effect of this perturbation [46, 47]. Here, we apply many rephasing cycles (consisting in the simplest case of two π pulses each)

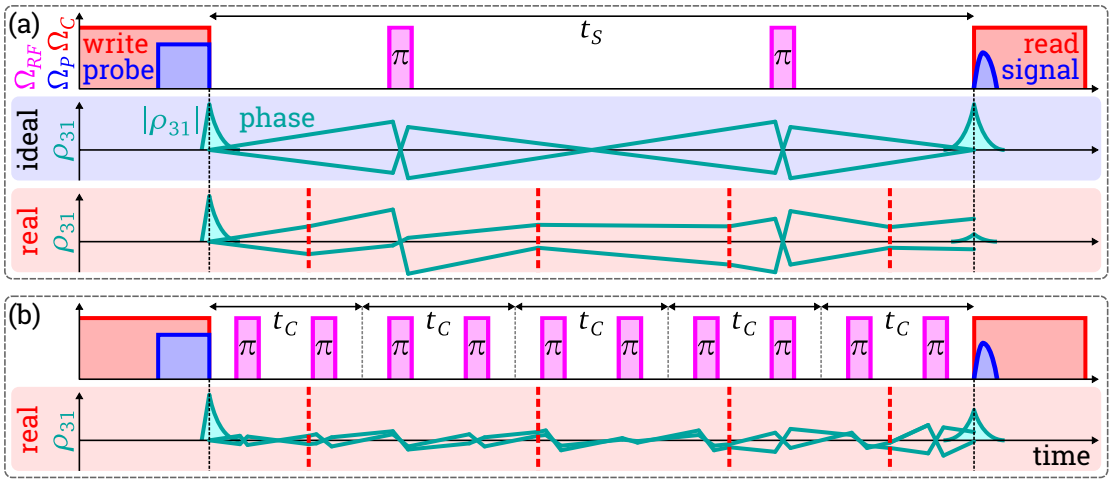

Figure 3.7: Rephasing and DD of an atomic coherence generated by EIT light storage. (a) Rephasing: The top row shows the time sequence of the applied RF (purple) and optical (control (red) and probe (blue)) pulses. The middle and lower rows show the evolution of the amplitude (filled turquoise curves) of the total coherence ρ_{31} summed over the inhomogeneous line and the phase of two constituent coherences (turquoise lines) with different transition frequencies. The middle row depicts the ideal case of a constant environment, and the lower row shows the real environment with random changes in the transition frequencies (indicated by the red, dashed lines). (b) Pulse sequence (top) and coherence evolution (bottom) for DD. Figure modified from [63].

with the duration t_C—also called cycle time—instead of just one. This rephases the coherence after every cycle and, if the cycle time is shorter than the noise correlation time, suppresses the perturbing effect of the frequency fluctuations (see Figure 3.7(b)). Hence, we can recover the net coherence even in the presence of noise.

However, due to the potentially large number of pulses, DD is very susceptible to pulse imperfections, as even minor errors add up and cause a loss of coherence. A typical method to circumvent this problem are CP sequences, as introduced in Section 2.2. However, unlike in Chapter 2, we now use broadband CP sequences, i.e., sequences that are robust with regard to changes in the pulse parameters like pulse area or detuning. This way, pulse imperfections are compensated for, and DD can rephase a coherence even for large numbers of pulses.

In particular, we consider here sequences consisting of pulses with identical pulse area $A = \pi$ and detuning but (potentially) different phases. These sequences replace an entire rephasing cycle, i.e., they consist of an even number of pulses and perform a robust identity operation. In general, we expect that the error compensation improves with the order of the sequence, i.e., the number of pulses per cycle N, due to the increased number of control parameters. However, similar to the discussion in Section 2.4.2, we expect further variations between different classes of sequences.

Light Storage Based On EIT In principle, we could generate the coherence for the following experiments in several ways, the easiest of which is to simply apply a $\pi/2$ pulse to the system. However, since we employ intentionally inhomogeneous

RF fields to test the robustness of DD sequences, using the same RF coils would lead to an inhomogeneous coherence. Adding a second coil pair, on the other hand, would significantly complicate the setup. Furthermore, this coherence would have a single phase across the entire ensemble of ions, and we would thus only test the coherence-preserving capabilities for that specific phase. However, in any quantum information application, it is important that any arbitrary phase is preserved.

Thus, we chose to create the coherence using the light storage protocol based on EIT. This creates a distribution of all phases across the individual coherences and thus allows for a comparison of the various DD sequences in a more realistic scenario. We now briefly review the process of EIT light storage and refer to [52, 63] for more details.

The typical coupling scheme for EIT is a Λ-system with two metastable ground states and a single excited state, as depicted in Figure 3.1. A strong control pulse couples the unpopulated $|3\rangle \leftrightarrow |2\rangle$ transition and renders the medium transparent on the probe transition $|1\rangle \leftrightarrow |2\rangle$. At the same time, it induces a strong dispersion that reduces the group velocity for a temporally overlapping, weak probe pulse. This dispersion depends on the control Rabi frequency Ω_C, such that reducing the latter to zero transfers the probe pulse into a coherence between the ground states $|1\rangle$ and $|3\rangle$. We illustrate this in the top row of Figure 3.7(a): The control "write" pulse stores the probe pulse as a coherence. When we increase the control Rabi frequency again after an arbitrary storage time t_S, the control "read" pulse beats with the atomic coherences to retrieve the signal pulse.

We define the storage efficiency η_{LS} as the ratio between the signal pulse energy and the probe pulse energy. Under ideal conditions, the signal pulse is a copy of the probe pulse, i.e., $\eta_{LS} = 1$. Otherwise, its energy is a measure of the loss of coherence, both from the memory process itself and from decoherence during the storage time. Hence, we can use the storage efficiency to quantify the rephasing capability of DD sequences.

3.4 DD with Inhomogeneous Driving Fields

3.4.1 Experimental Setup

To characterize the performance of different DD sequences in compensating for the previously measured field inhomogeneities, we monitor the rephasing efficiency for EIT light storage. We implement the latter in Pr:YSO using the Λ-system depicted in Figure 3.1. We employ the optical preparation sequence already described in Section 3.2.1 with only a slight modification discussed in [94]. The optical setup as shown in Figure 3.8 is very similar to the one shown in Figure 3.3, and we describe here only the differences. We use lens L1 (focal length 250 mm) to focus the probe beam to a diameter (FWHM) of 170 µm in the crystal. Thus, it is much smaller than the control beam (which utilizes the preparation beamline from Figure 3.3) such that the relevant control Rabi frequency distribution is approximately homogeneous. We further replace the CCD camera with a photodiode[5] since we

[5] 2051-FS, New Focus

require temporal instead of spatial resolution and decrease the focal length of L4 to 50 mm. Finally, we now use a diverging cylindrical lens (focal length −50 mm) to increase the size of the repump beam to 5400 µm × 780 µm (FWHM, width × height) at the crystal position. Since the beam is much wider than the window in the crystal mounts, it prepares the Λ-system homogeneously in the entire volume in which we previously measured the Rabi frequency distribution. Hence, we create the coherence in this entire volume as well, and the individual coherences experience different Rabi frequencies due to the inhomogeneous field.

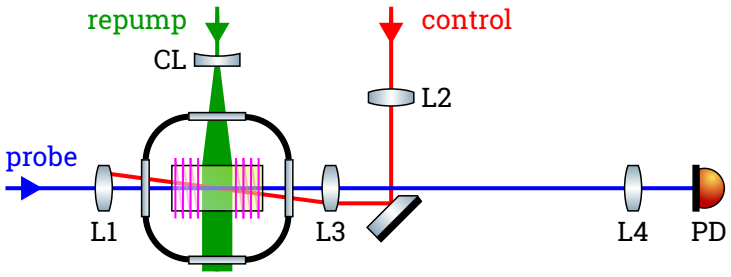

Figure 3.8: Experimental setup with probe (blue), control (red), and repump (green) beamlines, Pr:YSO crystal (green), RF coils (purple), lenses (L), cylindrical lens (CL), and photodiode (PD).

Figure 3.9 summarizes the time sequence of our light storage and DD experiments: (i) Preparation of the spectral pits by optical pumping. (ii) Transmission measurement of a probe pulse as reference. (iii) Creation of the antihole on the probe transition. (iv) Removal of unwanted population in state $|3\rangle$ to create the Λ-system. (v) Storage of a probe pulse as a coherence using EIT. (vi) Optional rephasing or DD by application of M cycles of a DD sequence. (vii) Readout of the coherence as a signal pulse. We repeat the sequence (i–vii) and average the result to reduce noise.

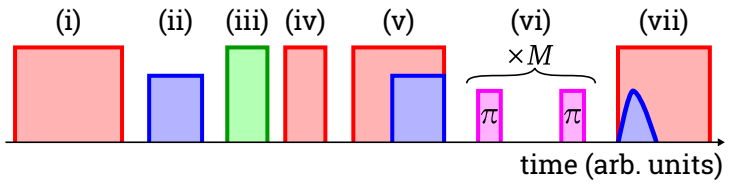

Figure 3.9: Time sequence of optical and RF pulses (see main text). Purple represents RF pulses; the other colors correspond to beamlines from Figure 3.8.

3.4.2 Experimental Results

We discuss now our experimental results on DD with different pulse sequences driven by inhomogeneous RF fields. We apply the time sequence discussed above and presented in Figure 3.9. In particular, we choose rectangular probe pulses with a duration of 10 µs and a Rabi frequency of roughly $2\pi \times 50$ kHz. We optimize the light storage efficiency without rephasing by varying the control Rabi frequency and get typical efficiencies of $\eta_{LS}(t_S = 2\,\mu s) \approx 20\,\%$ at $\Omega_C \approx 2\pi \times 250$ kHz. The exact values depend on the optical alignment on each measurement day.

Next, we apply RF rephasing pulses. We choose these to be rectangular in time with a duration of $\tau = 4\,\mu s$, i.e., a mean Rabi frequency of $\Omega_{RF} = 2\pi \times 125$ kHz limited by the available RF power. In this case, even the minimum Rabi frequency $2\pi \times 87.5$ kHz of the most inhomogeneous field is much larger than

the independently measured inhomogeneous linewidth of the spin transition $\Gamma = 2\pi \times 25\,\mathrm{kHz}$, such that detuning errors are negligible. In systematic measurements, we vary only the DD sequence and the number of cycles M but keep the time per pulse fixed at $t_P = 12.5\,\mu\mathrm{s}$. This short time per pulse ensures a large number of pulses, such that amplitude errors become a significant source of decoherence. The cycle time is $t_C = N \cdot t_P$ with the number of pulses per cycle N that depends on the specific DD sequence. Hence, the storage time is

$$t_S = M \cdot t_C = M \cdot N \cdot t_P = \mathcal{N} \cdot t_P \tag{3.1}$$

with the total number of pulses $\mathcal{N} \equiv M \cdot N$.

Furthermore, we are not interested in the light storage efficiency η_{LS} which includes losses due to the memory process, but only in the efficiency of the rephasing pulses. Hence, we normalize the data to the initial light storage efficiency without DD to obtain the rephasing efficiency $\eta(t_S) = \eta_{LS}(t_S)/\eta_{LS}(2\,\mu\mathrm{s})$.

We compare a total of ten different sequences and list their parameters in Appendix C. Since that many of these sequences perform similarly, we sort them into three groups: The non-robust "Carr, Purcell, Meiboom, Gill" (CPMG) sequence [100, 101]; the low-order robust sequences XY4 [87] and UR4 [83] (with four pulses each); and the high-order sequences XY8 and XY16 [88], KDD and KDD in XY4 [49], and URN with $N \geq 8$ [83]. Hence, to help the clarity of the following analysis, we focus our discussion on CPMG, XY4, KDD in XY4, and UR16 (the latter two being the best of the high-order sequences), i.e., on selected individuals from each group.

In Figure 3.10(a) we compare the rephasing efficiency of these four DD sequences when increasing the number of cycles M—i.e., the storage time t_S—in the case of an almost homogeneous RF field with $IH = 0.3\,\%$ ($N_1 = N_2 = 10$). For short storage times, i.e., few pulses, we see a high rephasing efficiency close to 100 % that confirms the homogeneity of the driving RF fields since no pulse errors reduce the coherence. For longer storage times, we see a decreasing efficiency for all sequences that is predominantly caused by environmental noise but also shows some unexpected oscillations.

From typical noise models based on phase memory [102–104] or an Ornstein-Uhlenbeck process [105–107] we would expect a single stretched exponential decay where the stretching exponent depends on the environmental noise. Following these models, the decay should be exponential if the noise correlation time is much shorter than the pulse separation, and stretched otherwise. From previous experiments [63] and our data, we estimate a short noise correlation time in Pr:YSO on the order of a few microseconds, i.e., smaller than the pulse separation $t_P = 12.5\,\mu\mathrm{s}$ and would thus expect a single exponential decay. However, this does not match the shape we observe in our experiments.

We suspect that a residual, not fully shielded magnetic field in the laboratory causes this discrepancy through a so-called dark state beating [107–110]. This magnetic field lifts the degeneracy of the hyperfine states in Pr:YSO, leading to the creation of coherences with eight unique transition frequencies that evolve differently during the storage time. Hence, during readout, the coherences beat

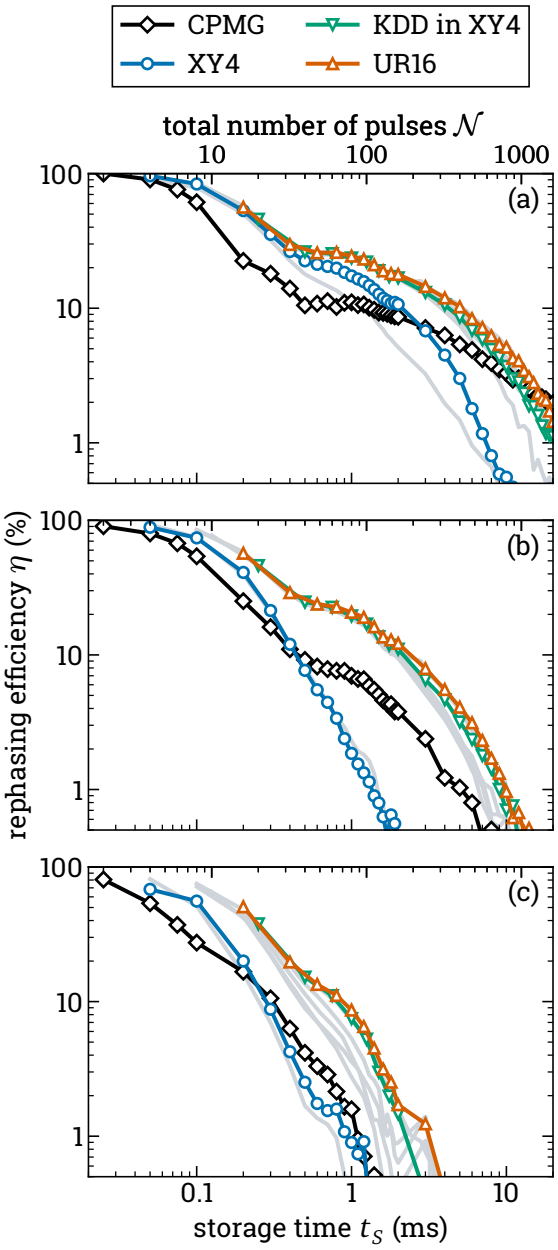

Figure 3.10: DD of coherences created by EIT light storage in Pr:YSO for different coil setups. Variation of the rephasing efficiency η vs. storage time t_S or total number of RF pulses $\mathcal{N}$. The RF field inhomogeneity increases from top to bottom: (a) $IH = 0.3\,\%$ ($N_1 = 10$; $N_2 = 10$), (b) $IH = 9\,\%$ ($N_1 = 13$; $N_2 = 3$), (c) $IH = 19\,\%$ ($N_1 = 14$; $N_2 = -3$). Comparison of four selected DD sequences. We show additional sequences (XY8, XY16, KDD, UR4, UR8, and UR32) in gray.

and the efficiency oscillates with the storage time. We have seen clear evidence of this dark state beating that matches the theory [110] in rephasing experiments with just two π pulses. However, it is not fully clear how the dark state beating affects DD with CP sequences in the presence of pulse errors. Hence, we require a more extensive theoretical treatment to fully confirm dark state beating as the cause for the oscillating shape of our experimental data.

Furthermore, we also see differences between the sequences in Figure 3.10(a), which indicate that there are still residual pulse errors that are better compensated for by some sequences. These might be frequency errors, i.e., a detuning of the RF pulses from resonance, but we assume that they are mostly pulse area errors since it is difficult to perfectly set the correct pulse amplitude.

For CPMG, the simplest DD sequence consisting of two identical pulses per cycle, we see a fast initial drop with increasing number of pulses, i.e., poor error compensation, but a long tail and the highest storage efficiency of all sequences for storage times exceeding 1.5 ms. The latter is presumably caused by the CPMG sequence's ability to preserve coherences with a single phase very well, while it is very sensitive to pulse errors for all other phases [48, 87]. We note that this imbalance also makes CPMG unsuitable for any quantum information application where an arbitrary phase has to be preserved. On the other hand, XY4—probably the best-known robust DD sequence—is phase-insensitive. As we can see in Figure 3.10(a), XY4 (and UR4) also compensate for the remaining pulse errors very well up to about 100 pulses. High-order sequences like the state-of-the-art KDD in XY4 sequence and the universal robust UR16 sequence can even compensate for them up to much higher numbers of pulses. The latter

shows the best performance of all sequences tested over the course of this work.

These results already show that it is always beneficial to use robust DD sequences, even if the pulse errors present in the system are very small and not necessarily caused by field inhomogeneity.

Let us now consider the effect of inhomogeneity in the driving RF fields. In Figures 3.10(b) and 3.10(c) we show the same measurement as before but with a field inhomogeneity of $IH = 9\,\%$ and $IH = 19\,\%$, respectively. We can clearly see that for a higher field inhomogeneity, i.e., larger pulse errors, the rephasing efficiency at short storage times decreases, and the efficiency decays faster when increasing the number of pulses. This effect is most pronounced for the CPMG sequence, whereas the robust DD sequences can compensate for the pulse errors in particular for few pulses. Again, as expected, high-order sequences perform better than low-order sequences, and the difference between the sequences increases (compare UR16 and KDD in XY4 to the other sequences shown as gray lines in Figure 3.10). This confirms the varying error compensation of different sequences.

To further quantify this behavior, we fit the data to a function of the form

$$\eta(t_S) = \mathcal{A} \cdot \exp\left(-\left(\frac{t_S}{T_{2f}}\right)^a\right) + \mathcal{B} \cdot \exp\left(-\left(\frac{t_S}{T_{2s}}\right)^b\right), \tag{3.2}$$

i.e., the sum of two (stretched) exponential decays. Here, T_{2f} and T_{2s} are the coherence times of a fast and a slow decay, while $\mathcal{A}$, $\mathcal{B}$, a, and b are fit constants. We note that so far, this is a fully empirical model, but it still allows us to quantify the data in the presence of dark state beating. We found that we can fix the exponent of the fast decay to $a = 2$, while the exponent of the slow decay varies between $b \approx 0.5$ and 1.

We plot the time constants of both decays vs. the inhomogeneity of the driving RF fields in Figure 3.11. For the fast decay time T_{2f} (Figure 3.11(a)) we see qualitatively the expected behavior: CPMG shows a faster decay, i.e., a shorter decay time, than the robust sequences independent of the field inhomogeneity while all robust sequences perform similarly for homogeneous fields. When increasing the field inhomogeneity, the decay time stays constant for all robust sequences until a threshold is reached (about $IH = 9\,\%$ for XY4 and UR4). At this point, the errors become too large and are no longer fully compensated, i.e., the coherence time decreases. We assume that this threshold increases with the sequence order, but cannot confirm this, since the decay time of all sequences with more than four pulses does not decrease in the range of field inhomogeneities we investigated. We further note that the measured decay is significantly faster than the coherence time of the spin transition $T_2^g = 500\,\mu s$. We assume that this short timescale is just the oscillation period of the dark state beating, but note that a reduced coherence time could also be due to the noise correlation time in our system being shorter than the pulse separation t_P. In this case, DD would not be able to decouple the system from the environment and might—in the presence of pulse errors—even decrease the coherence time.

The slow decay (see Figure 3.11(b)) behaves as expected only for CPMG, which shows a sharp drop in the decay time at about $IH = 2.5\,\%$. XY4 behaves much

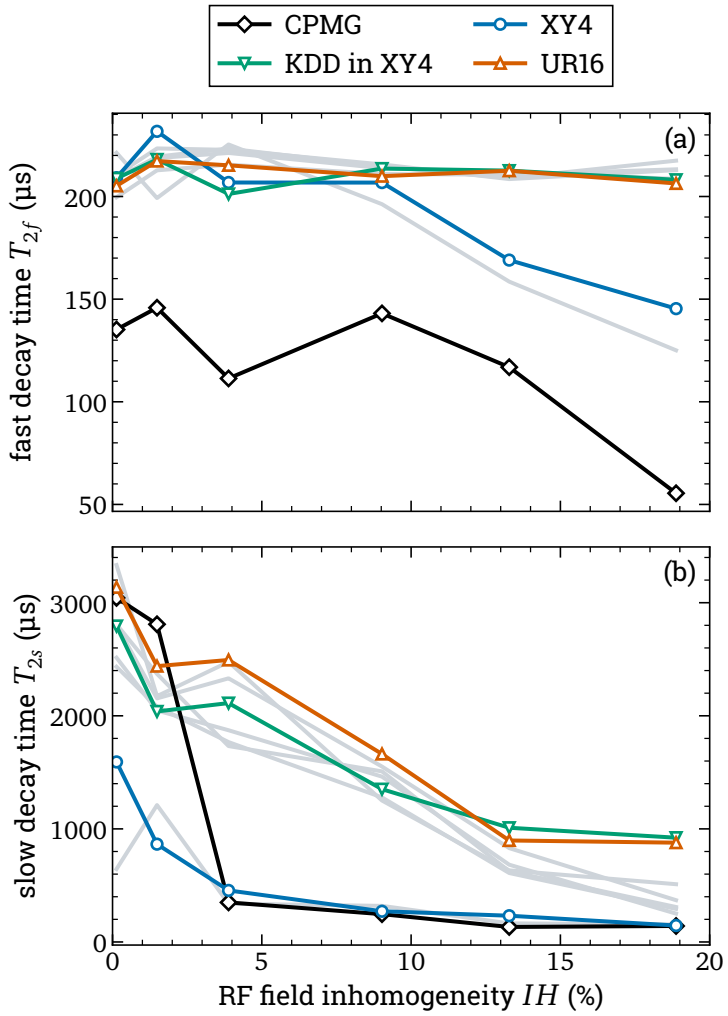

Figure 3.11: DD driven by inhomogeneous RF fields in Pr:YSO. Fast (a) and slow (b) decay times of coherences rephased by DD vs. the driving field's inhomogeneity IH. Comparison of four selected DD sequences. We show additional sequences (XY8, XY16, KDD, UR4, UR8, and UR32 ((b) only)) in gray. Decay times were extracted using fits to Equation (3.2).

worse even for homogeneous fields and drops quickly toward zero. This is also still somewhat expected since XY4 is known to have poor error compensation for large numbers of pulses, i.e., long storage times, as investigated here [48, 83]. However, the high-order sequences perform very differently and do not show the expected threshold behavior described above. Instead, they show a continuously decreasing decay time that remains larger than for CPMG and XY4/UR4. So far, we cannot explain this behavior. We see, however, that the decay time is consistently longer for some sequences. In particular, UR16 shows the slowest decay and even beats the state-of-the-art KDD in XY4 sequence. One could expect that high-order sequences like UR32 would perform even better. However, the cycle time $t_C = 400\,\mu s$ of UR32 is already comparable to the spin coherence lifetime $T_2^g = 500\,\mu s$, and hence decoherence over a single cycle of the sequence outweighs the additional error compensation. In other words, the optimal sequence strongly depends on the medium and pulse parameters. Nevertheless, we see the general trend that the universal robust class of sequences performs better than other

robust sequences of the same or comparable order.

These results confirm the expectation and show that CP sequences are essential for DD, in particular, in the presence of inevitable pulse errors.

Finally, we note that it is not clear that the simple models mentioned above accurately describe the noise in Pr:YSO in the first place, nor that dark state beating causes the oscillation in our data. In fact, there have been reports of multi-exponential decays similar to what we observe in our experiments in rare-earth ion-doped solids [107, 111] and other media [91, 112, 113]. The authors of both [91] and [107], for example, attribute a fast decay to pulse errors and a slower decay to environmental noise. However, contrary to our results, in this case one would expect no dependence of the slow decay time T_{2s} on the field inhomogeneity. The authors of [112] and [111], on the other hand, explain shoulders in their data with noise at specific frequencies. Again, this cannot explain the dependence of the slower timescale on the field inhomogeneity we observe. Moreover, except for [107], the published experiments utilized a fixed number of pulses where the authors varied the pulse separation, whereas we varied the number of pulses. Hence, it is difficult to compare their results to our measurements.

From the shape we observe in our experiments, i.e., the sum of two exponentials (3.2), one could also assume that there may be two classes of ions in which the coherence decays on different timescales. There have been reports of similar effects in rare-earth ion-doped solids due to the random nature of the doping which can lead, e.g., to some dopants being closer together than others [114]. However, in this case, we would expect a fast decay due to fast noise, i.e., it should be exponential with $a = 1$, while the slow decay would show the opposite behavior, i.e., a stretched exponential with $b > 1$. Neither is the case in our experiments. We even find that $b \leq 1$ which the typical noise model [105] cannot describe at all.

However, independent of the unexplained shape, the main result of this chapter remains unchanged: We clearly see that robust DD sequences and in particular the universal robust class of sequences outperform conventional DD sequences in the presence of typically unavoidable inhomogeneities in the driving RF fields.

3.5 Conclusion and Outlook

We presented a showcase experiment for DD with inhomogeneous driving fields. In particular, we used RF pulses to preserve the coherence created by EIT light storage in a Pr:YSO crystal. We varied the inhomogeneity of the RF fields by changing the number of windings on the driving coils and compared the rephasing efficiency of different DD sequences.

As a precondition to quantify the field inhomogeneities, we implemented a setup to directly measure the spatial variation of the Rabi frequency in three dimensions.

We performed systematic measurements where we increased the number of rephasing pulses (and the storage time) for different DD sequences and RF field configurations. We found that even with homogeneous driving fields, CP sequences

increase the rephasing efficiency and coherence time significantly. Moreover, when the field inhomogeneity increases, in particular the non-robust CPMG sequence but also low-order CP sequences show a fast decrease in efficiency. High-order CP sequences, on the other hand, clearly outperform the standard sequences and can compensate for pulse errors to a high degree. In particular, the universal robust class of sequences [83] shows the best error compensation and outperforms other state-of-the-art sequences like KDD in XY4. With our experimental conditions, UR16 was the best sequence, but we note that this can vary depending on the specific experiment.

However, there are still some unresolved issues with the experimental data. We saw oscillations in the efficiency as a function of the storage time, and the error compensation of all DD sequences did not work as well as expected on longer timescales. We suspect that both come from dark state beating [107–110] caused by a residual static magnetic field.

Prospects for Future Work Hence, we suggest that the next step should be to eliminate the dark state beating and to repeat these measurements. One could do so by reducing the magnetic field to 0 but we already utilize passive shielding and while an active compensation is possible, it also causes a large experimental overhead [63, 110]. Instead, one should intentionally apply a magnetic field in a single direction such that the level splitting becomes large enough that one can optically address a single non-degenerate Λ-system. Since the Zeeman splitting in Pr:YSO is on the order of 10 kHz/G [115], a weak field with about 10 G should be sufficient. This provides the additional advantage, that even weak magnetic fields suppress yttrium spin flips, i.e., the main noise source in Pr:YSO, so that the coherence time increases [63, 116, 117]. One could then more easily apply DD with more pulses to better probe the error compensation of CP sequences.

Summary

This research project dealt with the experimental implementation of theory proposals to spatially confine atomic excitations by different techniques of coherent and adiabatic interactions—potentially also below the diffraction limit imposed by the driving light fields. This tight confinement requires a strong nonlinear dependence of the coherent excitation probability on the laser intensities, which we achieved using adiabatic passage processes or NCP sequences.

In the first chapter, we investigated the adiabatic passage processes STIRAP [15] and EIT [26, 45]. They show pronounced robustness against variations of experimental parameters, which leads to a threshold-like behavior of the transfer efficiency vs. laser intensity and, hence, enables spatially tightly confined population dynamics. We applied a STED-like beam geometry with a Gaussian Stokes and a "donut"-shaped pump beam to localize population in the node of the latter. We presented a convincing experimental demonstration and a thorough investigation of both techniques. Our data confirmed that adiabatic passage confines population to spatial extensions far below the beam diameter. With a pump beam waist of $w_p = 100\,\mu\text{m}$, we confined the population to $\Delta r \approx 20\,\mu\text{m}$ for EIT and $\Delta r \approx 3\,\mu\text{m}$ for STIRAP. This is the first implementation of EIT-driven localization in a solid, and the first implementation of the STIRAP-based approach at all. Furthermore, we confirmed that the localization improves with increasing pump intensity and that STIRAP converges to smaller population regions much faster than EIT, as predicted by theory [15, 16, 19]. The data agree very well with numerical simulations and the analytic treatment [19]. We published these results in the special issue "Coherent Control: Photons, Atoms and Molecules" of the Journal of Physics B [51].

Moreover, in the second chapter, we implemented NCP sequences for high-resolution addressing [20–22]. They show a strong dependence of the excitation probability on the laser intensity. Our data confirmed that this confines excitation below the diameter of the driving Gaussian laser profile. This is the first implementation of NCP-driven localization in a solid. With $N = 31$ pulses, we reached a localization to 25 % of the beam diameter, which is far below the previously reported value of $\approx 72\,\%$ [22]. Furthermore, we found that most previously proposed NCP sequences cannot be applied on an inhomogeneously broadened transition. Hence, we collaborated with our theory partners in the team of Nikolay V. Vitanov (University of Sofia) to develop specific sequences matched to our medium. We compared them to several previously published classes of sequences and confirmed that the confinement improves with the number of pulses but also strongly depends on the class of sequence, as predicted by theory [74]. The results, in particular regarding the inhomogeneously broadened line, agree very well with the numerical simulation. We are currently preparing a manuscript to publish these results.

These proof-of-principle experiments on localization by STIRAP or NCP sequences still operated well above the diffraction limit. Nevertheless, they permit extrapolation toward obtaining spatially confined population in the subdiffraction

regime. This will be relevant to quantum information technology and well beyond.

Finally, in the last chapter, we investigated CP sequences in the context of error compensation. We provided a simple showcase experiment where we increased the coherence time of a quantum memory using DD, but intentionally introduced pulse errors in the form of inhomogeneous driving fields. We fully characterized these inhomogeneities and performed systematic measurements to compare the ability of various robust DD sequences to compensate for the errors. Our data showed that even in the case of homogeneous driving fields, robust DD sequences improve the coherence time. This difference becomes even more pronounced when the inhomogeneity increases. In particular, we found that the universal robust sequences [83] outperform other sequences of the same or similar order.

As the next step, we will perform additional measurements without dark state beating and then publish the results of this showcase experiment.

Zusammenfassung

Die vorliegende Arbeit befasst sich mit der experimentellen Umsetzung von theoretischen Vorschlägen zur räumlichen Begrenzung von atomarer Anregung durch verschiedene Techniken kohärenter und adiabatischer Wechselwirkungen. Diese erlauben es prinzipiell auch unterhalb des Beugungslimits der treibenden Lichtfelder zu lokalisieren. Eine solche enge Lokalisierung erfordert eine starke nichtlineare Abhängigkeit der kohärenten Anregungswahrscheinlichkeit von den Laserintensitäten, die wir mit adiabatischen Transferprozessen oder schmalbandigen Kompositpulssequenzen (kurz NCP-Sequenzen von engl. *narrowband composite pulse*) erreicht haben.

Im ersten Kapitel haben wir die beiden adiabatischen Transferprozesse der *stimulierten Raman-adiabatischen Passage* (STIRAP) und der *elektromagnetisch induzierten Transparenz* (EIT) untersucht. Diese zeigen eine ausgeprägte Robustheit gegenüber Variationen der experimentellen Parameter, was zu einem schwellenartigen Verhalten der Transfereffizienz gegenüber der Laserintensität führt. Letzteres ermöglicht eine räumlich eng begrenzte Besetzungsdynamik. Wir haben eine Strahlgeometrie ähnlich der STED-Mikroskopie (engl. stimulated emission depletion) mit einem Gaußschen Stokes- und einem „Donut“-förmigen Pumpstrahl verwendet, um die Besetzung im Zentrum des Pumpstrahls zu lokalisieren. Wir haben eine überzeugende experimentelle Demonstration und eine gründliche Untersuchung beider Techniken präsentiert. Unsere Daten haben bestätigt, dass der adiabatische Transfer die Besetzung auf räumliche Ausdehnungen weit unterhalb des Strahldurchmessers lokalisiert. Bei einer Pumpstrahltaille von $w_p = 100\,\mu\text{m}$ haben wir die Besetzung auf einen Durchmesser von $\Delta r \approx 20\,\mu\text{m}$ für EIT und $\Delta r \approx 3\,\mu\text{m}$ für STIRAP begrenzt. Dies stellt die erste Implementierung der EIT-basierten Lokalisierung in einem Festkörper und die erste Implementierung des STIRAP-basierten Ansatzes überhaupt dar. Weiterhin haben wir bestätigt, dass sich die Lokalisierung mit zunehmender Pumpintensität verbessert und dass STIRAP, wie von der Theorie vorhergesagt, viel schneller zu kleineren Besetzungsregionen konvergiert als EIT. Die Daten stimmen sehr gut mit numerischen Simulationen und der analytischen Rechnung [19] überein. Wir haben diese Ergebnisse in der Sonderausgabe „Coherent Control: Photons, Atoms and Molecules“ des Journal of Physics B veröffentlicht [51].

Weiterhin haben wir im zweiten Kapitel NCP-Sequenzen für die hochauflösende Adressierung implementiert. Diese zeigen eine starke Abhängigkeit der Anregungswahrscheinlichkeit von der Laserintensität. Unsere Daten haben bestätigt, dass sie dadurch die Anregung unter den Durchmesser des Gauß-förmigen Strahlprofils begrenzen. Dies ist die erste Implementierung von NCP-basierter Lokalisierung in einem Festkörper. Mit $N = 31$ Pulsen haben wir eine Lokalisierung auf 25 % des Strahldurchmessers erreicht, was weit unter dem zuvor veröffentlichten Wert von ca. 72 % [22] liegt. Ferner haben wir festgestellt, dass die meisten zuvor veröffentlichten NCP-Sequenzen nicht auf einem inhomogen verbreiterten Übergang angewendet werden können. Daher haben wir mit unseren Theoriepartnern in der Gruppe von Nikolay V. Vitanov (Universität Sofia) zusammengearbeitet, um

Sequenzen zu entwickeln, die auf unser Medium angepasst sind. Wir haben sie mit mehreren bereits veröffentlichten Klassen von Sequenzen verglichen und bestätigt, dass sich die Lokalisierung mit der Anzahl der Pulse verbessert, aber auch, wie von der Theorie vorhergesagt [74], stark von der Klasse der Sequenz abhängt. Die Ergebnisse – insbesondere auch in Bezug auf die inhomogen verbreiterte Linie – stimmen sehr gut mit einer numerischen Simulation überein. Wir bereiten derzeit ein Manuskript zur Veröffentlichung dieser Ergebnisse vor.

Diese grundsätzlichen Experimente zur Lokalisierung durch STIRAP bzw. NCP-Sequenzen haben wir noch weit oberhalb des Beugungslimits durchgeführt. Dennoch erlauben sie eine Extrapolation auf die räumliche Begrenzung von Besetzung im Bereich unterhalb des Beugungslimits. Dies wird für die Quanteninformationstechnologie und weit darüber hinaus von Bedeutung sein.

Im letzten Kapitel haben wir Kompositpulssequenzen in Bezug auf Fehlerkompensation untersucht. Wir haben ein einfaches Demonstrationsexperiment durchgeführt, bei dem wir die Kohärenzzeit eines Quantenspeichers mithilfe von *dynamischer Dekohärenzkontrolle* (DD) erhöht haben, gleichzeitig aber absichtlich Pulsfehler in Form von inhomogenen Entkopplungspulsen eingeführt haben. Wir haben diese Inhomogenitäten vollständig charakterisiert und systematische Messungen durchgeführt, um zu vergleichen, wie gut verschiedene robuste DD-Sequenzen die Fehler kompensieren. Unsere Daten haben gezeigt, dass robuste DD-Sequenzen selbst im Falle homogener Pulse die Kohärenzzeit verbessern. Dieser Unterschied wird noch deutlicher, wenn die Inhomogenität zunimmt. Insbesondere haben wir bestätigt, dass die universell-robusten Sequenzen [83] andere Sequenzen gleicher oder ähnlicher Ordnung, d. h. Pulszahl, übertreffen.

In einem nächsten Schritt werden wir weitere Messungen, die nicht durch eine Dunkelzustandsschwebung limitiert sind, durchführen, um dann die Ergebnisse dieses Demonstrationsexperiments zu veröffentlichen.

Appendix A

Parameters of NCP Sequences for Localization

We give now the relevant parameters, i.e., the phases, of all NCP sequences we used for localization in Chapter 2. All of them were derived by our theory cooperation partners in the group of Nikolay V. Vitanov. In particular, he developed the antisymmetric and optimized sequences specifically for this work and they have not yet been published elsewhere.

We can calculate the phases ϕ_k of an analytic NCP sequence with an odd number of pulses N from [21]

$$\phi_k = \begin{cases} \frac{k\pi}{N} & (k = 2, 4, 6, \ldots, N-1), \\ -\frac{(k-1)\pi}{N} & (k = 1, 3, 5, \ldots, N). \end{cases} \tag{A.1}$$

In all other cases, the sequences were derived numerically, and we list their phases in the following tables. We give all phases ϕ_k in units of π.

Table A.1: The phases (in units of π) of the symmetric sequences [20]. The sequences are symmetric, i.e., of the form $(\phi_1 = 0, \phi_2, \ldots, \phi_l, \ldots, \phi_2, \phi_1 = 0)$ with $N = 2l - 1$. We list only the first l phases.

Pulse count N	Phases $(\phi_1, \phi_2, \ldots, \phi_l)$
5	(0, 0.839, 1.42)
9	(0, 0.426, 1.49, 0.858, 1.3)
13	(0, 1.103, 0.876, 0.154, 1.708, 1.02, 0.229)
21	(0, 1.073, 0.919, 0.131, 1.831, 1.156, 0.721, 0.096, 1.521, 0.812, 1.954)

Table A.2: The phases (in units of π) of the numeric sequences with the excitation threshold $\epsilon = 0.01\,\%$ [74].

Pulse count N	Phases $(\phi_1, \phi_2, \ldots, \phi_N)$
3	(0, 0.65, 1.301)
5	(0, 0.332, 1.58, 0.828, 1.16)
7	(0, 0.663, 0.506, 1.842, 1.178, 1.021, 1.684)
9	(0, 0.478, 0.959, 1.61, 1.132, 0.654, 1.306, 1.786, 0.265)
11	(0, 0.804, 0.889, 1.387, 1.568, 1.875, 0.183, 0.364, 0.863, 0.948, 1.753)

Table A.3: The phases (in units of π) of the numeric sequences with the excitation threshold $\epsilon = 0.1\,\%$ [74].

Pulse count N	Phases $(\phi_1, \phi_2, \ldots, \phi_N)$
3	(0, 0.631, 1.262)
5	(0, 0.295, 1.575, 0.856, 1.151)
7	(0, 0.612, 0.409, 1.796, 1.182, 0.98, 1.591)
9	(0, 0.417, 0.837, 1.471, 1.055, 0.639, 1.273, 1.693, 0.11)
11	(0, 0.776, 0.859, 1.313, 1.472, 1.744, 0, 0.153, 0.576, 0.643, 1.399)

Table A.4: The phases (in units of π) of the numeric sequences with the excitation threshold $\epsilon = 1\,\%$ [74].

Pulse count N	Phases $(\phi_1, \phi_2, \ldots, \phi_N)$
3	(0, 0.587, 1.174)
5	(0, 0.238, 1.58, 0.923, 1.161)
7	(0, 0.124, 1.82, 0.502, 1.183, 0.879, 1.003)
9	(0, 0.335, 0.677, 1.27, 0.938, 0.605, 1.199, 1.54, 1.875)
11	(0, 0.281, 0.313, 1.784, 0.1, 0.597, 1.094, 1.411, 0.883, 0.917, 1.2)

Table A.5: The phases (in units of π) of the optimized sequences. The sequences are antisymmetric, i.e., of the form $(\phi_1, \phi_2, \ldots, \phi_l = 0, \ldots, -\phi_2, -\phi_1)$ with $N = 2l - 1$. We list only the first l phases.

Pulse count N	Phases $(\phi_1, \phi_2, \ldots, \phi_l)$
3	(0.5961, 0)
5	(0.9107, 0.2493, 0)
7	(0.8947, 0.5874, 1.8962, 0)
9	(0.8439, 1.3539, 1.8271, 1.5887, 0)
11	(1.4433, 0.7439, 0.6835, 0.3272, 0.2091, 0)
13	(1.576, 0.8705, 0.8232, 0.456, 0.3701, 0.1432, 0)
15	(1.8023, 1.0941, 1.0447, 0.6594, 0.5732, 0.3151, 0.1843, 0)
17	(0.2352, 0.8624, 1.0553, 1.2164, 1.4625, 1.6732, 1.5441, 0.0311, 0)
19	(1.8479, 1.2751, 0.981, 0.9493, 0.6312, 0.4917, 0.3592, 0.4262, 1.887, 0)
21	(1.7514, 1.3271, 1.0313, 0.8945, 0.5592, 0.5767, 0.6626, 0.4913, 1.8487, 0.0381, 0)
23	(1.6864, 1.4253, 1.1396, 0.767, 0.4155, 0.7338, 0.8962, 0.5376, 0.1081, 0.2852, 1.9109, 0)
25	(1.6293, 1.6013, 1.2881, 0.7557, 0.7333, 0.6666, 0.6003, 0.991, 0.4791, 0.1233, 0.0644, 0.1627, 0)
27	(0.2779, 1.7844, 1.3326, 1.4903, 1.1737, 0.941, 0.8286, 0.9406, 0.4875, 0.4249, 0.5421, 0.1645, 0.1325, 0)
29	(0.9509, 0.678, 0.1595, 1.9907, 0.0682, 0.031, 1.4253, 1.5511, 1.4331, 1.239, 1.1535, 0.738, 0.5688, 0.433, 0)
31	(1.0001, 1.4601, 1.756, 0.0908, 0.0722, 0.1049, 0.4856, 0.7993, 0.7721, 0.5517, 1.137, 1.2393, 1.4059, 1.6235, 1.698, 0)

Table A.6: The phases (in units of π) of the antisymmetric sequences with the excitation threshold $\epsilon = 1\,\%$. The sequences are antisymmetric, i.e., of the form $(\phi_1, \phi_2, \ldots, \phi_l = 0, \ldots, -\phi_2, -\phi_1)$ with $N = 2l - 1$. We list only the first l phases.

Pulse count N	Phases $(\phi_1, \phi_2, \ldots, \phi_l)$
3	(0.5867, 0)
5	(0.4167, 0.6531, 0)
7	(0.4962, 0.3741, 0.6722, 0)
9	(0.2638, 0.5868, 0.9098, 0.3231, 0)
11	(1.0521, 0.8626, 0.1783, 0.286, 0.3356, 0)
13	(0.3081, 0.3103, 0.7134, 1.0449, 0.4763, 0.3045, 0)
15	(0.808, 0.7523, 0.8893, 0.5425, 1.8546, 0.0639, 1.9734, 0)
17	(0.5511, 0.5869, 0.255, 0.1629, 0.542, 0.8862, 0.4558, 0.4502, 0)
19	(0.772, 0.8166, 1.384, 1.5422, 1.6391, 1.3322, 1.6465, 0.0531, 1.8781, 0)
21	(0.7721, 0.3532, 0.3977, 0.3727, 0.2405, 0.4101, 0.8202, 0.6987, 0.6325, 0.0469, 0)
23	(0.2855, 0.5246, 0.0672, 0.2785, 0.6819, 0.9743, 0.7609, 0.7125, 0.5803, 0.2815, 1.9764, 0)
25	(0.7752, 0.7436, 0.8543, 0.9156, 0.951, 0.3405, 0.3542, 0.1142, 1.7152, 1.8812, 0.1249, 0.2441, 0)
27	(0.9106, 0.7793, 0.8741, 0.919, 0.6748, 0.1305, 0.4263, 0.3121, 0.1732, 0.031, 1.5934, 1.601, 1.8221, 0)
29	(1.592, 1.6943, 1.8226, 1.6936, 1.7099, 1.148, 1.0171, 1.2158, 1.3742, 1.1667, 1.3745, 1.755, 1.7427, 0.0888, 0)
31	(0.1506, 0.1473, 0.4329, 0.6354, 0.4592, 0.6133, 0.5471, 0.909, 0.8177, 0.8211, 0.8799, 0.2678, 0.0471, 0.1753, 0.1386, 0)
33	(0.0605, 0.3173, 0.3687, 0.3214, 0.7288, 0.691, 0.4768, 0.5922, 0.755, 1.0539, 0.9969, 0.4875, 0.5086, 0.1605, 0.0942, 1.9699, 0)
35	(0.7764, 0.8959, 0.4011, 0.3161, 0.2605, 0.1795, 0.3489, 0.6039, 0.5421, 0.2292, 0.3143, 0.6859, 0.6385, 0.7293, 0.4954, 0.4996, 0.1466, 0)
37	(1.9595, 0.0756, 0.1623, 0.3757, 0.6084, 1.002, 0.7508, 0.4055, 0.5571, 0.5575, 0.6507, 0.592, 0.8204, 0.5076, 0.553, 0.49, 0.0528, 0.0186, 0)

39	(0.1087, 0.2857, 0.1066, 0.5401, 0.5102, 0.5232, 0.6996, 0.7261, 0.3576, 0.5627, 0.9152, 1.0572, 0.921, 0.6668, 0.4357, 0.3466, 0.0842, 1.9795, 0.0811, 0)
41	(0.011, 1.9903, 0.1027, 0.1698, 0.7533, 0.6829, 0.554, 0.755, 0.6636, 0.5558, 0.3994, 0.5137, 0.7315, 0.8742, 0.634, 0.6768, 0.3095, 0.1907, 0.2657, 0.2342, 0)
43	(0.7016, 0.5836, 0.6095, 0.2795, 0.5116, 0.3351, 0.2791, 0.3566, 0.132, 0.0988, 0.6051, 0.6613, 0.5835, 0.5485, 0.7326, 0.85, 0.7427, 0.6024, 0.2946, 1.9385, 1.9916, 0)
45	(0.1309, 0.0921, 0.2904, 0.1137, 0.1668, 0.5634, 0.8871, 0.6043, 0.8313, 0.7831, 0.786, 0.7749, 0.4961, 0.4196, 0.2216, 0.3962, 0.7556, 0.6052, 0.5514, 0.4025, 0.2568, 0.0817, 0)

Table A.7: The phases (in units of π) of the antisymmetric sequences with the excitation threshold $\epsilon = 3\,\%$. The sequences are antisymmetric, i.e., of the form $(\phi_1, \phi_2, \ldots, \phi_l = 0, \ldots, -\phi_2, -\phi_1)$ with $N = 2l - 1$. We list only the first l phases.

Pulse count N	Phases $(\phi_1, \phi_2, \ldots, \phi_l)$
3	(0.5478, 0)
5	(0.4014, 0.6036, 0)
7	(0.4679, 0.3661, 0.6192, 0)
9	(0.2743, 0.5479, 0.8215, 0.2737, 0)
11	(0.9405, 0.7834, 0.1544, 0.243, 0.2838, 0)
13	(0.3107, 0.3125, 0.6529, 0.9397, 0.41, 0.2559, 0)
15	(0.7374, 0.6918, 0.8046, 0.5114, 1.8791, 0.0525, 1.9782, 0)
17	(0.5133, 0.5426, 0.2648, 0.1967, 0.5245, 0.8278, 0.4145, 0.3883, 0)
19	(1.0857, 1.0493, 0.5481, 0.3897, 0.2779, 0.5719, 0.3104, 1.9541, 0.1001, 0)
21	(0.6942, 0.3357, 0.3807, 0.3709, 0.2512, 0.4053, 0.771, 0.6325, 0.5603, 0.0383, 0)
23	(0.2924, 0.4908, 0.0825, 0.316, 0.6696, 0.8921, 0.6873, 0.6276, 0.4963, 0.236, 1.9807, 0)
25	(0.7102, 0.6844, 0.7749, 0.8227, 0.8514, 0.3148, 0.3486, 0.1098, 1.7439, 1.8907, 0.1027, 0.2023, 0)
27	(0.8224, 0.7147, 0.7939, 0.8286, 0.6261, 0.1426, 0.42, 0.3223, 0.1844, 0.0327, 1.6501, 1.6654, 1.8534, 0)
29	(1.6074, 1.6911, 1.7964, 1.6895, 1.7042, 1.2068, 1.0931, 1.2621, 1.448, 1.2699, 1.4561, 1.7986, 1.7795, 0.0726, 0)
31	(0.1817, 0.1791, 0.4162, 0.5895, 0.4411, 0.5726, 0.5109, 0.8268, 0.7237, 0.7531, 0.7822, 0.2231, 0.0388, 0.144, 0.1134, 0)
33	(0.1076, 0.3212, 0.3644, 0.3211, 0.6773, 0.6392, 0.4342, 0.559, 0.712, 0.9352, 0.8841, 0.4095, 0.4257, 0.131, 0.0774, 1.9754, 0)
35	(0.6983, 0.796, 0.3625, 0.3012, 0.2514, 0.1598, 0.3449, 0.5826, 0.5269, 0.2746, 0.3443, 0.6698, 0.5971, 0.6582, 0.4339, 0.4226, 0.1203, 0)
37	(0.0242, 0.1193, 0.1903, 0.3682, 0.57, 0.9328, 0.7434, 0.4211, 0.5309, 0.5416, 0.6052, 0.5277, 0.7331, 0.4429, 0.4777, 0.4172, 0.043, 0.0152, 0)

39	(0.1473, 0.2929, 0.1416, 0.5286, 0.4652, 0.4965, 0.6626, 0.6447, 0.3384, 0.5618, 0.8585, 0.9491, 0.803, 0.5649, 0.3634, 0.2886, 0.07, 1.9827, 0.0663, 0)
41	(0.0664, 0.0495, 0.1414, 0.1955, 0.7154, 0.6562, 0.5504, 0.7447, 0.6492, 0.5413, 0.383, 0.4808, 0.6518, 0.7745, 0.5615, 0.5837, 0.2593, 0.1611, 0.2231, 0.1936, 0)
43	(0.6363, 0.5398, 0.5615, 0.2827, 0.4953, 0.3144, 0.2971, 0.3573, 0.1462, 0.1637, 0.6029, 0.6108, 0.5325, 0.5156, 0.6891, 0.7832, 0.6697, 0.5245, 0.2502, 1.9499, 1.9932, 0)
45	(0.1645, 0.1328, 0.2964, 0.1451, 0.1981, 0.5419, 0.8303, 0.5633, 0.7738, 0.7455, 0.7538, 0.7288, 0.4698, 0.3898, 0.2241, 0.377, 0.6715, 0.5291, 0.4697, 0.3362, 0.2116, 0.0668, 0)

Table A.8: The phases (in units of π) of the antisymmetric sequences with the excitation threshold $\epsilon = 10\,\%$. The sequences are antisymmetric, i.e., of the form $(\phi_1, \phi_2, \ldots, \phi_l = 0, \ldots, -\phi_2, -\phi_1)$ with $N = 2l - 1$. We list only the first l phases.

Pulse count N	Phases $(\phi_1, \phi_2, \ldots, \phi_l)$
3	(0.4796, 0)
5	(0.3645, 0.5224, 0)
7	(0.2602, 0.637, 0.3768, 0)
9	(0.2679, 0.4796, 0.6912, 0.2117, 0)
11	(0.7827, 0.6637, 0.122, 0.1889, 0.2195, 0)
13	(0.2954, 0.2967, 0.5593, 0.7861, 0.3226, 0.1965, 0)
15	(0.628, 0.5938, 0.6786, 0.4522, 1.9083, 0.0394, 1.9837, 0)
17	(0.4499, 0.4718, 0.2591, 0.2138, 0.4729, 0.7195, 0.346, 0.3069, 0)
19	(0.1604, 0.4132, 0.3959, 0.5442, 0.5017, 0.7561, 0.5058, 0.0744, 0.0879, 0)
21	(0.5854, 0.3046, 0.3457, 0.3471, 0.2463, 0.3761, 0.6804, 0.5324, 0.4586, 0.0287, 0)
23	(0.2819, 0.4323, 0.0969, 0.3351, 0.6166, 0.7596, 0.5734, 0.5078, 0.3885, 0.1808, 1.9856, 0)
25	(0.6081, 0.5888, 0.6566, 0.6908, 0.7123, 0.2779, 0.3276, 0.101, 1.789, 1.9087, 0.0773, 0.1536, 0)
27	(0.692, 0.6112, 0.6716, 0.6961, 0.543, 0.1473, 0.3933, 0.311, 0.18, 0.0325, 1.7255, 1.744, 1.8897, 0)
29	(1.6432, 1.7059, 1.7847, 1.7039, 1.7158, 1.3101, 1.2191, 1.3519, 1.552, 1.411, 1.5643, 1.849, 1.8274, 0.0543, 0)
31	(0.1741, 0.2498, 0.3431, 0.493, 0.4895, 0.3612, 0.5769, 0.6362, 0.5895, 0.6998, 0.605, 0.1247, 0.1155, 0.0053, 0.1562, 0)
33	(0.1435, 0.3053, 0.3383, 0.3026, 0.5877, 0.5517, 0.3699, 0.4966, 0.6328, 0.769, 0.7248, 0.3135, 0.3248, 0.0975, 0.058, 1.9817, 0)
35	(0.5883, 0.6616, 0.3128, 0.2751, 0.2333, 0.1405, 0.3266, 0.5326, 0.4848, 0.3006, 0.3435, 0.605, 0.515, 0.5453, 0.3476, 0.327, 0.0902, 0)
37	(0.08, 0.1512, 0.2045, 0.34, 0.5001, 0.8097, 0.6884, 0.4069, 0.4672, 0.4862, 0.5233, 0.4322, 0.6044, 0.3549, 0.3785, 0.3252, 0.0322, 0.0114, 0)

39	(0.1729, 0.2825, 0.1659, 0.4838, 0.3964, 0.4472, 0.586, 0.5307, 0.3071, 0.5287, 0.7521, 0.7887, 0.6426, 0.4375, 0.277, 0.2196, 0.0532, 1.9868, 0.0495, 0)
41	(0.1116, 0.099, 0.1677, 0.2077, 0.6355, 0.589, 0.5094, 0.688, 0.592, 0.4895, 0.3402, 0.4179, 0.5383, 0.6326, 0.4567, 0.4611, 0.1986, 0.1243, 0.1711, 0.1463, 0)
43	(0.5417, 0.4694, 0.486, 0.2708, 0.4489, 0.2784, 0.2983, 0.3323, 0.1512, 0.2125, 0.5571, 0.5221, 0.4528, 0.4592, 0.6113, 0.6728, 0.5575, 0.4188, 0.1941, 1.9626, 1.9949, 0)
45	(0.1852, 0.1616, 0.2847, 0.1668, 0.2139, 0.4869, 0.7253, 0.4896, 0.6735, 0.6646, 0.6744, 0.6353, 0.41, 0.3337, 0.2068, 0.3288, 0.5464, 0.4222, 0.365, 0.2562, 0.1592, 0.0499, 0)

Appendix B

Incoherent Population Transfer in NCP Experiments

During our experiments on localization by NCP sequences, we found some background population transfer. Here, we present systematic measurements and numerical simulations to determine its origin.

We can extract information about this background from fits to the ring-type localization we presented in Section 2.4.4, i.e., experiments where the pulse area in the center of the beam is 2π. Here, population transfer should be suppressed everywhere except in a ring on the wings of the beam profile, where $A(r) = \pi$. However, as we can see in Figure B.1 (blue line), where we show a cut through the experimentally determined population distribution after localization, this is not the case. Instead, we see three distinguishable features: The expected narrow ring of population localized by the NCP sequence (black, dashed line); a wider ring from decay of the excited state during the NCP sequence (orange, dash-dotted line); and a broad background caused by direct incoherent population transfer (green line). We can quantify these features with a fit of the form

$$P_3(r) = \underbrace{p_l \cdot \exp\left(-\left(\frac{r-r_0}{w_l}\right)^2\right)}_{\text{localization}} + \underbrace{p_d \cdot \exp\left(-\left(\frac{r-r_0}{w_d}\right)^d\right)}_{\text{decay}} + \underbrace{p_c \cdot \exp\left(-\left(\frac{r}{w_c}\right)^2\right)}_{\text{incoherent transfer}}, \tag{B.1}$$

where r is the radial coordinate and r_0 is the radius of the ring. p_i and w_i with $i = c, d, l$ are the amplitude and width of the three features, and $d > 2$ is an exponent to describe the saturated profile of the decay.

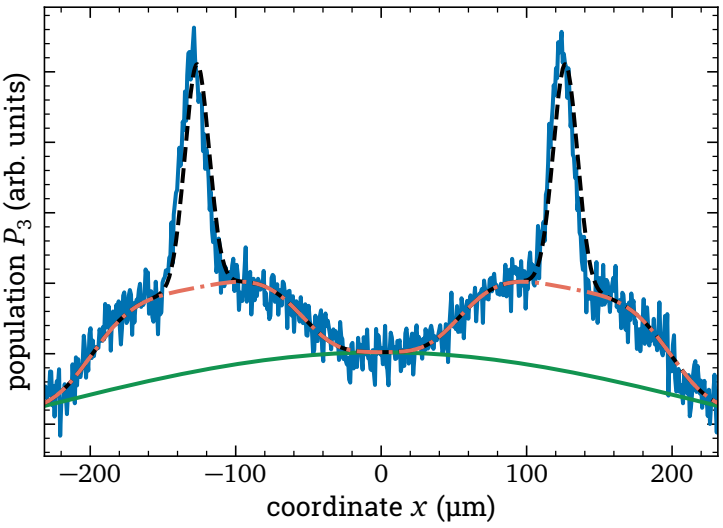

Figure B.1: NCP-driven ring localization using the optimized sequence with $N = 11$ pulses. Variation of the population $P_3(x)$ vs. coordinate x. The peak Rabi frequency is $\Omega_0 = 2\pi \times 2.5\,\text{MHz}$ and the total sequence duration is $t_C = 50\,\mu\text{s}$. Experimental data (blue line) and a fit to Equation (B.1) with the three features shown separately as black, dashed (localization), orange, dash-dotted (decay), and green (incoherent transfer) lines.

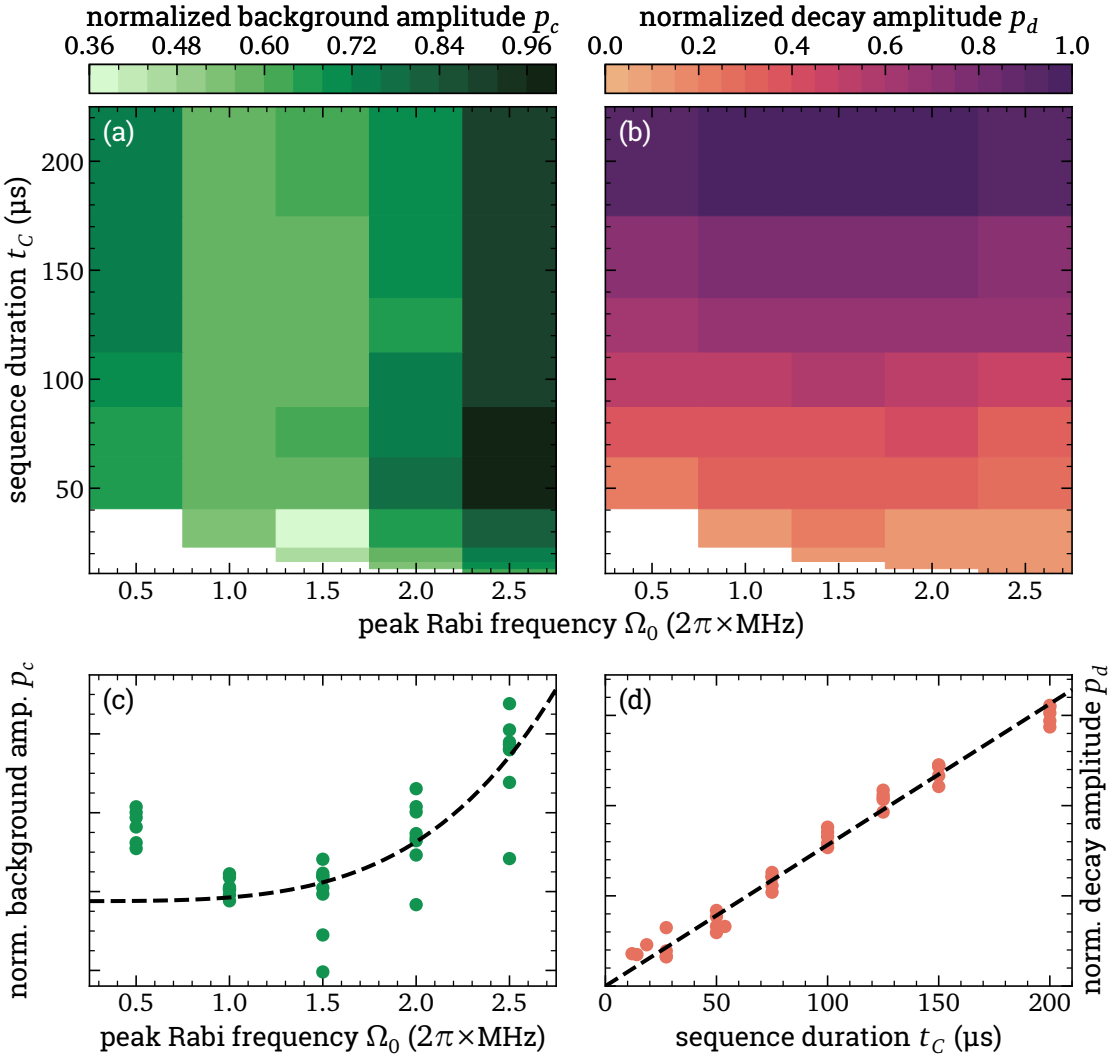

Figure B.2: Background analysis for NCP-driven ring localization using the optimized sequence with $N = 11$ pulses. Amplitude of the incoherent background peak (a) and broad ring (b) extracted with fits to Equation (B.1) vs. peak Rabi frequency Ω_0 and sequence duration t_C. (c) Data from (a) plotted only over the peak Rabi frequency (green circles) and a fit to a 4th order power law (black, dashed line). (d) Data from (b) plotted only over the sequence duration (orange circles) and a linear fit (black, dashed line).

We perform systematic measurements where we keep the pulse area fixed but vary the peak Rabi frequency Ω_0 and the total sequence duration t_C. We extract the amplitude of the broad, incoherent background p_c and the amplitude of the wide ring p_d from fits to Equation (B.1) and plot them in Figure B.2. As we can see, the background scales almost exclusively with the peak Rabi frequency Ω_0 but is independent of the total sequence duration t_C (see Figure B.2(a)), whereas the ring amplitude shows the opposite behavior (see Figure B.2(b)).

We attribute the broad background to the incoherent transfer of population from the initial state $|1\rangle$ directly to the final state $|3\rangle$, since it occurs in the pulse center where the pulse area $A(r = 0) = 2\pi$ and the NCP sequences suppress coherent excitation. We suspect that this population transfer is caused by Raman scattering. Alternatively, coupling to the excited state $|4\rangle$ could similarly lead

to such a transfer. However, state $|4\rangle$ is detuned from the NCP transition by 4.6 MHz, so this coupling should be negligible for our peak Rabi frequencies $\Omega_0 \leq 2\pi \times 2.5\,\mathrm{MHz}$. We plot the amplitude of this background over the peak Rabi frequency of the driving NCP pulses in Figure B.2(c) (green circles). Except for the data at $\Omega_0 = 2\pi \times 0.5\,\mathrm{MHz}$, we find that the background increases with the Rabi frequency, which supports our assumption. However, we find that the data scales with Ω_0^4 (see black, dashed line) and not Ω_0^2 as we would expect for both Raman scattering and off-resonant coupling. Hence, we require further investigations to fully understand the underlying process. Nevertheless, we see that a small peak Rabi frequency reduces the transfer and thus chose $\Omega_0 = 2\pi \times 1\,\mathrm{MHz}$ for most experiments in Chapter 2.

The broad ring, on the other hand, is caused by the decay of population during the NCP sequence. Since the pulse duration $\tau \approx 1\,\mu\mathrm{s}$ is much shorter than the excited state lifetime $T_1^e = 164\,\mu\mathrm{s}$, decay occurs only where a significant amount of population remains excited after each individual pulse, i.e., in the ring where $A(r) \approx \pi$. As expected, the ring amplitude is independent of the peak Rabi frequency but increases (linearly) with the sequence duration (see Figure B.2(d)). This background is almost negligible for the sequence durations $t_C \lesssim 30\,\mu\mathrm{s}$ we used in the main experiments.

Appendix C

Parameters of Robust CP Sequences for DD

In this appendix, we list the relevant parameters, i.e., the phases, of all robust DD sequences we investigated in Chapter 3.

We can calculate the phases ϕ_k of a universal robust sequence with an even number of pulses N from [83]

$$\phi_k = \frac{(k-1)(k-2)}{2}\Phi^{(N)} + (k-1)\phi_2 \tag{C.1}$$

with

$$\Phi^{(N)} = \begin{cases} \frac{\pi}{m} & N = 4m, \\ -\frac{2m\pi}{2m+1} & N = 4m+2. \end{cases} \tag{C.2}$$

ϕ_2 is a free parameter and we choose

$$\phi_2 = \frac{2-N}{2}\Phi^{(N)} \tag{C.3}$$

to create symmetric sequences.

We list the phases ϕ_k (in units of π) of all other sequences in the following table.

Table C.1: The phases (in units of π) of all DD sequences.

Sequence	Phases $(\phi_1, \phi_2, \ldots, \phi_N)$	source
CPMG	(0, 0)	[100, 101]
XY4	(0, 1, 0, 1)/2	[87]
XY8	(0, 1, 0, 1, 1, 0, 1, 0)/2	[88]
XY16	(0, 1, 0, 1, 1, 0, 1, 0, 2, 3, 2, 3, 3, 2, 3, 2)/2	[88]
KDD[1]	(1, 0, 3, 0, 1, 1, 0, 3, 0, 1)/6	[49]
KDD in XY4[1]	(1, 0, 3, 0, 1, 4, 3, 6, 3, 4, 1, 0, 3, 0, 1, 4, 3, 6, 3, 4)/6	[49]

[1] Note that we use a different nomenclature than the authors of [49]. In the latter work, the KDD sequence is called "CPMG (with robust pulses)" and the KDD in XY4 sequence is called "KDD sequence".

List of Abbreviations

AWG	Arbitrary waveform generator
BS	Beam splitter
CCD	Charge-coupled device
CP	Composite pulse
CPMG	"Carr, Purcell, Meiboom, Gill"
DD	Dynamical decoupling
EIT	Electromagnetically induced transparency
FWHM	Full width at half maximum
KDD	Knill dynamical decoupling
NCP	Narrowband composite pulse
NMR	Nuclear magnetic resonance
PD	Photodiode
PEEK	Polyether ether ketone
Pr:YSO	Praseodymium doped yttrium-orthosilicate (Pr^{3+}:Y_2SiO_5)
RF	Radio frequency
SPP	Spiral phase plate
STED	Stimulated emission depletion
STIRAP	Stimulated Raman adiabatic passage
UR	Universal robust (pulse sequence)

Bibliography

[1] C. Simon *et al. Quantum Memories - A Review Based on the European Integrated Project "Qubit Applications (QAP)".* European Physical Journal D **58,** 1 (2010).

[2] K. Heshami *et al. Quantum Memories: Emerging Applications and Recent Advances.* Journal of Modern Optics **63,** 2005 (2016).

[3] H. de Riedmatten and M. Afzelius. *Quantum Light Storage in Solid State Atomic Ensembles.* in *Engineering the Atom-Photon Interaction* (eds A. Predojević and M. W. Mitchell) (Springer International Publishing, Cham, 2015).

[4] D. Schraft, M. Hain, N. Lorenz, and T. Halfmann. *Stopped Light at High Storage Efficiency in a Pr^{3+}:Y_2SiO_5 Crystal.* Physical Review Letters **116,** 073602 (2016).

[5] Y. Ma *et al. One-Hour Coherent Optical Storage in an Atomic Frequency Comb Memory.* Nature Communications **12,** 2381 (2021).

[6] Z.-Q. Zhou *et al. Realization of Reliable Solid-State Quantum Memory for Photonic Polarization Qubit.* Physical Review Letters **108,** 190505 (2012).

[7] M. Afzelius, C. Simon, H. de Riedmatten, and N. Gisin. *Multimode Quantum Memory Based on Atomic Frequency Combs.* Physical Review A **79,** 052329 (2009).

[8] M. Bonarota, J.-L. Le Gouët, and T. Chanelière. *Highly Multimode Storage in a Crystal.* New Journal of Physics **13,** 013013 (2011).

[9] G. Heinze, N. Rentzsch, and T. Halfmann. *Multiplexed Image Storage by Electromagnetically Induced Transparency in a Solid.* Physical Review A **86,** 053837 (2012).

[10] S.-Y. Lan *et al. A Multiplexed Quantum Memory.* Optics Express **17,** 13639 (2009).

[11] T. Zhong and P. Goldner. *Emerging Rare-Earth Doped Material Platforms for Quantum Nanophotonics.* Nanophotonics **8,** 2003 (2019).

[12] J. G. Bartholomew and M. J. Sellars. *Technique for Frequency Selective, Sub-Diffraction Limited Imaging of Rare-Earth Ions in Bulk Crystals.* Journal of Luminescence **194,** 284 (2018).

[13] R. Kolesov *et al. Superresolution Microscopy of Single Rare-Earth Emitters in YAG and* H*3 Centers in Diamond.* Physical Review Letters **120,** 033903 (2018).

[14] G. Corrielli *et al. Integrated Optical Memory Based on Laser-Written Waveguides.* Physical Review Applied **5,** 054013 (2016).

[15] J. Mompart, V. Ahufinger, and G. Birkl. *Coherent Patterning of Matter Waves with Subwavelength Localization.* Physical Review A **79,** 053638 (2009).

[16] H. R. Hamedi *et al. Spatially Strongly Confined Atomic Excitation via a Two Dimensional Stimulated Raman Adiabatic Passage.* Optics Express **30,** 13915 (2022).

[17] A. V. Gorshkov *et al. Coherent Quantum Optical Control with Subwavelength Resolution.* Physical Review Letters **100,** 093005 (2008).

[18] C. Weitenberg *et al. Single-Spin Addressing in an Atomic Mott Insulator.* Nature **471,** 319 (2011).

[19] D. Viscor *et al. Single-Site Addressing of Ultracold Atoms beyond the Diffraction Limit via Position-Dependent Adiabatic Passage.* Physical Review A **86,** 063409 (2012).

[20] S. S. Ivanov and N. V. Vitanov. *High-Fidelity Local Addressing of Trapped Ions and Atoms by Composite Sequences of Laser Pulses.* Optics Letters **36,** 1275 (2011).

[21] N. V. Vitanov. *Arbitrarily Accurate Narrowband Composite Pulse Sequences.* Physical Review A **84,** 065404 (2011).

[22] J. T. Merrill *et al. Transformed Composite Sequences for Improved Qubit Addressing.* Physical Review A **90,** 040301 (2014).

[23] S. W. Hell and J. Wichmann. *Breaking the Diffraction Resolution Limit by Stimulated Emission: Stimulated-Emission-Depletion Fluorescence Microscopy.* Optics Letters **19,** 780 (1994).

[24] H. Blom and J. Widengren. *Stimulated Emission Depletion Microscopy.* Chemical Reviews **117,** 7377 (2017).

[25] K. D. Stokes *et al. Precision Position Measurement of Moving Atoms Using Optical Fields.* Physical Review Letters **67,** 1997 (1991).

[26] D. D. Yavuz and N. A. Proite. *Nanoscale Resolution Fluorescence Microscopy Using Electromagnetically Induced Transparency.* Physical Review A **76,** 041802 (2007).

[27] H. Li *et al. Optical Imaging beyond the Diffraction Limit via Dark States.* Physical Review A **78,** 013803 (2008).

[28] J. L. Rubio, D. Viscor, V. Ahufinger, and J. Mompart. *Nanoscale Resolution for Fluorescence Microscopy via Adiabatic Passage.* Optics Express **21,** 22139 (2013).

[29] A. P. Chu, K. K. Berggren, K. S. Johnson, and M. G. Prentiss. *A Virtual Slit for Atom Optics and Nanolithography.* Quantum and Semiclassical Optics **8,** 521 (1996).

[30] R. Abfalterer *et al. Nanometer Definition of Atomic Beams with Masks of Light.* Physical Review A **56,** R4365 (1997).

[31] K. S. Johnson *et al. Localization of Metastable Atom Beams with Optical Standing Waves: Nanolithography at the Heisenberg Limit.* Science **280,** 1583 (1998).

[32] J. H. Thywissen and M. Prentiss. *Demonstration of Frequency Encoding in Neutral Atom Lithography.* New Journal of Physics **7,** 47 (2005).

[33] J. Evers, S. Qamar, and M. S. Zubairy. *Atom Localization and Center-of-Mass Wave-Function Determination via Multiple Simultaneous Quadrature Measurements.* Physical Review A **75,** 053809 (2007).

[34] S. Subhankar *et al. Nanoscale Atomic Density Microscopy*. Physical Review X **9,** 021002 (2019).

[35] M. McDonald, J. Trisnadi, K.-X. Yao, and C. Chin. *Superresolution Microscopy of Cold Atoms in an Optical Lattice.* Physical Review X **9,** 021001 (2019).

[36] Z.-H. Qian *et al. Super-Resolved Imaging of a Single Cold Atom on a Nanosecond Timescale.* Physical Review Letters **127,** 263603 (2021).

[37] J. E. Thomas. *Uncertainty-Limited Position Measurement of Moving Atoms Using Optical Fields.* Optics Letters **14,** 1186 (1989).

[38] J. R. Gardner, M. L. Marable, G. R. Welch, and J. E. Thomas. *Suboptical Wavelength Position Measurement of Moving Atoms Using Optical Fields.* Physical Review Letters **70,** 3404 (1993).

[39] K. T. Kapale. *Subwavelength Atom Localization.* in *Progress in Optics 58* (ed E. Wolf) 1st edition (Elsevier, Oxford, Amsterdam, 2013).

[40] K. Bergmann, H. Theuer, and B. W. Shore. *Coherent Population Transfer among Quantum States of Atoms and Molecules.* Reviews of Modern Physics **70,** 1003 (1998).

[41] N. V. Vitanov, T. Halfmann, B. W. Shore, and K. Bergmann. *Laser-Induced Population Transfer by Adiabatic Passage Techniques.* Annual Review of Physical Chemistry **52,** 763 (2001).

[42] M. H. Levitt. *Composite Pulses.* Progress in Nuclear Magnetic Resonance Spectroscopy **18,** 61 (1986).

[43] M. H. Levitt. *Composite Pulses.* in *eMagRes* (eds R. K. Harris and R. L. Wasylishen) (John Wiley & Sons, Ltd, 2007).

[44] J. T. Merrill and K. R. Brown. *Progress in Compensating Pulse Sequences for Quantum Computation.* in *Quantum Information and Computation for Chemistry* (eds S. A. Rice, A. R. Dinner, and S. Kais) (John Wiley & Sons, Ltd, Hoboken, New Jersey, 2014).

[45] G. S. Agarwal and K. T. Kapale. *Subwavelength Atom Localization via Coherent Population Trapping.* Journal of Physics B: Atomic, Molecular and Optical Physics **39,** 3437 (2006).

[46] L. Viola, E. Knill, and S. Lloyd. *Dynamical Decoupling of Open Quantum Systems.* Physical Review Letters **82,** 2417 (1999).

[47] D. Suter and G. A. Álvarez. *Colloquium: Protecting Quantum Information against Environmental Noise.* Reviews of Modern Physics **88,** 041001 (2016).

[48] A. M. Souza, G. A. Álvarez, and D. Suter. *Robust Dynamical Decoupling.* Philosophical Transactions of the Royal Society A: Mathematical, Physical and Engineering Sciences **370,** 4748 (2012).

[49] A. M. Souza, G. A. Álvarez, and D. Suter. *Robust Dynamical Decoupling for Quantum Computing and Quantum Memory.* Physical Review Letters **106,** 240501 (2011).

[50] M. H. Levitt and R. Freeman. *NMR Population Inversion Using a Composite Pulse.* Journal of Magnetic Resonance (1969) **33,** 473 (1979).

[51] M. Stabel, L. D. Feldmann, and T. Halfmann. *Confining Atomic Populations in Space via Stimulated Raman Adiabatic Passage in a Doped Solid.* Journal of Physics B: Atomic, Molecular and Optical Physics **55,** 154003 (2022).

[52] M. Fleischhauer, A. Imamoglu, and J. P. Marangos. *Electromagnetically Induced Transparency: Optics in Coherent Media.* Reviews of Modern Physics **77,** 633 (2005).

[53] J. A. Miles, Z. J. Simmons, and D. D. Yavuz. *Subwavelength Localization of Atomic Excitation Using Electromagnetically Induced Transparency.* Physical Review X **3,** 031014 (2013).

[54] J. A. Miles, D. Das, Z. J. Simmons, and D. D. Yavuz. *Localization of Atomic Excitation beyond the Diffraction Limit Using Electromagnetically Induced Transparency.* Physical Review A **92,** 033838 (2015).

[55] N. V. Vitanov, A. A. Rangelov, B. W. Shore, and K. Bergmann. *Stimulated Raman Adiabatic Passage in Physics, Chemistry, and Beyond.* Reviews of Modern Physics **89,** 015006 (2017).

[56] J. Choi and D. S. Elliott. *Influence of Interaction Time and Population Redistribution on the Localization of Atomic Excitation through Electromagnetically Induced Transparency.* Physical Review A **89,** 013414 (2014).

[57] S. Pachava *et al. Generation and Decomposition of Scalar and Vector Modes Carrying Orbital Angular Momentum: A Review.* Optical Engineering **59,** 041205 (2019).

[58] L. Allen and M. Padgett. *Introduction to Phase-Structured Electromagnetic Waves.* in *Structured Light and Its Applications* (ed D. L. Andrews) (Elsevier, Burlington, 2008).

[59] P. Senthilkumaran. *Singularities in Physics and Engineering: Properties, Methods, and Applications* (IOP Publishing, 2018).

[60] E. J. Galvez. *Singular Optics and Phase Properties.* in *Structured Light and Its Applications* (ed D. L. Andrews) (Elsevier, Burlington, 2008).

[61] Y. C. Sun. *Rare Earth Materials in Optical Storage and Data Processing Applications.* in *Spectroscopic Properties of Rare Earths in Optical Materials* (eds L. Guokui and B. Jacquier) 1st edition (Springer, Berlin, 2006).

[62] A. Vijayakumar *et al. Generation of Structured Light by Multilevel Orbital Angular Momentum Holograms.* Optics Express **27,** 6459 (2019).

[63] G. Heinze. *Kohärente optische Datenspeicherung mittels EIT in einem Pr^{3+}:Y_2SiO_5-Kristall.* PhD thesis (TU Darmstadt, 2013).

[64] M. Nilsson *et al. Hole-Burning Techniques for Isolation and Study of Individual Hyperfine Transitions in Inhomogeneously Broadened Solids Demonstrated in Pr^{3+}:Y_2SiO_5.* Physical Review B **70,** 214116 (2004).

[65] F. Beil, J. Klein, G. Nikoghosyan, and T. Halfmann. *Electromagnetically Induced Transparency and Retrieval of Light Pulses in a Λ-type and a V-type Level Scheme in Pr^{3+}:Y_2SiO_5.* Journal of Physics B: Atomic, Molecular and Optical Physics **41,** 074001 (2008).

[66] S. Mieth, A. Henderson, and T. Halfmann. *Tunable, Continuous-Wave Optical Parametric Oscillator with More than 1W Output Power in the Orange Visible Spectrum.* Optics Express **22,** 11182 (2014).

[67] S. Mieth. *Preserving Atomic Coherences for Light Storage in Pr^{3+}:Y_2SiO_5 Driven by an OPO Laser System.* PhD thesis (TU Darmstadt, 2015).

[68] G. H. Zhang, B. Braverman, A. Kawasaki, and V. Vuletić. *Note: Fast Compact Laser Shutter Using a Direct Current Motor and Three-Dimensional Printing.* Review of Scientific Instruments **86,** 126105 (2015).

[69] A. Bruns. *Population Transfer by Composite Stimulated Raman Adiabatic Passage.* Master's thesis (TU Darmstadt, 2017).

[70] G. Wolfowicz and J. J. Morton. *Pulse Techniques for Quantum Information Processing.* in *eMagRes* (eds R. K. Harris and R. L. Wasylishen) (John Wiley & Sons, Ltd, Chichester, 2016).

[71] R. Tycko and A. Pines. *Iterative Schemes for Broad-Band and Narrow-Band Population Inversion in NMR.* Chemical Physics Letters **111,** 462 (1984).

[72] A. Shaka and R. Freeman. *Spatially Selective Radiofrequency Pulses.* Journal of Magnetic Resonance (1969) **59,** 169 (1984).

[73] A. Shaka, J. Keeler, M. Smith, and R. Freeman. *Spatial Localization of NMR Signals in an Inhomogeneous Radiofrequency Field.* Journal of Magnetic Resonance (1969) **61,** 175 (1985).

[74] B. T. Torosov, E. S. Kyoseva, and N. V. Vitanov. *Composite Pulses for Ultrabroad-Band and Ultranarrow-Band Excitation.* Physical Review A **92,** 033406 (2015).

[75] K. R. Brown, A. W. Harrow, and I. L. Chuang. *Arbitrarily Accurate Composite Pulse Sequences.* Physical Review A **70,** 052318 (2004).

[76] S. Wimperis. *Broadband, Narrowband, and Passband Composite Pulses for Use in Advanced NMR Experiments.* Journal of Magnetic Resonance, Series A **109,** 221 (1994).

[77] G. T. Genov, B. T. Torosov, and N. V. Vitanov. *Optimized Control of Multistate Quantum Systems by Composite Pulse Sequences.* Physical Review A **84,** 063413 (2011).

[78] B. T. Torosov and N. V. Vitanov. *High-Fidelity Composite Quantum Gates for Raman Qubits.* Physical Review Research **2,** 043194 (2020).

[79] C. Zhang *et al. Narrowband and Passband Composite Pulses in the Three-Level System.* http://arxiv.org/abs/2205.14432. preprint (2022).

[80] B. T. Torosov, S. S. Ivanov, and N. V. Vitanov. *Narrowband and Passband Composite Pulses for Variable Rotations.* Physical Review A **102,** 013105 (2020).

[81] B. T. Torosov and N. V. Vitanov. *Narrowband Composite Two-Qubit Gates for Crosstalk Suppression.* Physical Review A **107,** 032618 (2023).

[82] M. Hain, M. Stabel, and T. Halfmann. *Few-Photon Storage on a Second Timescale by Electromagnetically Induced Transparency in a Doped Solid.* New Journal of Physics **24,** 023012 (2022).

[83] G. T. Genov, D. Schraft, N. V. Vitanov, and T. Halfmann. *Arbitrarily Accurate Pulse Sequences for Robust Dynamical Decoupling.* Physical Review Letters **118,** 133202 (2017).

[84] P. Jobez *et al. Coherent Spin Control at the Quantum Level in an Ensemble-Based Optical Memory.* Physical Review Letters **114,** 230502 (2015).

[85] A. Holzäpfel *et al. Optical Storage for 0.53 s in a Solid-State Atomic Frequency Comb Memory Using Dynamical Decoupling.* New Journal of Physics **22,** 063009 (2020).

[86] Y. Wang *et al. Single-Qubit Quantum Memory Exceeding Ten-Minute Coherence Time.* Nature Photonics **11,** 646 (2017).

[87] A. A. Maudsley. *Modified Carr-Purcell-Meiboom-Gill Sequence for NMR Fourier Imaging Applications.* Journal of Magnetic Resonance (1969) **69,** 488 (1986).

[88] T. Gullion, D. B. Baker, and M. S. Conradi. *New, Compensated Carr-Purcell Sequences.* Journal of Magnetic Resonance (1969) **89,** 479 (1990).

[89] C. A. Ryan, J. S. Hodges, and D. G. Cory. *Robust Decoupling Techniques to Extend Quantum Coherence in Diamond.* Physical Review Letters **105,** 200402 (2010).

[90] G. A. Álvarez, A. Ajoy, X. Peng, and D. Suter. *Performance Comparison of Dynamical Decoupling Sequences for a Qubit in a Rapidly Fluctuating Spin Bath.* Physical Review A **82,** 042306 (2010).

[91] M. A. A. Ahmed, G. A. Álvarez, and D. Suter. *Robustness of Dynamical Decoupling Sequences.* Physical Review A **87,** 042309 (2013).

[92] N. Ezzell *et al. Dynamical Decoupling for Superconducting Qubits: A Performance Survey.* http://arxiv.org/abs/2207.03670. preprint (2023).

[93] M. Hain. *EIT Light Storage of Weak Coherent Pulses in a Doped Solid.* PhD thesis (TU Darmstadt, 2021).

[94] N. Stewen. *Robust Dynamical Decoupling Driven by Pulses with Field Inhomogeneities in Pr^{3+}:Y_2SiO_5.* Master's thesis (TU Darmstadt, 2023).

[95] N. Lorenz. *Optimising EIT Light Storage Efficiency in Pr^{3+}:Y_2SiO_5.* Master's thesis (TU Darmstadt, 2014).

[96] J. Mispelter, M. Lupu, and A. Briguet. *NMR Probeheads for Biophysical and Biomedical Experiments: Theoretical Principles & Practical Guidelines* 2nd edition (Imperial College Press, London, 2005).

[97] E. L. Hahn. *Spin Echoes.* Physical Review **80,** 580 (1950).

[98] G. T. Genov, D. Schraft, and T. Halfmann. *Rephasing Efficiency of Sequences of Phased Pulses in Spin-Echo and Light-Storage Experiments.* Physical Review A **98,** 063836 (2018).

[99] E. Fraval, M. Sellars, A. Morrison, and A. Ferris. *Pr–Y Interaction in Pr^{3+}:Y_2SiO_5.* Journal of Luminescence **107,** 347 (2004).

[100] H. Y. Carr and E. M. Purcell. *Effects of Diffusion on Free Precession in Nuclear Magnetic Resonance Experiments.* Physical Review **94,** 630 (1954).

[101] S. Meiboom and D. Gill. *Modified Spin-Echo Method for Measuring Nuclear Relaxation Times.* Review of Scientific Instruments **29,** 688 (1958).

[102] B. Herzog and E. L. Hahn. *Transient Nuclear Induction and Double Nuclear Resonance in Solids.* Physical Review **103,** 148 (1956).

[103] J. R. Klauder and P. W. Anderson. *Spectral Diffusion Decay in Spin Resonance Experiments.* Physical Review **125,** 912 (1962).

[104] W. B. Mims. *Phase Memory in Electron Spin Echoes, Lattice Relaxation Effects in $CaWO_4$:Er, Ce, Mn.* Physical Review **168,** 370 (1968).

[105] M. F. Pascual-Winter, R.-C. Tongning, T. Chanelière, and J.-L. Le Gouët. *Spin Coherence Lifetime Extension in Tm^{3+}:YAG through Dynamical Decoupling.* Physical Review B **86,** 184301 (2012).

[106] G. de Lange *et al. Universal Dynamical Decoupling of a Single Solid-State Spin from a Spin Bath.* Science **330,** 60 (2010).

[107] A. Arcangeli *et al. Spectroscopy and Coherence Lifetime Extension of Hyperfine Transitions in $^{151}Eu^{3+}$:Y_2SiO_5.* Physical Review B **89,** 184305 (2014).

[108] D. N. Matsukevich *et al. Observation of Dark State Polariton Collapses and Revivals.* Physical Review Letters **96,** 033601 (2006).

[109] T. Peters *et al. Optimizing the Retrieval Efficiency of Stored Light Pulses.* Optics Express **17,** 6665 (2009).

[110] G. Heinze, S. Mieth, and T. Halfmann. *Control of Dark-State Polariton Collapses in a Doped Crystal.* Physical Review A **84,** 013827 (2011).

[111] E. Fraval, M. J. Sellars, and J. J. Longdell. *Dynamic Decoherence Control of a Solid-State Nuclear-Quadrupole Qubit.* Physical Review Letters **95,** 030506 (2005).

[112] M. J. Biercuk *et al. Optimized Dynamical Decoupling in a Model Quantum Memory*. Nature **458,** 996 (2009).

[113] J. Du *et al. Preserving Electron Spin Coherence in Solids by Optimal Dynamical Decoupling.* Nature **461,** 1265 (2009).

[114] A. Beckert *et al. Emergence of Highly Coherent Quantum Subsystems of a Noisy and Dense Spin System.* http://arxiv.org/abs/2210.01024. preprint (2022).

[115] J. J. Longdell, M. J. Sellars, and N. B. Manson. *Hyperfine Interaction in Ground and Excited States of Praseodymium-Doped Yttrium Orthosilicate.* Physical Review B **66,** 035101 (2002).

[116] E. Fraval, M. J. Sellars, and J. J. Longdell. *Method of Extending Hyperfine Coherence Times in Pr^{3+}:Y_2SiO_5.* Physical Review Letters **92,** 077601 (2004).

[117] M. Zhong *et al. Optically Addressable Nuclear Spins in a Solid with a Six-Hour Coherence Time.* Nature **517,** 177 (2015).

Publications and Contributions to Conferences

Work Directly Related to this Dissertation

Publications in Peer-Reviewed Journals

- M. Stabel, L. Feldmann, and T. Halfmann.
  Confining Atomic Populations in Space via Stimulated Raman Adiabatic Passage in a Doped Solid.
  Journal of Physics B: Atomic, Molecular and Optical Physics **55**, 154003 (2022)
  Published as part of the special issue "Coherent Control: Photons, Atoms and Molecules"

Manuscripts in Preparation

- M. Stabel, N. Joseph, N. V. Vitanov, and T. Halfmann.
  Spatial Confinement of Atomic Excitation by Composite Pulses in a Doped Solid.

Contributions to National and International Conferences

- M. Stabel, L. Feldmann, and T. Halfmann.
  Confining Atomic Populations in Space via Stimulated Raman Adiabatic Passage in a Doped Solid.
  Talk at Rare Earth Ion Workshop (Edinburgh, UK, June 2022)

- M. Stabel, L. Feldmann, and T. Halfmann.
  Confining Atomic Populations in Space via Stimulated Raman Adiabatic Passage in a Doped Solid.
  Talk at CAMEL (Nessebar, Bulgaria, August 2022)

- M. Stabel, N. Stewen, and T. Halfmann.
  Robust Dynamical Decoupling Driven by Pulses with Field Inhomogeneities in Pr:YSO.
  Talk at CAMEL (Nessebar, Bulgaria, June 2023)

- N. Joseph, M. Stabel, N. V. Vitanov, and T. Halfmann.
  Spatial Confinement of Atomic Excitation by Composite Pulses in Pr:YSO.
  Poster at Rare Earth Ion Workshop (Lund, Sweden, September 2023)

- N. Stewen, M. Stabel, and T. Halfmann.
  Robust Dynamical Decoupling Driven by Pulses with Field Inhomogeneities in Pr:YSO.
  Poster at Rare Earth Ion Workshop (Lund, Sweden, September 2023)

Further Work not Directly Related to this Dissertation

Publications in Peer-Reviewed Journals

- M. Hain, M. Stabel, and T. Halfmann.
  Few-Photon Storage on a Second Timescale by Electromagnetically Induced Transparency in a Doped Solid.
  New Journal of Physics **24**, 023012 (2022)

Contributions to National and International Conferences

- M. Stabel, M. Hain, and T. Halfmann.
  EIT Light Storage of Weak Coherent Pulses in Pr:YSO.
  Talk at Rare Earth Ion Workshop (Grenoble, France, October 2019)

- M. Stabel, M. Hain, and T. Halfmann.
  Solid-State Few-Photon Storage on a Second Timescale Using Electromagnetically Induced Transparency.
  Poster at Rare Earth Ion Workshop (Bad Honnef, Germany, August 2021)
  Winner of the Best Poster Prize

Supervisions and Contributions to Teaching

Master's Projects

- Benedikt Moneke. *Setup of a Tunable, Narrowband, Continuous Wave Optical Parametric Oscillator at 606 nm*. (2020)
- Leo Feldmann. *Precise Localization by Adiabatic Population Transfer in* $Pr^{3+}:Y_2SiO_5$. (2022)
- Niels Joseph. *Spatial Confinement of Atomic Excitation by Composite Pulses in* $Pr^{3+}:Y_2SiO_5$. (2022)
- Niklas Stewen. *Robust Dynamical Decoupling Driven by Pulses With Field Inhomogeneities in* $Pr^{3+}:Y_2SiO_5$. (2023)

Bachelor's Projects

- Viktor Mitura. *Optimierung von atomaren Frequenzkämmen zur Steigerung der Lichtspeichereffizienz in* $Pr^{3+}:Y_2SiO_5$. (2020)
- Niels Joseph. *Preliminary Studies towards Spatial Modulation of Adiabatic Population Transfer in* $Pr^{3+}:Y_2SiO_5$. (2021)
- Thomas Riederer. *STIRAP Autokorrelation lokalisierter Anregung in* $Pr^{3+}:Y_2SiO_5$. (2022)

Contributions to Teaching

- Supervision of Advanced Laboratory Courses
  - *Acousto-Optic Modulator* (06/2020–02/2023)
- Lab tours (2019–2023)

Erklärungen laut Promotionsordnung

§8 Abs. 1 lit. c PromO
Ich versichere hiermit, dass die elektronische Version meiner Dissertation mit der schriftlichen Version übereinstimmt.

§8 Abs. 1 lit. d PromO
Ich versichere hiermit, dass zu einem vorherigen Zeitpunkt noch keine Promotion versucht wurde. In diesem Fall sind nähere Angaben über Zeitpunkt, Hochschule, Dissertationsthema und Ergebnis dieses Versuchs mitzuteilen.

§9 Abs. 1 PromO
Ich versichere hiermit, dass die vorliegende Dissertation selbstständig und nur unter Verwendung der angegebenen Quellen verfasst wurde.

§9 Abs. 2 PromO
Die Arbeit hat bisher noch nicht zu Prüfungszwecken gedient.

Darmstadt, 10. Januar 2024

_____
(Markus Stabel)